UNIVERSITY OF CALIFORNIA

SANTA CRUZ

OBSERVATIONAL STUDIES OF DRIZZLE IN MARINE STRATOCUMULUS

A dissertation submitted in partial satisfaction
of the requirements for the degree of

DOCTOR OF PHILOSOPHY

in

EARTH SCIENCE

by

Dione Lee Rossiter

June 2012

The Dissertation of Dione Lee Rossiter
is approved:

Professor Patrick Y. Chuang, Chair

Professor Andrew M. Moore

Professor Qing Wang

Tyrus Miller
Vice Provost and Dean of Graduate Studies

Contents

List of Figures

List of Tables

ABSTRACT

OBSERVATIONAL STUDIES OF DRIZZLE IN MARINE STRATOCUMULUS

by

DIONE LEE ROSSITER

The most expansive and persistent clouds, reducing the net radiation balance on a annually averaged global basis by ∼15 W/m^2, are the low-lying marine stratocumulus (MSc) which hover over the eastern subtropical oceans. Despite their climatic importance, key processes and feedbacks within the MSc regime have yet to be fully quantified or understood. The goal of this research is to improve our understanding of MSc processes and their impact on the marine boundary layer (MBL). Specifically, using *in situ* aircraft cloud microphysical measurements, this research pays particular attention to the process of drizzle, the sedimentation of liquid water. Data utilized in this study primarily come from the Artium Flight Phase Doppler Interferometer (F/PDI) and the Cloud Imaging Probe (CIP) during four days of the Marine Stratus Experiment (MASE) in July 2005 in the northeastern Pacific near Monterey, California. Results presented in this dissertation are especially unique because of the broad and continuous range in which the F/PDI samples (2-100 µm diameter), a size range measured by no other instrument alone with the same resolution and accuracy. The upper portion of this size range, ∼30 to 100 µm, is of particular importance to the initiation and evolution of drizzle but traditionally, has been difficult to measure well.

The first goal of this research was to characterize in-cloud drizzle during the four MASE days by exploring the horizontal and vertical structure of drizzle. Drizzle statistics indicate two microphysical regimes exist, a high drizzle regime, associated with patches of heavy drizzle occurring in clusters, and a low drizzle regime, associated with more uniform, light-to-no drizzle. Heavy drizzle regimes exhibit significant drop growth

by collision-coalescence while low drizzle regimes exhibit drop growth primarily from condensation. The second goal of this research is to quantify the effects of drizzle on the MBL via the process of evaporation. The observations indicate a large range of BL cooling exists among the four study days. Sub-cloud profiles of evaporative cooling show variability in the location of peak and total depth of cooling. Variability is also found to exist in the horizontal. Lastly, cloud top (CT) processes which may be responsible for the initiation of drizzle during the heavy drizzle days are investigated. We utilize drop size distribution (DSD) measured from CIP/PDI and derived from box model simulations to calculate CT collision rates. We found the observational collision rates follow a power law with the observed slope, m, varying at CT between well-developed and less-developed drizzling MSc. No correlations between m and other observed cloud properties were found. Drop size distributions simulated from a box model of collision-coalescence suggest that while collision rates can be impacted by properties such as turbulence and cloud drop residence time, realistic values were insufficient to reproduce observed CT collision rates.

For my teachers (K-22).

Acknowledgments

I would like to begin by thanking my advisor, Professor Patrick Y. Chuang, for allowing me to be a member of his lab, for inviting me to attend five field projects and ten conferences, for the hundreds of hours he spent supporting this dissertation, for not letting me quit, and for supplying me with all the tools for my science toolbox. I would also like to thank the rest of my reading committee members, Prof.s Qing Wang and Andrew Moore for their continued support, insight, and generous guidance during the past four years, especially with regards to this dissertation.

I would next like to thank my colleagues, the most amazing labmates on Earth: Dr. Chris Ruehl, Dr. Jennifer Small, and Mikael Witte. I cannot imagine the last six years of my life without the support of each one of these individuals. A special thanks goes out to Chris, who welcomed me into the lab with open arms from day one. I miss our daily chats in lab, having a great friend off campus as well as on, and his wife, Dr. Jean Ruehl. I would also like to highlight and thank my science sister, Jen, for her immense support: emotional, academic, administrative- you name it. I have never met such a loving, helpful, and sincere individual. She always had a shoulder for me to cry on, a warm embrace, and an open ear available at all times. Jen continued to offer her guidance long after she left UCSC, never hesitating to help me in any way she could. Patrick, Jen, Chris, and Mikael: I am so lucky to have such and awesome science family... thank you from the bottom of my heart!

I would next like to thank the two individuals who made all of this possible; without their support and encouragement, I would have never applied to graduate school in the

first place. First, Dr. Tanya Faltens taught me how to "embrace my fear" of failing and looking stupid. She was there for me during each step of the application process: guiding me, offering advice, and editing my written work. Second, Dr. Rajul Pandya convinced me I would have a better life with a PhD. He absolutely insisted I go to graduate school, never once wavering, and refused to take "no" for an answer. Both of these individuals showed consistent personal support throughout graduate school as well, writing letters of recommendations, responding to phone calls and emails of distress. Raj even once conducted a mock-interview with me, and somehow (I am not sure how) he always made time during his crazy-hectic schedule at AGU to sit down with me, take a breath, and discuss my life, my experiences, and my struggles. On a similar note, I would like to thank the UCAR-NCAR SOARS Program. I am not sure what my life would be like without SOARS. Every open door I have encountered since 2003 has been a result of the SOARS Program.

I would like to continue by thanking the Earth and Planetary Science (EPS) Department office staff, the EPS technical staff, the CIRPAS crew, and the scientists at Artium Technologies. I would like to thank everyone at AGU, AAAS, and VOA for allowing me to follow my dreams, while at the same time enjoy the most amazing summer of my life. I would like to thank my taekwondo family, my running girls, plus all of my "grad bests" for helping me through all of the *interesting* moments of graduate school. Specifically, I would like to thank Dr. Nicole Kinsman, Dr. Travis O'Brien, and soon-to-be-mom-and-Dr. Kathleen Uzilov.

Finally, I would like to thank my parents, Norma and Bermil Rossiter, for putting up with me for 30+ years. Thank you for always supporting my education, for teaching me how to be a confident woman, and for holding my hand through thick and thin. Words cannot express my heartfelt appreciation... of course, I am indebted to you for life. I love you.

Chapter 1

Introduction

On any given day, clouds hover over 67% of the Earth's surface, as measured by satellites capturing hundreds of images of the Earth a day. [1] From space clouds appear homogeneous and two-dimensional (Fig. 1.1), but clouds are not only abundant, they are also diverse, ranging is size, height and location. It is no surprise, then, that long before advanced meteorological technology existed (ie. satellites, radiosondes, models, radar, etc.), measuring and understanding the diversities of clouds has been a goal of scientists for millennia. Ancient Indian texts written as far back as 505-587 AD discuss the process of cloud formation and rainfall prediction [*Sivaprakasam and Kanakasabai*, 2009].

While it may seem counter-intuitive that something as commonplace as clouds would cause such consternation with scientists, in fact, it is the implications of cloud ubiquity and variety that are truly challenging. Clouds are one of the principal players involved in regulating the Earth's temperature and serve a large and complex role in many of the Earth's climate processes. Although, in the current climate, clouds on average cool the Earth, reflecting 20% of the Earth's incoming solar radiation, depending on their specifics - their height, size, and location - clouds have varying effects on different regions.

[1] Derived from 2009 MODIS mean global cloud fraction data

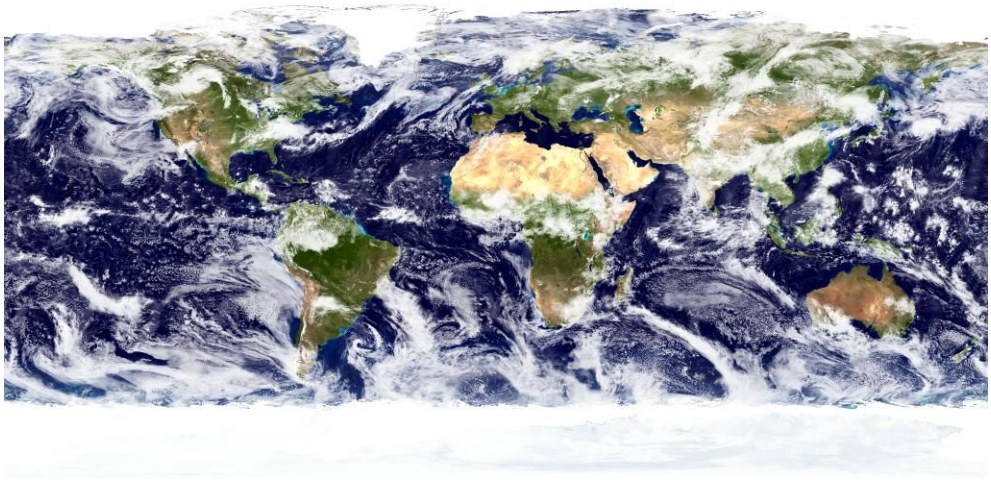

Figure 1.1: Earth from space
The "blue marble" is a composite of images taken using NASA's MODIS, a remote-sensing devise onboard the Terra satellite. The image highlights the abundance of clouds which hug the Earth's surface. Photo credit: NASA Goddard Space Flight Center Image by Reto Stöckli (land surface, shallow water, clouds). Enhancements by Robert Simmon (ocean color, compositing, 3D globes, animation). Data and technical support: MODIS Land Group; MODIS Science Data Support Team; MODIS Atmosphere Group; MODIS Ocean Group Additional data: USGS EROS Data Center (topography); USGS Terrestrial Remote Sensing Flagstaff Field Center (Antarctica); Defense Meteorological Satellite Program (city lights).

Clouds are just as important to regional climates, ecosystems, and societies because they carry with them rain, snow, and fog. Clouds determine where and how fresh water is distributed around the globe. In order to understand, and hopefully predict, patterns of rainfall, we must first understand the processes that determine how moisture is transported through the atmosphere.

Scientists have also discovered that human-induced changes affect the way clouds form, produce rain, dissipate, and even interfere with shortwave (SW) and longwave (LW) radiation. An increase in atmospheric greenhouse gases, an increase in atmospheric particles, and the destruction of native ecosystems are all examples of unnatural trends that will directly change the evolution of clouds and their properties. Also, because clouds are so complex and diverse, they are the largest source of uncertainty when

calculating the global anthropogenic radiative forcing [*IPCC,* 2007;*Bony et al.*, 2006; *Cronin et al.*, 2006; *Wyant et al.*, 2006; *Bony and Dufresne*, 2005]. Before scientists can understand the behavior of the global climate, they must first better understand the behavior of clouds.

But researchers are gaining a stronger grasp of the nuances associated with cloud properties. Armed with at least a dozen cloud observing satellites, countless cloud probing instruments scattered across every continent, and models that simulate clouds from meter to global scales, scientists are determined to better understand all properties of clouds. The broadest goal of this research is to contribute to this cause: to increase the understanding one type of cloud, the marine stratocumulus cloud.

1.1 Motivation and background

Despite decades of research (starting with *Lilly*, 1968), key processes and feedbacks within the marine stratocumulus (MSc) regime have yet to be fully understood. These vast and frequent low lying cloud decks are one of the main features of the Earth's atmosphere and significantly impact climate. MSc clouds on average cover 34% of the oceans [*Klein and Hartmann*, 1993], can locally reflect up to 20% of the earth's incoming solar radiation (70 W/m^2, *Stephens and Greenwald*, 1991), and reduce the net radiation balance on a annually averaged global basis by $\sim$15 W/m^2 [*Hartmann et al.*, 1992]. A small change of MSc cloud cover over time can lead to substantial radiative impacts on the climate system and furthermore may lead to unforeseen feedbacks.

While MSc are important to the radiative balance on a regional scale with global consequences, their properties are dependent on processes from the synoptic scale (e.g. subsidence) to the micro-scale (e.g. collision-coalescence) that control their formation, evolution, and dissipation. Therefore, in order to understand how MSc clouds impact

the atmosphere, one must focus particular attention on the microphysical processes that control their evolution. The aim of this research is to use *in situ* microphysical measurements to explore and better understand the primary physical processes of MSc clouds. The long-term goal is to better understand their influence on climate and their response to climate change.

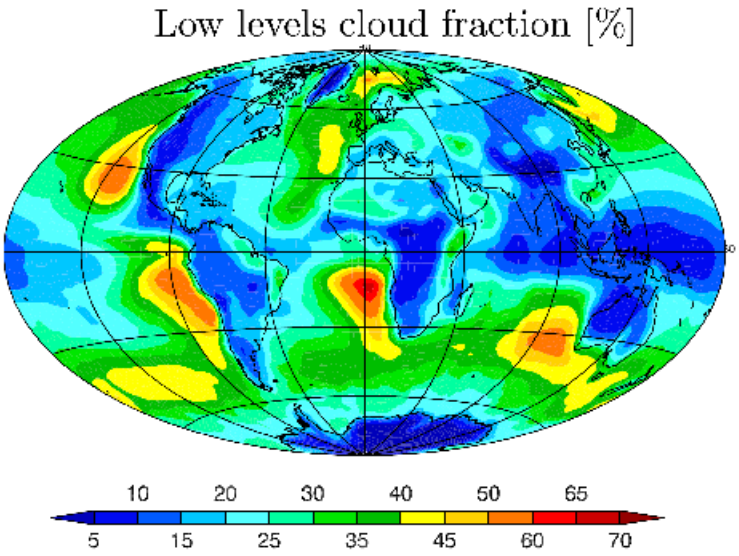

Figure 1.2: Average low-level cloud fraction (1983-2005)
This International Satellite Cloud Climatology Project (ISCCP, *Rossow and Schiffer*, 1999) map of low-level clouds shows strongest low-cloud occurrence over the eastern sub-tropical oceans.

1.1.1 Marine stratocumulus clouds

The most widespread and ubiquitous clouds, having a strong negative effect on the Earth's radiation budget, are the low lying MSc which blanket the world's eastern sub-tropical oceans [*Eastman et al.*, 2011]. Figure 1.2 shows the low-level cloud fraction, the fraction of sky covered by clouds, averaged over the period 1983 through 2005. As this figure highlights, low-level clouds are most common off of the west coast of the

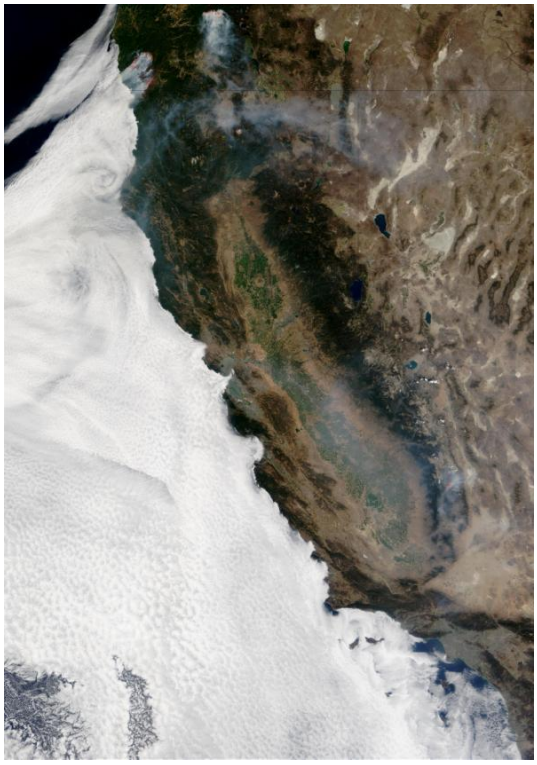

Figure 1.3: MSc off of the West Coast of the US
This image captures the prominence of the MSc over the eastern Pacific. Also visible in this August, 14, 2012 MODIS Satellite image is the Biscuit and Tiller Complex Fire in the southwest corner of Oregon (upper left hand corner of the photo). Both fires were caused by a single lightening storm. MSc, like this one, are sensitive to aerosol concentrations derived from a combination of natural and anthropogenic sources (fires, volcanic emissions, desert dust, the products of fossil fuel combustion, etc). Photo credit: Jacques Descloitres, MODIS Land Rapid Response Team, NASA/GSFC

US, Chile, Africa, Europe and Australia (areas of warmer colors) and are least common over continents. *Klein and Hartmann* [1993] found that in the summer months, when conditions in these regions are most ideal, cloud cover can exceed 80%.

The images in Fig. 1.3 and 1.4 depict the strength of the MSc in size, reflectivity, and its striking ability to hug the western coastline of the US. Figure 1.3 is a Moderate Resolution Imaging Spectroradiometer (MODIS) image of a typical summertime MSc cloud. The marine layer, as it is known to most West Coast natives, is a classic feature of the coast, often interrupting a warm day at the beach (Fig. 1.4).

Stratocumulous clouds result in strong radiative cooling because of the combination of two main features: their high albedo, α, (0.4-0.8) reflects more solar radiation compared to the low α of the ocean's surface (0.05-0.1), while their low altitude causes their emitted LW radiation to be similar to that of the Earth's surface. MSc are such a significant climate forcing that *Slingo* [1990] found a 20% increase in the relative amount of low clouds could balance the greenhouse warming expected from a doubling of CO_2. While the sensitivity of the Earth's energy budget to MSc is large, their quantitative impact on the stratocumulus-topped boundary layer (STBL) remain unknown – for such an expansive and stable cloud, MSc have been historically hard to model [*Bretherton et al.*, 2004]. Even at the surface, quantifying the effects that MSc have on the surface energy budget has proven difficult because of a lack of understanding of their key physical properties [*Stephens*, 2005].

Along with its already complex nature, climate scientists have still yet to understand how sensitive MSc are to anthropogenic changes, such as greenhouse gas-induced warming or an increase in aerosol concentrations, and therefore how such clouds will play a role in further perturbing the Earth's climate [*IPCC*, 2007]. While numerous studies have found that MSc are sensitive to aerosol concentration (Fig. 1.3), the sign of these changes is unsettled [*Albrecht*, 1989; *Charlson et al.*, 1992; *Pincus and Baker*, 1994]. It is likely, then, that changes in MSc are already occurring because globally averaged temperatures (including sea surface temperatures) and aerosol concentrations have been increasing for decades, which makes quantifying their influence on climate even more difficult [*Bony et al.*, 2006; *Cronin et al.*, 2006; *Wyant et al.*, 2006; *Bony and Dufresne*, 2005].

Bretherton et al. [2004] suggest that the impact of MSc on the climate system, and their uncertainties, have been difficult to quantify because they are maintained by a combination of physical processes that are too complex to parameterize until more is learned about their dynamics. The primary physical processes of the marine boundary

Figure 1.4: View of MSc from the coast
This image depicts a classic view of the Pacific, as seen from most coastal towns on the West Coast, during the summer months. The photo, taken at Cape Disappointment State Park and capturing the MSc off the coast of Washington state, also highlights the low-lying nature of the marine layer near the coastline. Photo credit: http://5starcampgrounds.com/wp-content/uploads/Cape-Disappointment-State-Park-Washington-marine-layer.jpg

layer (MBL) are depicted in Fig. 1.5 and the estimated timescales for each process is listed in Table 1.1.

Typical MSc cloud regimes are associated with a number of standard features. Cold and wet conditions below are met by warm and dry conditions above, creating pronounced thermal and moisture contrasts between the MBL and the free troposphere which lead to MSc formation. Cold and wet conditions below are produced when upwelling along western margins of continents creates cold surface water. The warm and dry conditions above the MBL are associated with descending branches of the Hadley and Walker circulations. In the sub-tropics, this subsiding air joins the MBL to produce a strong inversion in both temperature and total water content and is most pronounced during the summer months. MSc clouds form within the MBL and are capped by the

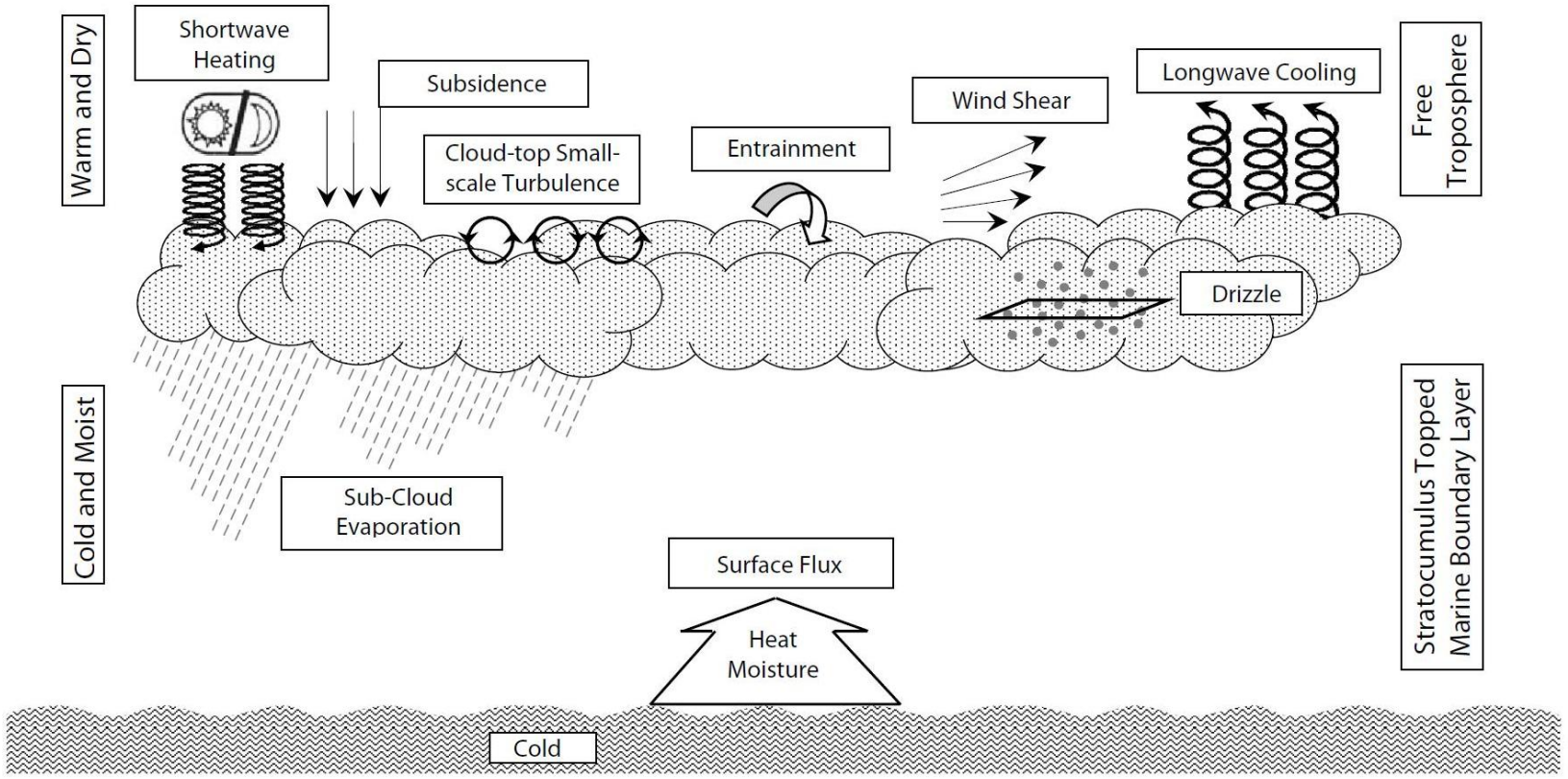

Figure 1.5: The primary physical processes of the STBL
Surface fluxes (moisture and heat), drizzle, evaporation, wind shear, SW heating, LW cooling, subsidence, cloud-top small-scale turbulence, and entrainment all play a role in MSc dynamics. A change in these processes will affect BL structure, microphysics, water budget, energy budget, and turbulence (modified from *Bretherton et al.*, 2004).

inversion above.

Process Timescale		MSc Response Timescale	
Forcing		**Forcing**	
MBL Turnover Time	30 min	Surface Fluxes	
Drizzle	2 hr	Moisture	10 hrs
Sub-Cloud Evaporation	10 min	Heat	∼1 day
Shear	∼1 day	Shortwave Heating	∼hours
Entrainment	∼1 min	Longwave Heating	1 hr
		Subsidence	1-2 days

Table 1.1: Estimated timescales for the MBL
Estimated timescales for the primary forcings found within the MBL were obtained by assuming a cloud depth of 300 m, BL depth of 650 m, and characteristic drop size of 40 µm.

Once the MSc layer is formed, BL physics is modified in two significant ways. First, the layer inhibits warming of the BL by reflecting incoming solar radiation that would otherwise warm the surface. As noted previously, the marine cloud's high albedo strongly contrasts with the low albedo of the dark ocean. This creates a positive feedback by inhibiting absorption of radiation to the ocean thus maintaining a cold ocean for sustained MSc. Secondly, because liquid water is such an effective emitter of LW radiation, air at the top of the BL is cooled and subsequently sinks. Consequently, cloud top cooling produces significant turbulence within the entire MBL. The mixing generated by buoyancy production at cloud top helps maintain a well-mixed BL and the MSc layer.

Figure 1.6 shows idealized vertical profiles for different atmospheric variables within a Sc-topped MBL. Total water mixing ratio, q_T, is the sum of the water vapor, liquid, and solid mixing ratios. Equivalent potential temperature, θ_e, is the potential temperature of a parcel of air when all the water vapor has condensed to liquid. It is clear from Fig. 1.6a and 1.6b, that the MBL is moister and colder than the free troposphere above and that q_T, and θ_e are constant under their inversions. The virtual potential temperature, θ_v, is the potential temperature of a parcel of air if the dry air had the same density as the moist air. The use of θ_v is a way to refer to changes in temperature without having

to refer to changes in density due to changes in moisture. Therefore, θ_v can be used to measure buoyancy and, unlike q_T and θ_e, is not constant within the idealized MBL (Fig. 1.6d).

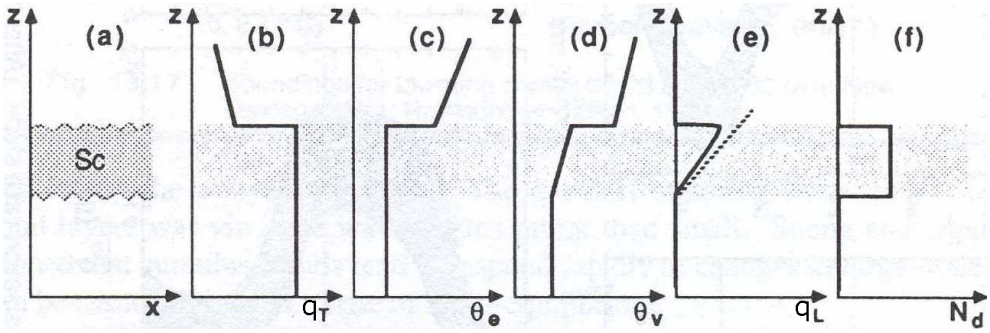

Figure 1.6: Idealized profiles of mean variables within a STBL
(a) cloud location, (b) total water mixing ratio, (c) equivalent potential temperature, (d) virtual potential temperature, (e) liquid water mixing ratio (dashed line indicates the theoretical adiabatic value), and (f) number density of drops. (From *Stull*, 1988 p. 570)

Liquid water mixing ratio, q_L, is the mass of liquid water per unit mass of dry air and thus will reflect variations in liquid water content (LWC). Due to condensational growth of cloud droplets, q_L, increases more-or-less linearly with height in cloud (Fig. 1.6e). q_L and LWC do not tend to follow adiabatic values (the dotted line in Fig. 1.6e) because of entrainment of dry air from above. Even though LWC increases with height, the idealized profile of drop number density remains constant (Fig. 1.6f). This arises because cloud droplets are larger higher in the cloud. Two other BL measurements important to the study of the MBL are vertical velocity variance, $(w')^2$, and shear strength, dv/dz. $(w')^2$ is the mean-square deviation from the mean of the vertical velocity, w, and is a measure of BL turbulence. dv/dz is a measure of variation in the horizontal wind vector with altitude and is used to study the influence of wind shear on BL dynamics, particularly at cloud top.

1.1.2 Cloud microphysics

On a much smaller scale, cloud microphysical parameters, such as cloud droplet size and concentration, are important for several reasons. First, they control how clouds radiatively impact the atmosphere—that is, how they interfere and transmit solar and terrestrial radiation. These parameters also determine the LWC of a cloud and therefore influence the latent energy balance of the atmosphere. Lastly, cloud microphysics determines the lifetime of a cloud. Cloud microphysical processes begin with the formation of water droplets onto cloud condensation nuclei (CCN) and end with the precipitation or evaporation of the cloud.

When air becomes supersaturated, water vapor condenses onto available CCN. Condensational growth can produce drops up to 20 μm diameter. Cloud droplet growth for drops greater than 20 μm is dominated by collision/coalescence. This is the process by which cloud droplets collide with each other and combine to form larger drops. Often this occurs when drops larger than their neighboring drops, and thus with larger fall speeds, sweep up smaller drops that lie in their path. The collision-coalescence growth rate increases rapidly with size; once the process begins, it becomes quite easy for drops to grow. [*Rogers and M.K Yau*, 1989]

Once a cloud is formed, competing processes govern how the cloud will evolve. For example, some processes may promote droplet growth, remove BL moisture, increase BL kinetics, or cause MSc thinning, while other processes do just the opposite. As these processes act simultaneously, so do their feedbacks, enhancing or inhibiting cloud responses. This research focuses on three of these processes: (1) the flux of water moving through the cloud due to the sedimentation of drops, (2) the evaporation of drops under the cloud base and (3) the modification of the cloud droplet spectrum due to drop collisions.

1.2 General methodology

1.2.1 Instrumentation

This research utilizes an Artium Flight Phase Doppler Interferometer (F-PDI) probe [*Bachalo*, 1980; *Bachalo and Houser*, 1984; *Chuang et al.*, 2008]. The F-PDI, shown in Fig. 1.7a, fundamentally measures individual cloud droplet size and velocity from which size distributions of drop number, terminal velocity, mass, etc. can be derived. One of the advantages of the F-PDI relative to other instruments is its accurate cloud drop size distribution measurements across a wide range of sizes, 2 to 100 µm diameter. Traditionally, the upper portion of this size range, ∼30 to 100 µm, has been difficult to measure well, and it is of particular importance to the initiation and evolution of drizzle. All of the work presented here advances cloud microphysics for this reason alone; much of the research performed would not have been possible, or possible to the extent of the accuracy we present, without the use of the F-PDI. Further details regarding the F-PDI can be found in *Chuang et al.* [2008].

Figure 1.7: UCSC F-PDI probe and the CIRPAS Twin Otter

To capture the whole range of drop sizes important for drizzle, drop size measurements from the Cloud Imaging Probe (CIP) are merged with those from the F-PDI. Data retrieved from the F-PDI was utilized for drop diameter, $D < 98$ µm, above which the

CIP data is used, with a maximum size of 1562 µm. Due mostly to the optical properties of the probe, specifically, the shadow threshold intensities within the depth-of-field, studies show the CIP is susceptible to counting and sizing errors for spherical particles [*Joe and List*, 1987; *Korolev et al.*, 1998; *Reuter and Bakan*, 1998]. *Strapp et al.* [2001] present sizing and counting measurements for monodisperse particles as a function of particle size and speed. We reconstruct CIP drop size distribution, accounting for oversizing and overcounting, by implementing two correction factors derived from *Strapp et al.* [2001]. For drops traveling at 50 m/s, the average speed of the aircraft, sizing biases ranged between 14 and 5% for drops ranging from 89 to 512 µm and concentration biases ranged between 44 and 56% for drops ranging from 89 to 121 µm, respectively. By combining the F-PDI for drop sizes between 2 to 98 µm, and the CIP from 98 to 1562 µm, we cover the range of drop sizes expected to be relevant to the range of conditions from non-drizzling to heavily drizzling. The transition from one instrument to the other at ∼100 µm is helpful in detecting problems with one (or both) of the instruments; ideally the two distributions merge smoothly with no obvious bias. We will examine this question in more detail in Sect. 2.3.3.2.

1.2.2 Project description

The aircraft measurements used in this study come from *in situ* observations taken from a combination of instruments onboard the Center for Interdisciplinary Remotely-Piloted Aircraft Studies (CIRPAS) Twin Otter (Fig. 1.7b) during the MArine Stratus/Stratocumulus Experiment (MASE) in July 2005. The flights specifically targeted MSc off the coast of California in the vicinity of Monterey, CA during the month in which the stratocumulus is at its maximum. The goal of MASE was to study the interaction between aerosol and cloud using state-of-the-art instrumentation within one of the world's most persistent stratocumulus decks (Fig. 1.2). For more detailed information

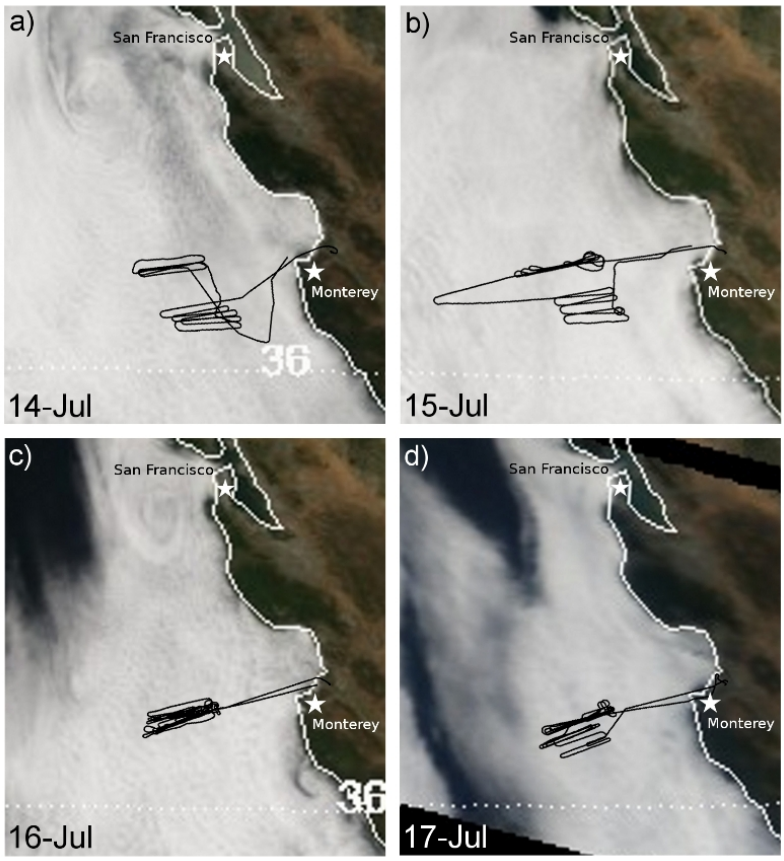

Figure 1.8: MASE satellite images with flight path
MODIS satellite images and Twin Otter flight paths for MASE Days 14, 15, 16, 17 (a-d, respectively)

on the MASE mission see *Lu et al.* [2007].

Thirteen flights were performed between approximately 17:30 and 21:00 UTC or 10:30 to 14:00 LT (local time = UTC -7h) and in the region 123.5 to 121.5^{o}W and 35.8 to 36.8^{o}N between 2-17 July, 2005. This study will focus on only four of those flight days: 14, 15, 16, and 17 July. For brevity, we will call these Day 14 to 17, respectively. These flights were chosen because they contained the most continuous F-PDI data sets during the MASE project. Figure 1.8 shows satellite images of the study area and the surrounding region taken from MODIS on Days 14-17 (a-d). All flights were carried out in a Lagrangian frame of reference, i.e. with the aircraft drifting with the mean wind,

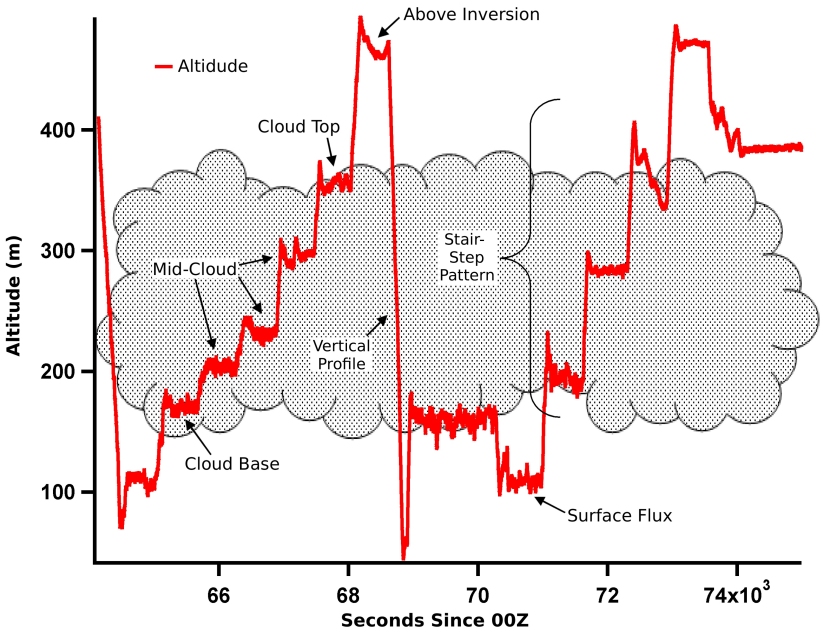

Figure 1.9: Typical stair-step pattern flight path
The CIRPAS Twin-Otter completed two stair-step patterns and two vertical profiles on this day, 14-July, 2005 during the MASE field experiment.

which maintains the aircraft in approximately the same volume of air for the duration of the observational period.

During each MASE flight, the aircraft flight pattern incorporated several stair-step patterns proceeding through the height of the STBL. This pattern begins with a surface level leg and proceeds through the MBL, taking consecutive steps of increased altitude. Figure 1.9 shows an example of a flight path where two stair-step patterns were performed back to back (Day 14). Level leg runs are performed at each step, starting below the cloud base and continuing through the cloud until reaching the inversion. In cloud, legs are performed at cloud base, at several levels within the middle of the cloud, and finally at cloud top. The flight paths can also occur in the opposite direction where the pattern begins above cloud top and ends below cloud base. This technique is useful because it allows for comparisons to be made between equal lengths of time, and therefore equal lengths of distance, at different levels within the cloud.

Average Level Altitude (m)

Level	**14-Jul**	**15-Jul**	**16-Jul**	**17-Jul**
CT	370	398	390	295
MC	290	299	258	192
CB	176	175	100	128

Table 1.2: Altitude of each flight level
The altitude, z, of each flight leg is dependent on the structure of the cloud, which may vary with time. Level-averaged altitudes for cloud top (CT), mid-cloud (MC), and cloud base (CB) for each of the four MASE study days are listed.

A second benefit of this technique is that comparisons of the same horizontal cloud layer can be made from cloud to cloud. This can be done regardless of changes in the cloud's vertical structure. The research presented in each chapter utilizes this feature. All data was divided into three levels, cloud top (CT), mid-cloud (MC), and cloud base (CB). Calculations are presented averaged over entire levels, which often incorporated data from several legs. The level-averaged altitude for each day are listed in Table 1.2. MC data includes all flight legs which took place 50 m above and below the geometric center of the cloud. This eliminated flight legs which occurred near cloud top or cloud base flight legs. Also, vertical profiles from below cloud to above cloud (and vice versa) are routinely performed during each flight (Fig. 1.9). Both of these flight techniques allow for a fine-scale analysis of cloud properties through time and space, in both the horizontal and vertical. Each level leg is approximately 30 km in length, which, assuming a maximum eddy size equal to the boundary layer depth ($\sim$1 km), represents a distance corresponding to tens of boundary-layer eddies.

Chapter 4 includes additional contributions from Physics Of Stratocumulus Tops (POST) campaign which took place in in July-August 2008 off of the coast of California and VAMOS Ocean-Cloud-Atmosphere-Land Study (VOCALS) campaign which took place in November 2008 off of the coast of Chile [*Wood et al.*, 2011]. Data from these campaigns were used to broaden the breadth of the results found in Chapter 4, as they

both investigated the summer-time MSc over the Pacific.

1.2.3 Aircraft measurements

The suite of instruments onboard the Twin Otter measure aerosol, cloud thermodynamic, meteorological, and radiometric properties of the atmosphere. This study utilizes the temperature, dew point and pressure, as measured by standard meteorological instruments, to calculate other important boundary layer parameters (potential temperature, virtual potential temperature, water vapor mixing ratio, specific humidity, etc). This study utilizes the 1 Hz (50-m) data. The turbulence gust probe, from which vertical and horizontal wind speed is derived, was not functioning properly and therefore no turbulence studies could be preformed. As mentioned previously, CIP data was combined with F-PDI data to produce complete drop size distributions, drizzle size distributions, and LWC measurements.

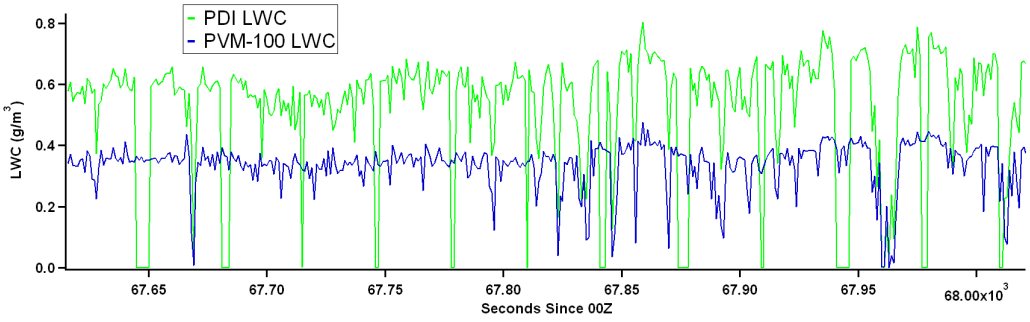

Figure 1.10: PVM-100 and F-PDI LWC
The PVM-100 and F-PDI LWC show good comparison. PVM-100 measured LWC is lower than F-PDI derived LWC because of the low efficiency at which the PVM-100 samples liquid water at large drop sizes [*Gerber et al.*, 1994].

The Gerber Scientific Particle Volume Monitor-100 (PVM-100) was used to cross-check the F-PDI by comparing derived LWC. Figure 1.10 shows a time series comparison

of F-PDI derived LWC with PVM-100 measured LWC for a cloud top leg on Day 14. The PVM-100 measured LWC is consistently lower than F-PDI derived LWC because of the low efficiency at which the PVM-100 samples liquid water at large drop sizes [*Gerber et al.*, 1994]. Several PVM-100 efficiency curves have been introduced to account for the decrease in sampling efficiency [*Gerber*, 1991; *Wendisch et al.*, 2002; *Chuang et al.*, 2008], with *Chuang et al.* using F-PDI derived LWC from MASE to produce the most optimal efficiency curve for these clouds (see reference for more information). Figure 1.10 also shows the F-PDI LWC dropping to zero every 30 s. Because of the high volume of drops measured by the F-PDI each second, the F-PDI processor requires a second every 30 seconds to store Sc drop data. The drop to zero is an artifact of the F-PDI and should not be considered real. Taking into consideration these two differences in LWC data, Fig. 1.10 shows good comparison at 1 Hz between the two LWC, with the temporal behavior of the curves tracking each other very well. Similar agreement is found over all field campaigns.

1.3 MASE clouds, Days 14-17

1.3.1 Mean conditions

Table 1.3 shows a summary of the cloud properties for Days 14-17. Cloud top and cloud base altitudes, z, were averaged over all ascends and descends in and out of cloud through the length of the flight. Cloud thickness, H, was derived directly from CT and CB altitudes. Superscript minus ($^-$) next to measurements of H denotes the cloud was thinning through time. Considering the average F-PDI drop concentrations, N, from each flight level, the largest N value for each day is listed in Table 1.3. Our attempt was to present a measurement of drop concentration which was least affected by collision-coalescence

or entrainment (this most often refers to mid-cloud N). Aerosol concentrations, N_a, were measured by the Condensation Particle Counter (CPC) and were averaged over all sub-cloud legs for each day. LWC values are specifically F-PDI derived CT LWC. Two F-PDI derived drizzle rate, R , values are presented: CB R and CB R only considering $D > 40$ µm, R_{40}. Sea surface temperature, SST, was measured from a Heitronics KT 19.85 Pyrometer and was averaged over all sub-cloud legs for each day. The jump in equivalent potential temperature, $\Delta\theta_e$, presented in Table 1.3 is a measure of the largest $\Delta\theta_e$ between a 50 m altitude range at the inversion. $\Delta\theta_e$ is derived from measurements obtained by temperature (Rosemount 102EAL), pressure (SETRA transducers), and humidity (EDGETECH EG&G Chilled Mirror) sensors. The jump in total water mixing ration at cloud top, Δq_T, was derived in a similar manner as $\Delta\theta_e$ and is a combination of the PVM-100 measured LWC and humidity measurements from the EDGETECH EG&G Chilled Mirror.

	Day 14	Day 15	Day 16	Day 17
Date	14 July 2005	15 July 2005	16 July 2005	17 July 2005
UTC flight time (SSM)	64380 - 73560	72180 - 75240	74940 - 77280	69840 - 73980
CT (m)	350 ± 63	340 ± 19	350 ± 11	280 ± 21
CB (m)	160 ± 32	110 ± 29	130 ± 39	98 ± 14
H (m)	190 ± 71	230 ± 34$^-$	220 ± 41	180 ± 25$^-$
N (#/cm^3)	97 ± 53	151 ± 40	120 ±35	133 ± 24
N_a (#/cm^3)	720 ± 340	450 ± 330	480 ± 24	490 ± 610
LWC (g/m^3)	0.45 ± 0.23	0.45 ± 0.29	0.43 ± 0.26	0.33 ± 0.28
R (mm/day)	0.57 ± 2.6	0.24 ± 0.37	0.32 ± 1.7	0.10 ± 0.12
R_{40} (mm/day)	0.52 ± 2.6	0.08 ± 0.38	0.29 ± 1.7	0.05 ± 0.18
SST (°C)	14.0 ± 1.0	14.4 ± 0.8	14.7 ± 0.2	15.7 ± 0.3
$\Delta\theta_e$ (°C)	4.6	6.4	9.0	7.0
Δq_T (g/kg)	1.9	1.6	3.3	2.2

Table 1.3: Summary of cloud properties
Summary of mean cloud properties for each of the four MASE days, 14-17. See text in Sect. 1.3.1 for variable name and the process by which each property was determined.

Data presented in Table 1.3 shows small variation in H and data presented by *Lu et al.* [2007] show Days 14-17 contained the geometrically thinnest clouds during the MASE project. Day 14 and 16 were strong drizzling cases while Day 15 and 17 exhibited weaker drizzle rates. Cloud depth affects drizzle in a positive sense, therefore H is reflected in R. The exception to this is Day 15, which is thick but exhibits low drizzle rates. In Chapter 2, we will show Day 15 to be a less diluted cloud, containing large mean drop sizes at all levels within the cloud, suppressed drizzle, and large N, as shown in Table 1.3. Sub-cloud aerosol concentration show that Days 15, 16, 17 contained moderate background aerosol counts ($\sim$490-500 cm^{-3}) while Day 14 showed slightly higher aerosol counts ($\sim$720 cm^{-3}). N_a does not show any obvious relationship with average drop concentrations for these four days. N is high for Days 15 and 17; in fact, *Lu et al.* [2007] show these two days have the highest drop concentrations out of the 13 flights.

1.3.2 General cloud characteristics

Figures 1.11 and 1.12 give a general overview of the observed cloud properties with time for Days 14-17. The uppermost panel in Fig. 1.11 shows potential temperature, θ, and PVM-100-measured LWC, while the lowermost panel shows z and F-PDI N as a function of time. Profiles of q_T (top axis) and θ_e (bottom axis) are shown in Fig. 1.12 and can be compared to the idealized profiles shown in Fig. 1.6. Cloud top and cloud base heights along with cloud thickness, as listed in the Table 1.3, are also plotted on Fig. 1.12. Using these two figures, the basic features of a MSc can be observed. For example, both LWC and N increase with z in Fig. 1.11. Figure 1.12 shows q_T and θ_e are relatively constant throughout the layer, indicative of a well-mixed (coupled) boundary layer. The exception to this is Day 17 where a jump in moisture below cloud base is evidence of a decoupled sub-cloud layer. q_T on Day 15 drops off much more slowly above

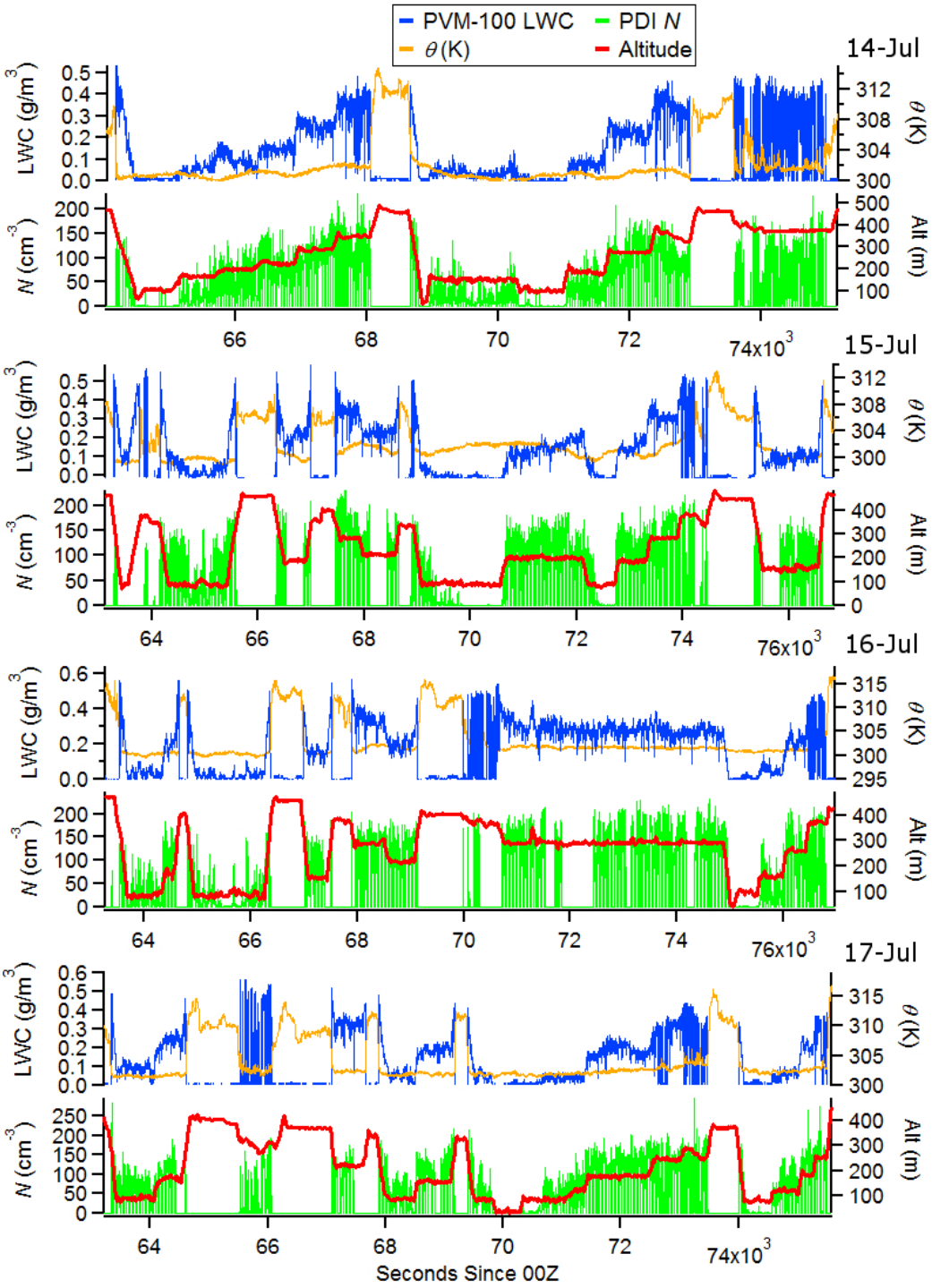

Figure 1.11: Time-series of basic cloud properties

A time series of basic cloud microphysical properties for MASE Days 14-17, top to bottom, respectively. The uppermost panels show a times series of LWC and θ, while the lowermost panel shows z and F-PDI N.

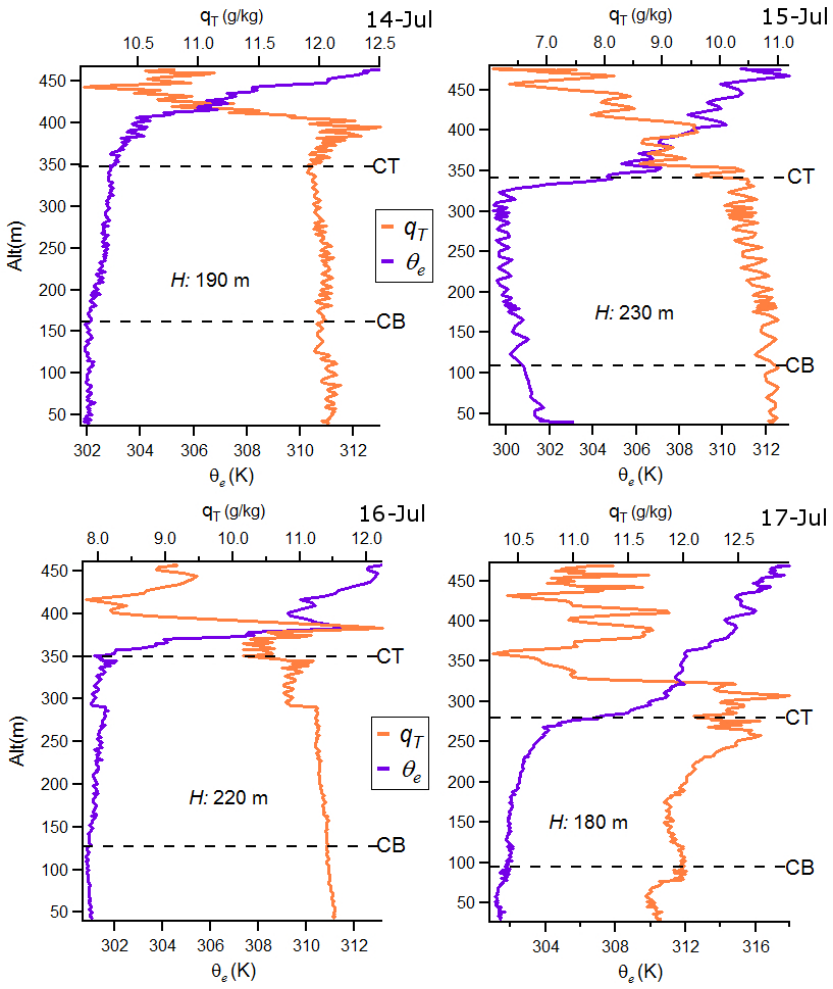

Figure 1.12: Profiles of θ_e and q_T

Profiles of equivalent potential temperature, θ_e, and total water mixing ratio, q_T, for Days 14-17. The location of cloud base and cloud top are also marked. Here, "CB" and "CT" refer to the location of the physical cloud top and cloud base whereas, in the text, CB and CT refer to the level of flight leg.

cloud top than it does during all other days, while Day 16 exhibits anomalous jumps to lower q_T near cloud top and an accompanying pocket of moist air above cloud before falling off to normal free-tropospheric values. The intersection of moist air just above the MBL has been hypothesized to play a role in the formation and growth of drizzle within the cloud layer [*Stevens et al.*, 2005]. Day 16 is, in fact, a strong drizzling case, along with Day 14, while Day 15 and 17 exhibit weaker drizzle rates (see Chapter 2 for

more a detailed presentation of daily R).

While each MODIS image in Fig. 1.8 shows the flight paths moved through an unbroken cloud deck, a closer look reveals differences the brightness, reflecting difference in the structure, between the days. Microphysical data supports these difference (Table 1.3 and results in Chapter 2). The MODIS satellite image from Day 17 shows seemingly no cellar structure at all; the cloud appears thin with wide-spread breakup just to the west and north of where the plane sampled. These observations are consistent with previous results which show Day 17 contains the thinnest MASE cloud [*Lu et al.*, 2007]. Microphysical measurements presented in Chapter 2 confirm that Day 17 is the least developed cloud, containing the smallest drops at all cloud levels and showing no evidence for drop growth from cloud top to cloud base (collision-coalescence). The MODIS images from Day 15 shows more of a cellular environment to the west of the flight path and a less structured, more uniform cloud environment in the area of the flight path. Day 15 appears brighter and more solid than Day 14, consistent with a more diluted cloud with a large mean drop diameter. The satellite image shows cloud breakup in the upper left corner of Day 16; the cloud-free region is surrounded by wispy, thin clouds. Day 14 and Day 16, the most drizzling days, show evidence for a cellular environment in the region in which the plane sampled.

1.4 Summary

In summary, this research utilizes the PDI probe in combination with the CIP probe to derive high rate size distributions of drop number and drizzle rate through the summertime MSc off the coast of California for four days, MASE Days 14-17. These measurements, in conjunction with other simultaneous aircraft measurements, will be used to create a comprehensive set of data and a quantitative analysis of the relationship between

MSc clouds and the water and energy budgets of the MBL. This work is important, in short, because MSc control the radiation budget in large areas of the world's subtropical oceans. This means that exploring and evaluating their involvement within the MBL is crucial for understanding the present global climate. While the Earth's climate system faces anthropogenic perturbations from dozens of forcing and feedbacks (some even possibly unknown) at unprecedented rates, the attempt to unravel each component of the climate system, including that of the MSc regime, is imperative.

Chapter 2

The structure and variability of drizzle in marine stratocumulus clouds

Marine stratocumulus (MSc) clouds control the radiation budget in large areas of the world's subtropical oceans. The properties of such MSc clouds depend on the water and heat budgets of the marine boundary layer (MBL). Drizzle, defined as the redistribution of cloud droplets through sedimentation, directly affects Sc properties such as cloud lifetime and albedo. Drizzle also indirectly impacts Sc via feedbacks to other primary processes involved in the Sc topped MBL. Although the effects of drizzle on the system are widely acknowledged, there remain many outstanding questions regarding its quantitative impacts on the system and its structure within cloud. Here, we report in situ aircraft measurements of the size-resolved drizzle rates in marine Sc using the Artium Flight Phase Doppler Interferometer (F/PDI) and the Cloud Imaging Probe (CIP) during the Marine Stratus Experiment (MASE) in July 2005 in the northeastern Pacific near Monterey, California. Statistics indicate two microphysical regimes exist, a high drizzle

regime and a low drizzle regime. High drizzle regimes are associated with patches of heavy drizzle, occurring in clusters with a typical length scale of 1 to 10 km, and exhibit variability in R at all levels of the cloud. This is in contrast to light drizzle regimes, which are associated with more uniform, light-to-no drizzle. The presence of a small fraction of large, collisionally-formed drops at cloud top appears to be a very strong indicator of how drizzle will develop through the cloud. We show that drop growth can not be explained by simple gravitational sedimenation of the largest CT drops and suggest other mechanisms for growth, such as turbulence. The predictability of the structure (vertical and horizontal) and variability of drizzle may lead to further developments in distinguishing how other key microphysical processes control Sc evolution. Furthermore, because these processes, including drizzle, control cloud properties, the findings described in this study make advancements towards understanding the interaction between Sc and the larger climate system.

2.1 Introduction

Marine stratocumulus (MSc) clouds which reside over the eastern subtropical oceans play a key role in regulating global and regional climates. MSc are vast, persistent, highly reflective (α = 0.4-0.8), exist in environments sensitive to cloud cover, and recently, have been found to play a role in El Niño–Southern Oscillation. Even still, attempts at modeling MSc accurately are thwarted by the array of complex processes that govern their radiative properties, spatial structure, and lifecycle. This research specifically focuses on the microphysical processes of the Sc-topped boundary layer (STBL). Quantifying the effects of microphysical processes are especially difficult as tight feedbacks exist between them and as they have been shown to be sensitive to fluctuations in external forcing, such as above-cloud moisture and aerosol concentrations. Recently, the important role of drizzle on the dynamics of the STBL has become a greater focus of

research. Numerous studies have found that the flux of energy associated with drizzle is similar in magnitude to other energy fluxes within the boundary layer [*Nicholls*, 1984; *Austin et al.*, 1995; *Bretherton et al.*, 1995; *Duynkerke et al.*, 1995; *Frisch et al.*, 1995; *Boers et al.*, 1996; *Vali et al.*, 1998] such as surface heat fluxes and entrainment fluxes. More obviously, drizzle can be a significant process by which moisture is redistributed to the sub-cloud layer when drizzle evaporates, and possibly lost from the system altogether if it reaches the surface. More recent observations suggest that the occurrence of significant drizzle is much higher than formerly thought [*vanZanten et al.*, 2005]. In the past, underestimated drizzle rates were partially due to instrument limitations in accurately measuring the complete spectra of drop sizes from a few microns in diameter rain drops to millimeter-size rain drops. Accurately quantifying the total amount of drizzle moving through the cloud is important because cloud water loss due to drizzle affects the structure of the cloud (thickness, coverage, and liquid water path), cloud top cooling, turbulence within the boundary layer, the entrainment rate, the evaporation of precipitation, and the albedo of the cloud, subsequently affecting the net heating of the cloud layer. The research presented here is unique because we calculate drizzle rates across a large range of drop sizes (from 2 µm up to ∼1.5 mm) with much better accuracy and precision than previously possible.

Cloud averaged drizzle rates are not sufficient to characterize drizzle in Sc. *vanZanten et al.* [2005] warned that large flight-averaged drizzle rates were mostly a result of large localized drizzle rates while *Austin et al.* [1995] found that patches of heavy drizzle exceeded the cloud base average over a 700 km flight leg by a factor of 10. Horizontal variability is relevant to STBL evolution because high precipitation values can lead to convective instability, weaker circulation, and diminished STBL moisture (via loss by precipitation and suppressed vapor flux) leading to Sc breakup [*Paluch and Lenschow*, 1991; *Feingold et al.*, 1996; *Stevens et al.*, 1998; *Jensen et al.*, 2000; *Comstock et al.*, 2004; *Wood*, 2005]. Although horizontal patchiness has been documented in a number

of past studies [*Austin et al.*, 1995; *Vali et al.*, 1998; *Stevens et al.*, 2003; *Comstock et al.*, 2004, 2005; *vanZanten et al.*, 2005; *Wood*, 2005], there is still no predictive theory for the horizontal structure and variability of drizzle. Also, because drizzle formation in stratocumulus is primarily (though not exclusively) a vertical process, the vertical structure and organization of drizzle is important to understanding its development [*Austin et al.*, 1995; *Feingold et al.*, 1996; *Vali et al.*, 1998; *vanZanten et al.*, 2005]. Along with high-rate localized drizzle rate measurements in the horizontal and vertical, another way to characterize drizzle is through its size distribution. The size distribution of drizzle is important because of its relevance to a number of key processes. For example, drop-drop interactions (such as collision-coalescence) within the cloud are strongly dependent on drop size, and therefore the development and evolution of drizzle itself is size-dependent.

This work focuses on the microphysics of drizzle in MSc. In order to understand the state, evolution, and impacts of drizzle within the cloud, the horizontal and vertical structure of drizzle is examined in detail. Section 2.2 of this work describes the instruments used to retrieve cloud drop data, the project from which the data is retrieved, and how drizzle rates are calculated. Section 2.3 presents measurements of cloud number distributions, drizzle rates, drizzle rate distributions, and drizzle rate statistics in horizontal and vertical space. Implications for STBL evolution is also discussed within the Sect. 2.3.

2.2 Methods

2.2.1 Instrumentation and Aircraft Measurements

The MArine Stratus/Stratocumulus Experiment (MASE) was a field campaign specifically targeting MSc off the coast of California in the vicinity of Monterey, CA in July

2005. The research presented here utilizes cloud drop size distributions (DSD) data for computing drizzle rates necessary for this study. To capture the whole range of drop sizes, drop size measurements from the Artium Flight Phase Doppler Interferometer (F-PDI) (D $<$ 98 µm) were merged with those from the Cloud Imaging Probe (CIP) (98 $<$ D $<$ 1562 µm). Both instruments flew onboard the Center for Interdisciplinary Remotely-Piloted Aircraft Studies (CIRPAS) Twin Otter which was host to a collection of other cloud probing instruments. An introduction to the F-PDI, CIP, and other instruments as they relates specifically to this research can be found in Chapter 1. A detail description of the F-PDI can be found in *Chuang et al.* [2008] and a detail description of the CIP can be found in *Knollenberg* [1970]. A general overview of the entire MASE project can be found in *Lu et al.* [2007], while its specifics, as they relate to this research, can also be found in Chapter 1.

2.2.2 Drizzle Calculations

To calculate the size distribution of drizzle, the 1-Hz number drop size distribution (DSD), $\frac{dN}{d\log D}$, measured by the F-PDI and CIP is converted into a drizzle rate size distribution according to:

$$\frac{dR}{d\log D} = \frac{\pi}{6} D_i^3 \left(\frac{dN}{d\log D}\right)_i w_T\left(D_i\right) \tag{2.2.1}$$

where R is the drizzle rate and $w_T\left(D\right)$ is the terminal velocity. Equations given by *Pruppacher and Klett* (1197, pp. 416-419) are used to calculate fall velocity in three regimes: $1 \leq D \leq 20$ µm, in which $w_T \sim D^2$; $20 \leq D \leq 1070$ µm, in which $w_T \sim D$; and 1070 µm$\leq D \leq 7$ mm, in which drops cannot be considered spherical and increased drag resistance counteracts increased in gravitational force. It is important to note that only terminal velocity is used to calculate drizzle rate; the instantaneous vertical velocity is

ignored, consistent with most previous studies (e.g. *Nicholls*, 1984). This assumes that in-cloud velocities are turbulent and average to zero over a sufficiently long time, T, i.e. $\frac{1}{T}\int_0^T w dt = 0$ for large T. Summing the contribution to drizzle rate from all size bins yields the total drizzle rate for each second, i.e.:

$$R = \int_0^\infty \frac{dR}{d\log D} d\log D \tag{2.2.2}$$

Using each 1-s observation of R, we calculate averaged drizzle rates, $\overline{R}$, and produce a probability distribution function (PDF) of drizzle rate, PDF_R. For each 1-s observation of R, we also sum the contribution to drizzle rate from each bin size. This yields the total drizzle rate over the drop distribution for each second which we can then use to create average drizzle rate distributions. For each 1-s size distribution of R, we also compute the 10th, 50th, and 90th percentile sizes for this distribution , D_{10} ,D_{50} , and D_{90} respectively. We then generate the PDF of these values, $\mathrm{PDF}_{R,D10}$, $\mathrm{PDF}_{R,D50}$, and $\mathrm{PDF}_{R,D90}$.

2.3 Results

The overall goal in this study is to study the horizontal and vertical structure of drizzle in marine stratocumulus in cases spanning a wide range of mean drizzle rates. The horizontal structure of the cloud is examined by utilizing data retrieved during the level flight legs, which are divided into three levels: cloud top (CT), mid-cloud (MC), and cloud base (CB). MC data includes all flight legs which took place 50 m above and below the geometric center of the cloud. This eliminated flight legs which occurred near cloud top or cloud base flight legs. To understand the vertical structure of the cloud, and therefore the vertical evolution of cloud drops, we examine the differences among these

different horizontal legs.

Figure 2.1 gives a overview of the drizzle calculations for Days 14-17. These directly correlate with the general overview figure, Fig. 1.11, presented in Chapter 1. Two calculations of drizzle rate are plotted in the uppermost panel. The first only includes drops larger than 40 µm, R_{40}, which is a typical definition of drizzle (e.g. *Wood*, 2005; *Bretherton et al.*, 2007; *Lu et al.*, 2007; *Rasinski et al.*, 2011). The second method calculates R for drops of all sizes (unless otherwise stated, drizzle rate calculations herein include contributions from all drop sizes). The corresponding time series for drizzle rate D_{10} , D_{50} , D_{90}, and aircraft altitude are shown in the lowermost panel.

2.3.1 Number Distributions

The traditional measure of a cloud's microphysical state is its number size distribution. We therefore begin our analysis of Days 14 through 17 by exploring the contribution of different drop sizes to the concentration at each level within the cloud (Fig. 2.2). We also compare the DSD between the 4 days at each level. The number DSDs at cloud top (Fig. 2.2a) show very small daily variability in mode diameter, $D_{m,DSD}$. Table 2.1, which contains the distribution statistics for drop concentration, shows $D_{m,DSD}$ ranges between 19.0 and 19.7 µm. There is also very little difference in the general shape of the distributions among the 4 days. The geometric standard deviation, $\sigma_{g,DSD}$, values at cloud top (Table 2.1) are similar for each day, only ranging between 1.06 and 1.03. The differences in mode height between the 4 days reflect the differences in mean drop concentration, $\overline{N}$.

Moving down in the cloud, the number DSD at mid-cloud, similar to cloud top, have comparable shapes (Fig. 2.2b). $D_{m,DSD}$ for Days 14, 16 and 17 are nearly equal (15.8-16.4 µm) while that for Day 15 is larger (18.3 µm). Because the mode diameter of the number distribution is a function of height above cloud base, day to day variations

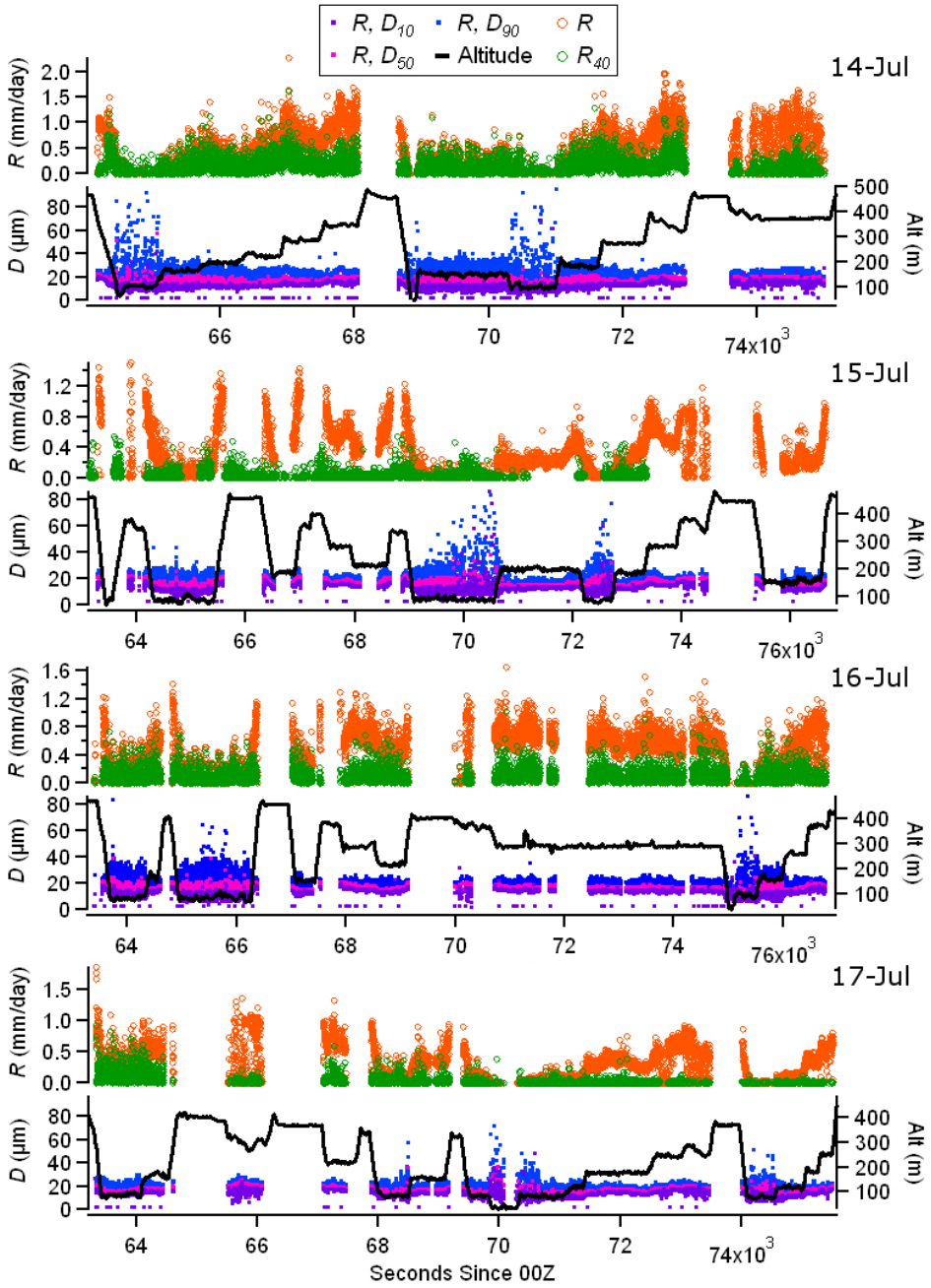

Figure 2.1: General drizzle time series data

A time series of drizzle rate data for MASE Days 14-17, top to bottom, respectively. The uppermost panels show a times series of R and R_{40}, drizzle only accounting drops larger than 40 µm. Drizzle rate D_{10} , D_{50} ,D_{90} and aircraft altitude are shown in the lowermost panels.

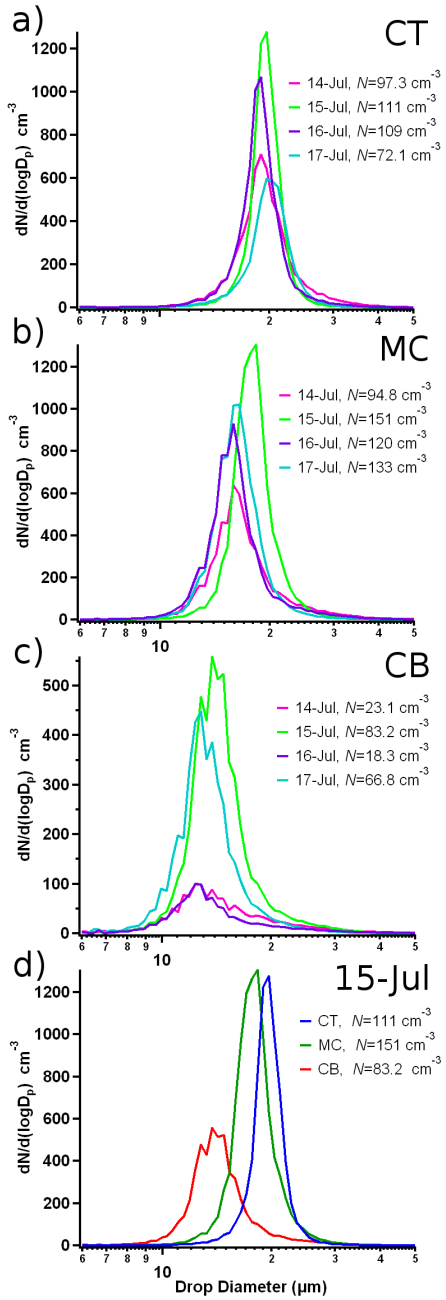

Figure 2.2: Number drop size distributions

MASE DSD for all levels, (a) CT, (b) MC and (c) CB. Daily sets of DSDs (like that shown in the last panel) look very similar to one another and therefore only Day 15 is presented. Corresponding level-averaged concentrations, N, are also presented on each plot.

in flight path can contribute to differences in mode diameters. For example, these include differences in the position of the plane relative to the estimated cloud top or cloud base and varying the altitude of the mid-cloud flight legs relative to cloud base. As described above, a systematic approach was taken to reduce this effect by only including legs which were 50 m in either direction of true cloud center. Considering the flight distribution statistics on Day 15 (Table 2.1), the difference between the mode diameters between Days 14/16/17 and Day 15 cannot be explained by altitude differences amongst mid-cloud sampling because the mid-cloud flight legs on Day 15 fall well within the range of altitudes (relative to cloud base) as sampled by the other three days (Table 1.2). Figure 2.7 indicates that Day 15 was high in LWC and high in drop concentration, suggestive of a less diluted cloud compared to the other three days, and which most likely accounts for the larger mode diameter. As at cloud top, the shapes of the DSD are similar with the mid-cloud σ_{DSD} values in Table 2.1 ranging only between 1.08 and 1.03.

	14-Jul	**15-Jul**	**16-Jul**	**17-Jul**
$D_{m,DSD}$ (µm)				
CT	19.0	19.7	19.0	19.7
MC	15.8	18.3	15.8	16.4
CB	12.8	13.7	12.3	12.8
$\sigma_{g,DSD}$				
CT	1.06	1.03	1.05	1.03
MC	1.08	1.03	1.05	1.03
CB	1.17	1.05	1.14	1.05

Table 2.1: Drop size distribution statistics
DSD statistics showing mode diameters, $D_{m,DSD}$, and geometric standard deviations, $\sigma_{g,DSD}$, for all days and levels.

Similar to the mid-cloud DSDs, cloud base $D_{m,DSD}$ for Days 14, 16 and 17 are again nearly equal (12.3-12.8 µm) while that for Day 15 is larger (13.7 µm). Because the mode diameter of the number distribution is a function of height above cloud base and because

the variations in the mode diameters are small, differences in the number distribution due to varying flight base altitudes are assumed to be negligible. $D_{m,DSD} > 10$ µm also suggest that the flight legs were not flown directly above the physical cloud base but at an altitude at which drops were already well-developed. Unlike the cloud top and mid-cloud number DSD, the DSDs at cloud base show two very distinct shapes (Fig. 2.2c). The mode heights on Days 14/16 are shorter, corresponding to smaller average total concentrations, than the mode heights on Days 15/17, and the $\sigma_{g,DSD}$ values are larger on Days 14/16 (1.17/1.14) compared to Days 15/17 (both 1.05, Table 2.1).

A closer look at Table 2.1 reveals a slight separation between $\sigma_{g,DSD}$ on Days 14/16 and Days 15/17 beginning at cloud top and becoming more pronounced moving down in the cloud. It is not apparent that this separation is meaningful (differences in $\sigma_{g,DSD}$ between Days 14/16 and Days 15/17 range only between 3-5%) until cloud base. It is nearly impossible to see variations in the widths of the distributions in Fig. 2.2a-c, even at cloud base when $\sigma_{g,DSD}$ differences are largest. It is only until Days 14/16 undergo a significant reduction in mode height before a separation between Days 14/16 and Days 15/17 become apparent. Based on these findings, we conclude that the two distinct DSD shapes at cloud base are real; the DSD and their statistics reveal the development of two microphysical regimes, one occurring on Days 14/16 and the other on Days 15/17. These results also suggest a mechanism for a reduction in drop concentration discernible only at cloud base.

Figure 2.2d shows the DSD for each flight level during Day 15. The shape and behavior of the DSDs are similar for all 4 days (not shown; statistics are available in Table 2.1). Although we have discussed the daily differences in drop distributions for each level by starting at cloud top and moving down to cloud base (Fig. 2.2a-c), when thinking about the level-by-level differences in distribution for each day (Fig. 2.2d), it is appropriate to discuss the shapes of the distributions from cloud base moving up to cloud top. The distributions in Fig. 2.2d are typical for drops which form at cloud base

and undergo condensational growth as they move up through the cloud, increasing mode diameter from cloud base to cloud top. Drops grow to ∼20 µm at cloud top. A few of the largest drops will fall through the cloud, growing even more as they collide with smaller drops. Collision-coalescence causes a reduction in the drop concentration (note the change in y-axis from Fig. 2.2b-c) and an increase in the widths of the distributions at the larger drop sizes at cloud base. As stated, the DSDs for each day are typical and similar amongst all days but the day to day differences in DSD, especially the separation between Days 14/16 and Days 15/17 at cloud base, are interesting. We further our analysis of MSc by calculating in-cloud drizzle rates as described in the methods section. Sections 2.3.2 and 2.3.3 describe how calculated drizzle rates show more complex differences between Days 14/16 and 15/17, and an investigation of the structure of drizzle, horizontally and vertically, between different days and cloud levels reveals possible cloud processes responsible for the divergence of data found between Days 14/16 and 15/17.

2.3.2 Horizontal Structure of Drizzle

Numerous cloud studies, using both *in situ* instruments and cloud radar, have shown that large horizontal variations in drizzle rate exist [*Paluch and Lenschow*, 1991; *Feingold et al.*, 1996; *Stevens et al.*, 1998; *Jensen et al.*, 2000; *Comstock et al.*, 2004; *Wood*, 2005]. Studies have also shown that large localized drizzle rates can impact the dynamics of the boundary layer to the point of MSc breakup [*Paluch and Lenschow*, 1991; *Feingold et al.*, 1996; *Stevens et al.*, 1998; *Jensen et al.*, 2000; *Comstock et al.*, 2004; *Wood*, 2005]. Therefore, it is important to study the horizontal behavior of drizzle in MSc in order to determine (a) the extent to which variability exists and (b) the role it has on the development of the clouds. The horizontal structure of drizzle on the 4 days sampled varied from day to day, within each cloud, and within each level. We begin our analysis

of the horizontal variability of drizzle using Fig. 2.3 and Table 2.2. Seven hundred seconds of cloud top, mid-cloud, and cloud base drizzle rate data are plotted for Day 14 (Fig. 2.3a), the day with the highest mean drizzle rate at all levels within the cloud, and Day 17 (Fig. 2.3b), the day with the lowest mean drizzle rate at all levels within the cloud. The insets show the PDF for all available drizzle rate data on the corresponding days, PDF_R. Mean drizzle rates, $\overline{R}$, standard deviations, σ_{PDF_R}, and mean drizzle rate over one standard deviation, $\overline{R}_{1\sigma}$, for all days and levels are listed in Table 2.2.

2.3.2.1 Daily variability

The day to day variation of horizontal drizzle is large and easily discernible from Fig. 2.3 and Table 2.2. For example, Table 2.2 reveals that Day 14 has a much larger σ_{PDF_R} than Days 15, 16, and 17. Similarly, Fig. 2.3 reveals that compared to Day 17, Day 14 has much larger variation in drizzle rate with time. The widths of the PDF_R distributions for all levels within the cloud (shown in the insets) are also larger on Day 14 than on Day 17. We conclude that Day 14 has the largest horizontal variability in drizzle rate compared to all other days. $\overline{R}_{1\sigma}$ (Table 2.2) shows that on Day 14, larger-than-average drizzle rates contribute significantly to this variability, especially at mid-cloud and cloud base. Visually, large patches of drizzle can be seen in Fig. 2.3a as vertical spikes that go beyond the scale of the y-axis. At cloud base (mid-cloud), $\overline{R}_{1\sigma}$ is 14.7 mm/day (13.0 mm/day) with a maximum observed R of 45.2 mm/day (20.8 mm/day). For comparison, cloud base R on Day 17 peaks at 2.43 mm/day with a $\overline{R}_{1\sigma}$ of 0.394 mm/day.

This data suggests a high drizzle day, like Day 14, may correspond to high horizontal variability containing patches of heavy drizzle throughout the cloud. Days with low drizzle rates, like Day 17, have overall low variability. Days 15 and 16 represent cases in-between Days 14 and 17. They have similarly moderate mean drizzle rates at cloud top and mid-cloud but then diverge at cloud base. The second largest drizzle rate

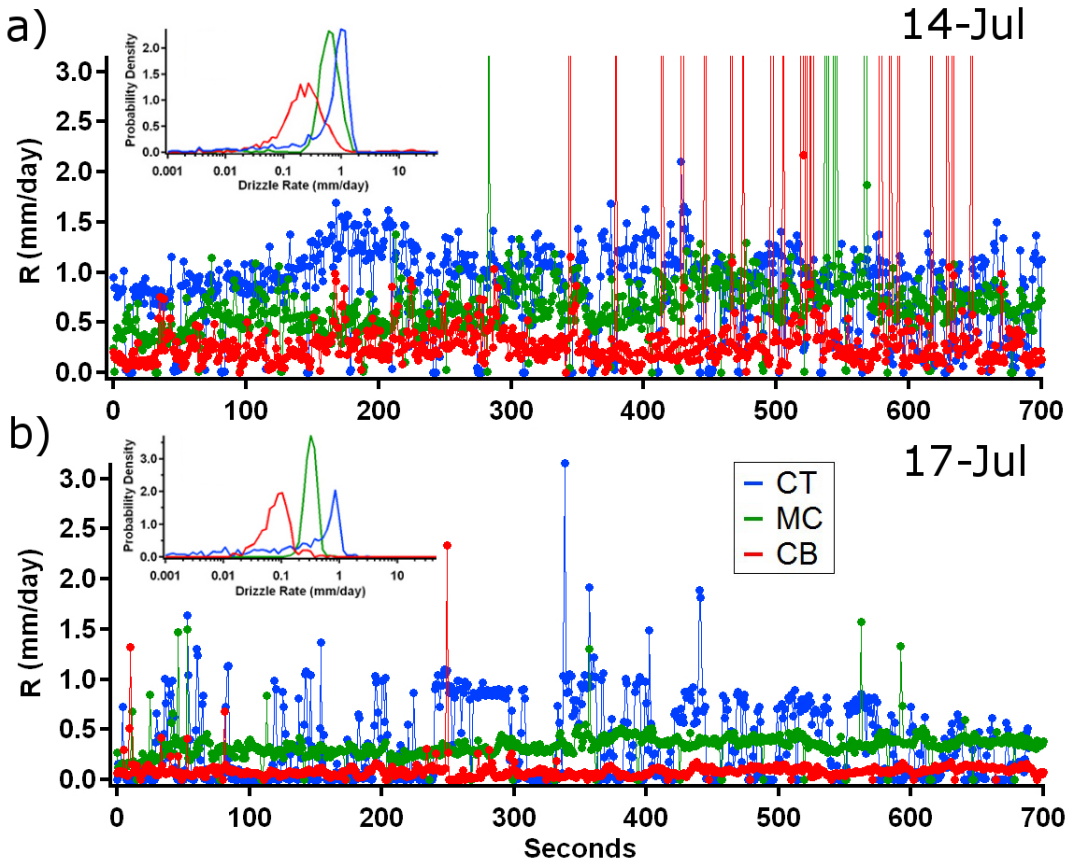

Figure 2.3: R time series and PDF_R
R time series and PDF_R shown as insets for Day 14 (a), the most drizzly day, and Day 17 (b), the least drizzly day.

at cloud base, which occurs on Day 16, corresponds to a large $\sigma_{PDF,R}$ and large $\overline{R}_{1\sigma}$, similar to Day 14. But unlike Day 14, these large values occur only at cloud base. One possible explanation for this is that drizzle is variable in time as well as space; the research flight could have passed through the cloud base during heavy drizzle but reached the mid-cloud level after or before strong drizzle production. We believe this scenario to be unlikely in this case. The flight pattern (Fig. 1.11) on Day 16 shows the airplane spent a significant amount of time sampling between the cloud base and mid-cloud levels. Because mid-cloud flight legs were performed before and after cloud base legs in which heavy drizzle was measured, it is unlikely the airplane could have missed a heavy drizzle

event while following a Lagrangian path. Another likely explanation we believe to be true suggests that patches of heavy drizzle at cloud base can develop in the lower half of the cloud and shafts of heavy drizzle penetrating the entire cloud, like those present Day 14, may only be unique to heavily drizzling clouds.

	14-Jul	**15-Jul**	**16-Jul**	**17-Jul**
$\overline{R}$ (mm/day)				
CT	0.758	0.519	0.553	0.437
MC	0.718	0.574	0.489	0.327
CB	0.569	0.244	0.324	0.098
σ_R				
CT	0.425	0.330	0.348	0.401
MC	1.09	0.165	0.147	0.107
CB	2.56	0.372	1.65	0.116
$\overline{R}_{1\sigma}$(mm/day)				
CT	1.34	0.891	0.992	1.01
MC	13.0	0.829	0.733	0.533
CB	14.7	2.14	8.51	0.394

Table 2.2: Drizzle statistics
Leg-averaged mean drizzle rates, $\overline{R}$, and drizzle PDF statistics, such as standard deviations, σ_{PDF_R}, and mean drizzle rates over one standard deviation, $\overline{R}_{1\sigma}$, for all days and levels.

Cloud base mean drizzle rate is moderately smaller on Day 15 compared to Day 16 but is better-developed than Day 17. Day 15 is similar to Day 17 in that it has very low cloud base variability compared to Days 14/16, as shown in $\sigma_{PDF,R}$ and $\overline{R}_{1\sigma}$. Day 15 stands out because drizzle rate is high in the mid-cloud layer; it is the only day which exhibits a higher mid-cloud $\overline{R}$ than at cloud top and oddly, mid-cloud $\overline{R}$ is larger on Day 15 than on Day 16, a day which is more drizzly at cloud base. Factors which may account for the high mid-cloud mean drizzle rate have been mentioned previously: Day 15 has been characterized as much less diluted cloud compared to the rest of the days;

it is high in LWC, high in N (Table 1.3), and has a significantly larger mode drop diameter than any other day (Fig. 2.2b).

2.3.2.2 Level by level variability

The horizontal drizzle structure varies from level to level within each cloud. Cloud top PDF_R always contain a significant tail on the left hand side of the peak (as illustrated in Fig. 2.3), corresponding to drizzle rates smaller than the mean. Unlike cloud base variability, where patches of heavy drizzle exist, cloud top variability appears to be comprised of patches of very low drizzle, which we attribute to entrainment drying combined with the aircraft occasionally leaving the cloud top. Cloud top entrainment brings dry air from above the inversion into the boundary layer, evaporating liquid water at cloud top. This will either cause cloud droplets to decrease in size or decrease the overall drop concentration, both of which reduce R. At times, cloud top legs were flown in and out of cloud. This would have increased the research flight's exposure to patches of cloud affected by entrainment and therefore increased variability at cloud top.

In the lower part of the cloud, PDF_R is always centered over smaller drizzle rates since condensational growth increases with altitude. In general, cloud base distributions are widest, corresponding to large $\sigma_{PDF,R}$ (Fig. 2.3 and Table 2.2), because they include a large proportion of small drizzle rates (< 0.2 mm/day) which cloud top and mid-cloud levels do not include. Values of $\overline{R}_{1\sigma}$ in Table 2.2 are also greatest at cloud base, showing the widest variability at large R. This is due to patches of strong collisional growth that have occurred during a falling drop's path to cloud base as shown by large spikes in Fig. 2.3a. Exception is on Day 17 when $\sigma_{PDF,R}$ and $\overline{R}_{1\sigma}$ at cloud top are larger than that at cloud base. On this day, cloud top variability due to cloud top entrainment is typical, but the cloud is so underdeveloped (with a mean drizzle rate at cloud base of 0.098 mm/day) that drizzle does not develop through the depth of the cloud. This both

limits the width of PDF_R at larger sizes and inhibits strong drizzle patches from growing (Fig. 2.3b). Mid-cloud tends to exhibit narrower PDF_R distributions than either cloud top or cloud base since both entrainment and collisional growth are not as strong.

2.3.2.3 Variability within a single level

The horizontal variability of drizzle at a single level is expressed in each PDF_R. But relatively rare events, like the patches of heavy drizzle at cloud base on Day 14, are hard to see in the PDF_Rs in linear space (notice only a small bump to the right of the cloud base distribution in Fig. 2.3a, inset). Examining the time series of R is useful for investigating anomalies in the data not shown in the PDFs of R . For example, cloud base drizzle rates appear to have similar variability to mid-cloud and cloud top levels for approximately 350 seconds (Fig. 2.3a). At that point, the aircraft encounters an area of cloud containing patches of heavy drizzle for $\sim$300 seconds (or $\sim$15 km). The aircraft encounters three more areas with similar patchiness on this day, two more at cloud base (not shown) and one at mid-cloud (between 500 and 600 seconds). Two drizzle patches are also found at cloud base on Day 16 (not shown).

On Day 14, only 24% of the time spent at cloud base and only 3% of the time spent at the mid-cloud level was within drizzling patches. Similarly, on Day 15, only 18% of the time spent at cloud base was within a drizzling patch. Even within a patch of heavy drizzle, low drizzle rates are still the norm rather than the exception. For example, the 300 second patch of heavy drizzle in Fig. 2.3a only contains 22 seconds of high drizzle, corresponding to only 7% of the time within the drizzling patch. Because moments of high drizzle rate make up a relatively small percentage of the total time spent in cloud, the high drizzle are barely visible at high R in the PDF_R in Fig. 2.3a. From this, we conclude that heavy drizzle is not ubiquitous throughout MSc clouds but are rare events that appear to occur in clusters with a typical length scale of 1 to 10 km. The absence

or presence of these rare events appears to the primary distinguishing factor between weak and strong drizzling MSc.

2.3.2.4 Variability in drop population

We next examine the horizontal variability in the rain rate size distribution. As described in the Methods section, for each 1-s observation of R, we sum the contribution to drizzle rate from each bin size. This yields the total drizzle rate R over the drop distribution for each second. Level-averaged drizzle rates and drizzle rate distributions for the three cloud levels, CB, MC, and CT are computed and are shown in Table 2.3 and Fig. 2.4. Mode diameters and geometric standard deviations associated with the drizzle rate distributions are also listed in Table 2.3. We further characterize drizzle using the PDFs of 1-s the D_{50} and D_{90} values during each horizontal flight level illustrated in Figs. 2.5 and 2.6. Lastly, the geometric mean and standard deviation of each of these PDFs are computed with results listed in Table 2.4.

Because R depends on both drop concentration and drop size, we use these results to de-couple, as much as possible, these two effects and thereby study more carefully the drop size dependence of R. This is interesting in particular because it addresses the rates and variability of collisional growth. We note that N and D are somewhat dependent on each other as condensation, entrainment and collision-coalescence all can depend on both quantities, though only collisional growth can increase D beyond ~30 µm.

Unlike the drop size distributions, the drizzle rate distributions show large variations at all levels within the cloud between Days 14-17 (Fig. 2.4a-c). The larger moment of the drizzle rate distributions (approximately between the 4th and 5th moment) as compared to the number distribution (zeroeth moment) means that larger drop sizes are emphasized in the drizzle rate distribution. Physically, as drop sizes increase, the

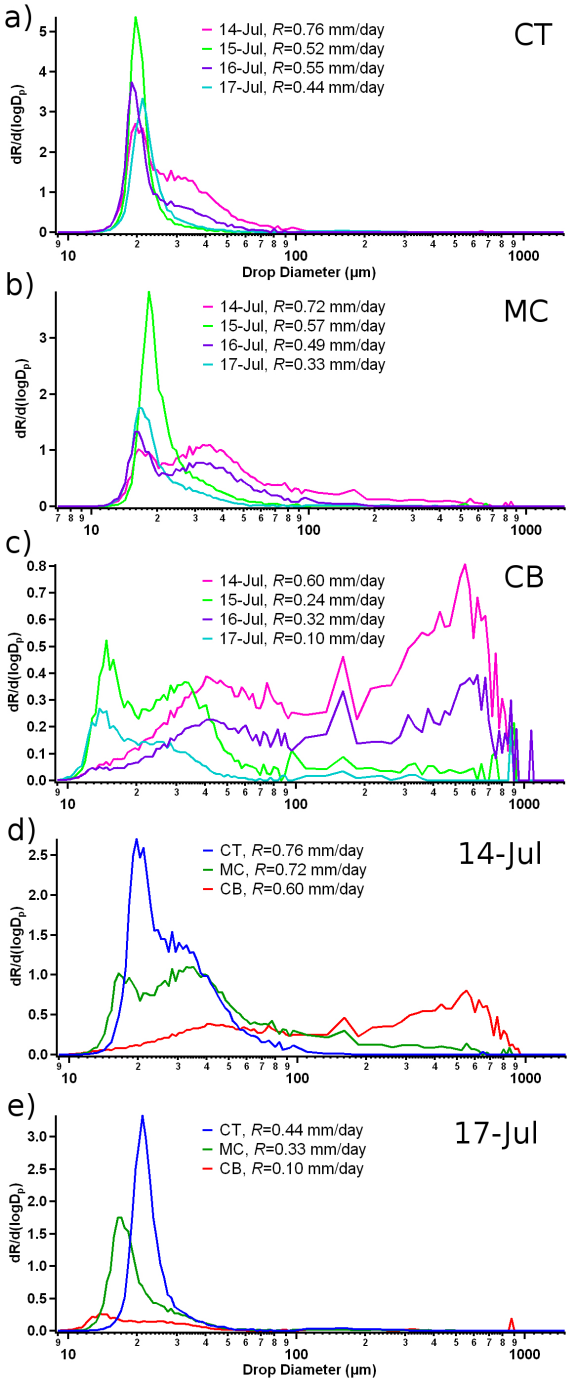

Figure 2.4: Drizzle rate distributions

Drizzle rate distributions for CT (a), MC (b), CB (c), Day 14 (d) and Day 17 (e). Corresponding level-averaged drizzle rates, R , are also presented on each plot.

	14-Jul	**15-Jul**	**16-Jul**	**17-Jul**
$D_{m,R}$ (µm)				
CT	19.7	19.7	19.0	21.1
MC	16.4, 32.6	18.3	16.4, 30.3	17.7
CB	550	14.8, 32.6	625	13.7, 25.3
$\sigma_{g,R}$				
CT	1.17	1.03	1.11	1.08
MC	1.71	1.13	1.28	1.14
CB	4.95	2.88	5.72	2.11

Table 2.3: Drizzle distribution statistics
Drizzle distribution statistics showing mode diameters, $D_{m,R}$, and geometric standard deviations, $\sigma_{g,R}$, for all days and levels.

increase in volume for each drop, along with the increase in terminal velocity, means that larger drops contribute much more to drizzle rate than smaller drops on a per-drop basis. Figure 2.4 and Table 2.3 will be examined in much greater detail in Sect. 2.3.3.2 when discussing the vertical structure of drizzle.

Now, we discuss the $\text{PDF}_{R,D50}$ and $\text{PDF}_{R,D90}$ distributions with respect to horizontal variability. Because the $\text{PDF}_{R,D50}$ and $\text{PDF}_{R,D90}$ distributions are products of the drizzle distributions, they too show large variation from day to day and level by level (Figs. 2.5 and 2.6).

Similar to Fig. 2.3 and Table 2.2, Figs 2.5 and 2.6 and Table 2.4 also reveal variability in the horizontal structure of drizzle. Starting at cloud top (Fig. 2.5a), the $\text{PDF}_{R,D50}$ distribution for Day 14, the heaviest drizzle day, stands out: the peak of the distribution is at a larger size, the mode height is shorter, and the distribution is wider than on any other day. Table 2.4 shows cloud top $D_{g,D50}$ on Day 14 is 25.9 µm compared to a relatively constant $D_{g,D50}$ on all of the other three days, which only range between 20.3 and 21.5 µm. These data suggest that the bulk drizzle population on Day 14 is much further developed and more variable at cloud top than any other day. One possible hypothesis, then, is that the strong drizzle and strong variability found throughout the

cloud on Day 14 is a result of a broad range of drizzle drop sizes at cloud top as evident by the wide distribution of the median drizzle drop sizes observed in Fig. 2.5a.

Figure 2.6 shows the peak of cloud top $\text{PDF}_{R,D90}$ distributions are very clearly separated for each day. This is very different from the case of the $\text{PDF}_{R,D50}$ distributions where only Day 14 stood apart. The $D_{g,D90}$ values in Table 2.4 show the peak values for each day are directly related to their drizzle rates; large $D_{g,D90}$ values correspond to large drizzle rates and vice versa. The width of $\text{PDF}_{R,D90}$ distributions also increases as the peak size increases, i.e. drizzle variability increases as drizzle becomes more developed.

	14-Jul	**15-Jul**	**16-Jul**	**17-Jul**		**14-Jul**	**15-Jul**	**16-Jul**	**17-Jul**
	$D_{g,D50}$ (µm)					$\sigma_{g,D50}$			
CT	25.9	20.3	21.1	21.5	CT	1.34	1.05	1.25	1.21
MC	32.5	21.1	27.1	18.7	MC	1.47	1.42	1.40	1.21
CB	48.2	27.0	45.4	19.1	CB	1.75	1.85	1.82	1.44
	$D_{g,D90}$ (µm)					$\sigma_{g,D90}$			
CT	43.6	24.3	33.7	27.4	CT	1.44	1.14	1.39	1.40
MC	59.7	33.0	52.0	30.1	MC	1.44	1.51	1.36	1.42
CB	1.75	1.70	1.90	1.66	CB	1.75	1.70	1.90	1.66

Table 2.4: Drizzle $\text{PDF}_{R,D50}$ and $\text{PDF}_{R,D90}$ distribution statistics
Drizzle $\text{PDF}_{R,D50}$ and $\text{PDF}_{R,D90}$ distribution statistics showing geometric means, $D_{g,D50}$ and $D_{g,D90}$, and geometric standard deviations, $\sigma_{g,D50}$ and $\sigma_{g,D90}$, for all days and levels.

We conclude that for very well-developed drizzle days, like Day 14, the variability in drizzle by any measure, whether that is in the PDF_R, $\text{PDF}_{R,D50}$, or the $\text{PDF}_{R,D90}$ distributions, at cloud top is large. But for Day 16, which does not show considerable strength or variability in R until cloud base, most cloud top metrics do not foretell the much more highly developed drizzle which exists farther down in the cloud. The exception is $\text{PDF}_{R,D90}$, which does appear able to indicate how drizzle will develop throughout the cloud. This suggests that at cloud top, even the presence of a small

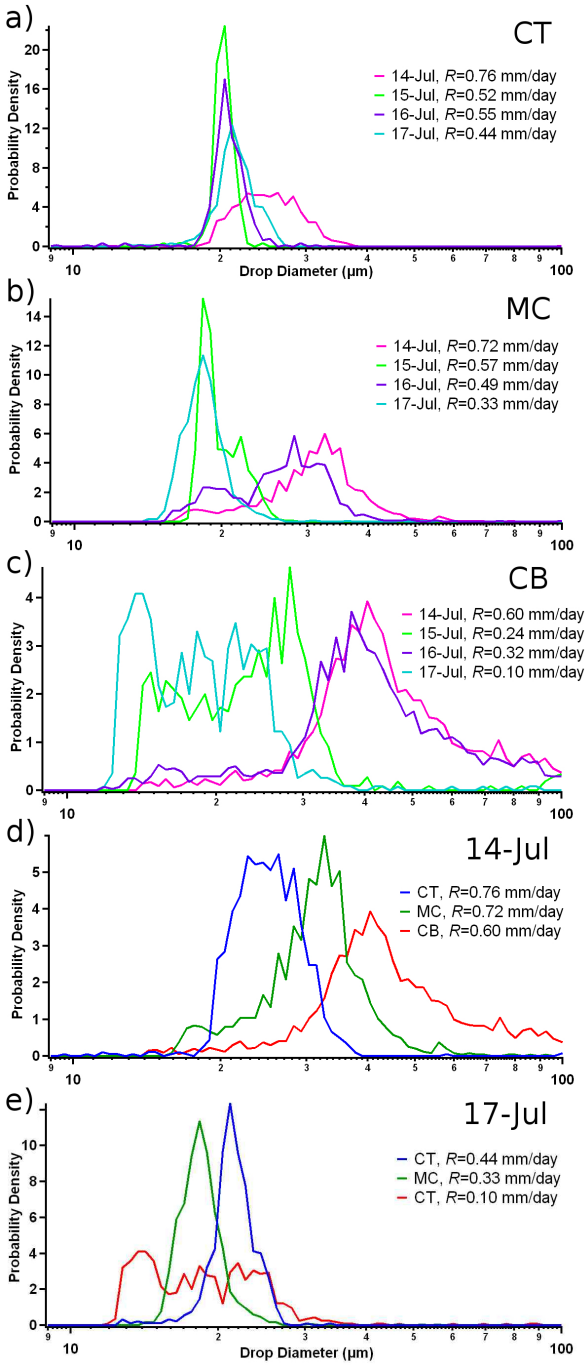

Figure 2.5: $\mathrm{PDF}_{R,D50}$ distributions

$\mathrm{PDF}_{R,D50}$ distributions for CT (a), MC (b), CB (c), Day 14 (d) and Day 17 (e). Corresponding level-averaged drizzle rates, R , are also presented on each plot.

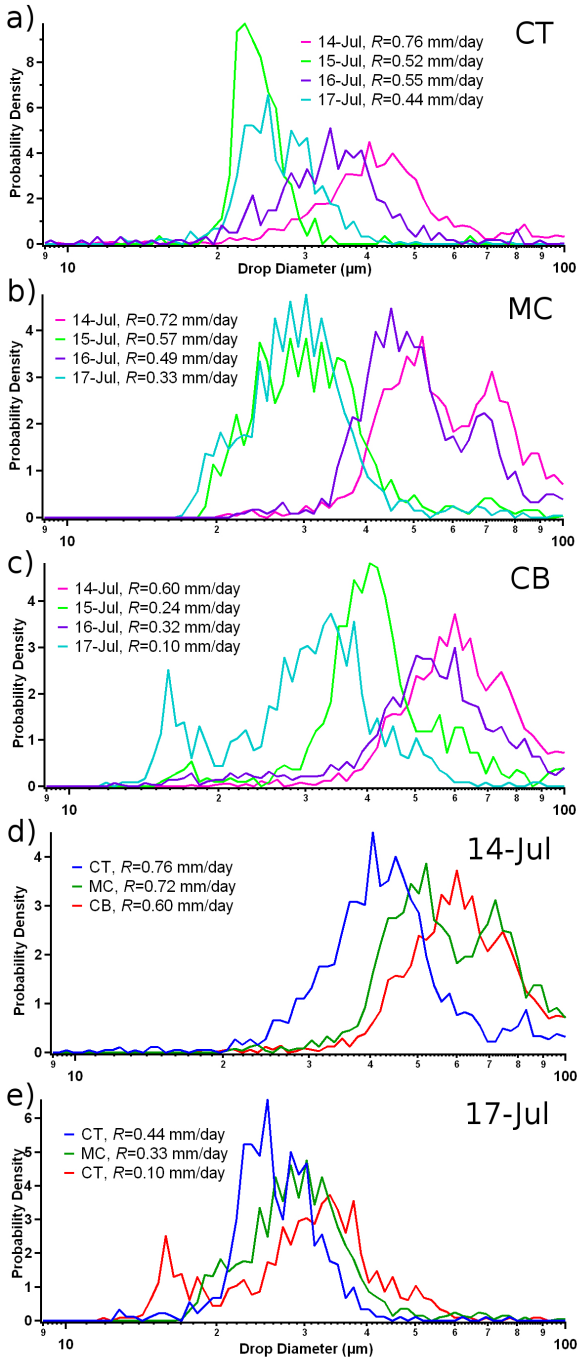

Figure 2.6: $\mathrm{PDF}_{R,D90}$ distributions

$\mathrm{PDF}_{R,D90}$ distributions for CT (a), MC (b), CB (c), Day 14 (d) and Day 17 (e). Corresponding level-averaged drizzle rates, R , are also presented on each plot.

fraction of larger, collisionally-formed drops – so few that they do not change mean cloud top properties – can greatly alter the drizzling properties of the Sc layer. This is consistent with the notion that strong drizzle is highly patchy, as discussed above, and highlights the importance of having accurate DSD for possibly diagnosing the strength of drizzle within a cloud from cloud top distributions alone.

At the mid-cloud and cloud base levels, the $\mathrm{PDF}_{R,D50}$ and $\mathrm{PDF}_{R,D90}$ distributions separate between Days 14/16, the strong drizzle days, and Day 15/17, the weaker drizzling days. This separation is evident in the peak of the distributions, corresponding to a separation in the development of drizzle drops, and in the widths of the distributions, corresponding to a divergence in the horizontal variability found between the two sets of days (Fig. 2.5b-c). Table 2.4 shows the divergence of the mid-cloud $D_{g,D50}$ values on Days 14/16 (32.5/27.1 µm) and Days 15/17 (21.1/18.65 µm), and cloud base $D_{g,D50}$ values between Days 14/16 (48.2/45.4 µm) and Days 15/17 (27.0/19.1 µm). Similarly, the mid-cloud $D_{g,D90}$ values also clearly diverge between Days 14/16 (59.7/52.0 µm) and Days 15/17 (33.0/30.1 µm), and cloud base $D_{g,D90}$ values between Days 14/16 (75.0/71.1 µm) and Days 15/17 (47.6/31.7 µm). With distribution peaks at larger sizes in both $\mathrm{PDF}_{R,D50}$ and $\mathrm{PDF}_{R,D90}$ distributions, the drizzle drop population is significantly more developed on Days 14/16, the days exhibiting much stronger drizzle rates, than on Days 15/17. Broader $\mathrm{PDF}_{R,D50}$ distributions on Days 14/16 than on Days 15/17 (Fig. 2.5b-c) suggest more variability in the mean drizzle size and therefore more variability in drop population, consistent with our findings that drizzle is highly spatially variable especially during heavily drizzling days like Days 14/16.

The horizontal variability of drizzle has revealed to be a diverse and complex property of the 4 stratocumulus layers studied. It has been shown that while DSD do not exhibit differences amongst the daily drop population except at cloud base, drizzle PDFs and time series data reveal large variations in horizontal drizzle at mid-cloud and cloud base levels and can further distinguish between light and heavy drizzle cases: heavy drizzling

days being more horizontally variable and light drizzling days being less. Furthermore, an investigation of the drop population using $\mathrm{PDF}_{R,D50}$ and $\mathrm{PDF}_{R,D90}$ distributions lead to even more explicit differences between heavy and light drizzle days: heavy drizzling days show more well-developed drops and higher variability than less drizzling days. In particular, unlike all the other methods of investigating horizontal drizzle rate variability, $\mathrm{PDF}_{R,D90}$ show large difference in the distributions at all levels, including at cloud top.

Investigating the horizontal variability of drizzle also lead to questions regarding the vertical structure of drizzle. For example, Day 14 and 16 exhibited small amounts of variability at cloud top which seemed to become magnified through the cloud layers. Also, while the $\mathrm{PDF}_{R,D90}$ distributions at cloud top revealed information about the drizzliness of the cloud below, the mean drizzle size was not indicative of drizzle (amount or variability) in the rest of the cloud. This suggests that the vertical development of drizzle is primarily driven by the largest drops (shown in the $\mathrm{PDF}_{R,D90}$) rather than the average drops. These findings and others will be investigated further in the following section focusing on the vertical structure of the drizzle for MASE Days 14-17.

2.3.3 Vertical Structure of Drizzle

Aside from investigating the horizontal structure of drizzle, it is also important to study the organization of drizzle in the vertical direction. Drop growth and drizzle formation are thought to be vertical processes and therefore in order to understand how the variations of drizzle structure developed from day to day (e.g. heavy versus light drizzle days), it is important to study the evolution of drizzle through the depth of the cloud. Our analysis of the vertical structure of drizzle begins by developing a contextual basis for studying the drizzle rate distributions; we first take a thorough look at how the average total drizzle rates develop within the cloud. We then move on to explore the vertical variability of the R distributions within the 4 study days, and lastly, we discuss

the growth of the drizzle drops from cloud top to cloud base.

2.3.3.1 Total drizzle rates through the cloud

Average total drizzle rates, $\overline{R}$, for each day and level are plotted in Fig. 2.7a. Most noticeable is that $\overline{R}$ increases from cloud base to cloud top. A review of the drizzle rate distributions (Fig. 2.4) indicates that drizzle contribution from cloud droplets <40 µm is a significant source of the sedimenting water flux at all levels in the cloud. However, the smallest drop size that is considered drizzle varies substantially, with typical values ∼40 µm diameter [*Wood*, 2005; *Bretherton et al.*, 2007; *Lu et al.*, 2007]. Small drops are often dismissed in drizzle calculations because drizzle rate (scaling with D^4 orD^5) is very sensitive to the presence of a few larger drops since they are volumetrically significant and have large fall speeds. However, *Nicholls* [1984] reports observations that suggest that the contribution of drops smaller than 50 µm to the drizzle rate can be very substantial, particularly at cloud top, although the resolution of the instrumentation allowed for only a coarse analysis. The drizzle rate calculations presented in this study, which come from instrumentation much more suitable for studying this size range, support these findings. R distributions on Days 15/17 indicate that almost all of the cloud top and mid-cloud drizzle is comprised of drops <40 µm (Fig. 2.4a-b). Even at cloud base, where drop sizes are largest and contribute most to the total drizzle rate, $\mathrm{PDF}_{R,D50}$ distributions for Days 15/17 lie entirely to the left of 40 µm, indicating that over half of the drizzle at cloud base is made up of drops <40 µm (Fig. 2.5c). For Days 14/16, the $\mathrm{PDF}_{R,D50}$ distributions at cloud top, and nearly all at mid-cloud, lie to the left of 40 µm, indicating that even on the heaviest drizzling days, a substantial fraction of the drizzle in the top half of the cloud is made up of drops <40 µm (Fig. 2.5a-b).

Average total drizzle rates which do not include drops <40 µm, $\overline{R}_{40}$, for each day and level are plotted in Fig. 2.7b. $\overline{R}_{40}$ increases from cloud top to cloud base, a paradigmatic

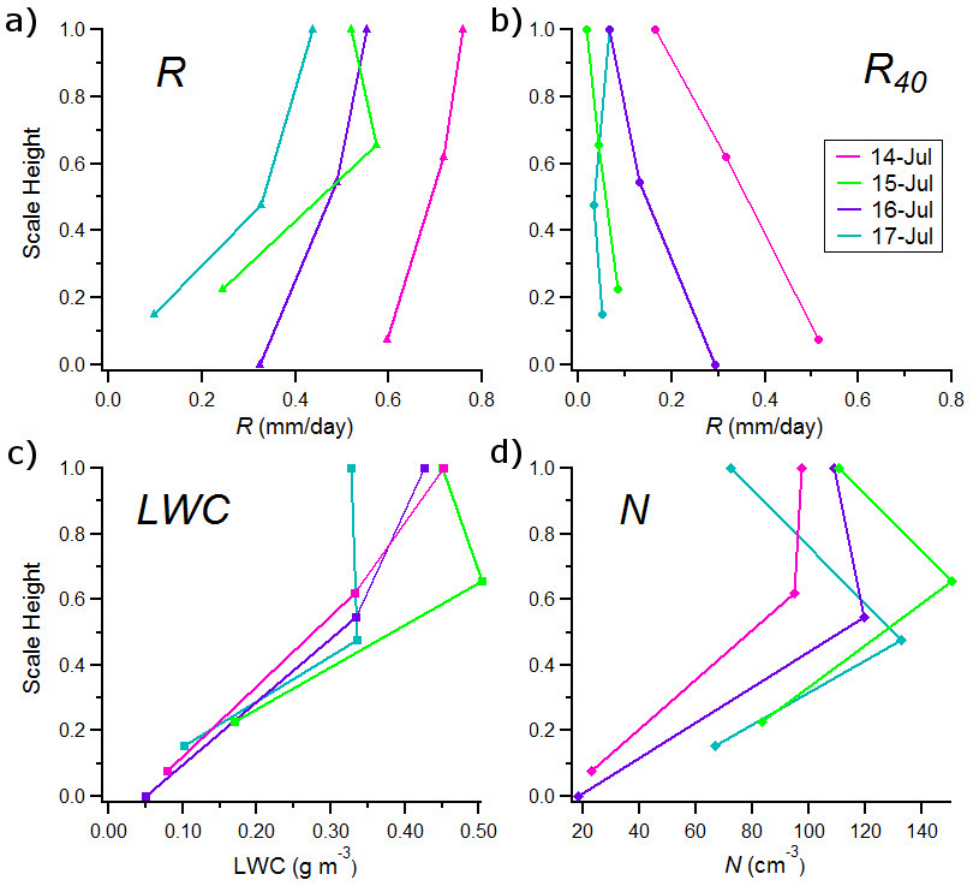

Figure 2.7: Level-averaged cloud properties
Level-averaged R, R_{40}, LWC and N for all days plotted with scale height.

view of drizzle rate. Figure 2.7a and 2.7b show that at cloud top and mid-cloud levels are more significant sources of drizzle when considering the contribution of all drops to the total drizzle rate. At cloud top, $\overline{R}$ drops significantly (79%, 97%, 88%, and 84%, 14th-17th respectively) from $\overline{R}$ to $\overline{R}_{40}$ (Fig. 2.7a,b), confirming that cloud top drizzle is comprised mostly of small droplets. Differences in $\overline{R}$ and $\overline{R}_{40}$ are greatest at cloud top and generally decrease moving down in the cloud indicating the contribution of drops >40 µm to the total drizzle rate increases towards cloud base. This highlights the fact that cloud droplets < 40 µm are a significant source of drizzle in many parts of the cloud, not exclusively at cloud top.

We will next explore how the contribution from different drop sizes to R changes throughout the depth of the cloud. Examining the difference in drizzle distribution within the cloud will help us understand how the drizzle structures varies from day to day. While we have shown that the smaller drops contribute most to cloud top and mid-cloud drizzle rates, larger drop sizes are critical to the development of heavy drizzle, as discussed above (Sect. 2.3.2.2). The distinction between heavy versus light drizzling days is important because high or low drizzle rates strongly determine the future state of the cloud. High drizzle rate may lead to a decoupling of the cloud layer, removal of water (energy) from the STBL system, and possibly pockets of open cells (POCs) which have been found to be the embryos to mesoscale cloud breakup [*Stevens et al.*, 1998, 2003, 2005].

2.3.3.2 Vertical variability through the cloud

Our analysis of the horizontal distribution of drizzle in Sections 2.3.2 and 2.3.2.2, gave us a brief look into drizzle formation in the vertical, which we explore now in greater depth. Unlike the number drop size distributions, which only showed variation between Days 14/16 and Days 15/17 at cloud base, but similar to the $\mathrm{PDF}_{R,D50}$ and $\mathrm{PDF}_{R,D90}$ distributions, large variations in the drizzle distributions can be seen between Days 14/16 and Days 15/17 through the entire depth of the cloud (Fig. 2.4a-c). While all of the days have similar mode diameters at cloud top ($D_{m,R}$, between 19.0 and 21.1 µm), Days 14 and 16 have a markedly different distribution shapes than Days 15 and 17, especially at larger drop sizes (Table 2.3 and Fig. 2.4a). On Days 15 and 17 the distributions are fairly symmetric (similar to their corresponding number distributions) whereas Days 14 and 16 contain a distinct shoulder between 25 and 100 µm.

Mid-cloud drizzle distributions (Fig. 2.4b) are similar to their corresponding cloud top distributions, but with greater collisional growth on the higher drizzle days. All

mode heights are suppressed (note the change in y-axis), and the shoulders on Days 14/16 developed into a second mode of well-developed drizzle drops. Like at cloud top, the first mode of the drizzle distributions are similar, $D_{m,R}$ only ranging between 16.4 and 18.3 µm, and the second mode on Days 14 and 16 only range between 30.3 and 32.6 µm. Day 14 has a significantly long tail showing consistent contribution to R from D as large as 600 µm. The widths of the drizzle rate distributions, as reflected by the geometric standard deviation of the drizzle distributions, $\sigma_{g,R}$, in Table 2.3, correspond to differences in $\overline{R}$. In other words, large $\sigma_{g,R}$ correspond to large R. This is dissimilar to $\text{PDF}_{R,D50}$ and $\text{PDF}_{R,D90}$ distributions where large $D_{g,D90}$ values corresponded to large drizzle rates.

The slight separation of $\sigma_{g,DSD}$ between Days 14/16 and Days 15/17 (on Table 2.1 and discussed in Sect. 2.3.1) is now pronounced in Fig. 2.4a and2.4b. The slightly larger $\sigma_{g,DSD}$ on Days 14/16 are associated with the tails to larger sizes at cloud top and the second mode in the R distributions at mid-cloud. The larger moment of the drizzle rate distributions as compared to the number distribution means that larger drop sizes, which contributed to the slightly larger $\sigma_{g,DSD}$, are emphasized in the drizzle rate distribution.

Cloud base drizzle distributions (Fig. 2.4c) show even larger mode height suppression (again, note the change in the y-axis) and broadening. Days 15/17 finally develop a second mode at larger sizes, while on Days 14/16, the mode at smaller drop sizes, pronounced at cloud top and mid-cloud, disappears. A new mode, centered at drop sizes significantly greater than any other mode (550 µm and 625 µm) and with mode heights larger than either mode on Days 15/17, appears. Also unique about the new mode on Days 14/16 is that their heights are both larger than the heights of the first mode at smaller sizes. We conclude that at cloud base, larger drop sizes contribute more to R than smaller drop sizes ($D > 100$ µm) on Days 14/16, consistent with R distributions from a well-developed, drizzling cloud.

The second mode on Days 14/16 extends far past the bounds of the PDI measurements (98 µm) and into the range measured by the CIP. The CIP samples well until ∼600 µm, where the effect of poor counting statistics become noticeable in the drizzle distributions. A spike in a single CIP diameter bin, centered at 161 µm, is also visible. The implementation of the concentration correction factor, as described in Section 2.3.3.2, lowered the concentration at all CIP diameters up to this bin; the correction disappears at this bin, leading to a jump in the drizzle distribution. The distribution does appear to recover to reasonable values starting with the next bin, so this artifact is temporary and does not significantly affect the data.

Figure 2.2d shows the number distributions for each flight level on Day 15 (discussed in Sect. 2.3.1), we note the shift in the drop size distribution from cloud base to cloud top is clearly dominated by condensational growth, with mean drop size increasing with height. All other days (14, 16, and 17, not shown) show very similar distributions. Drizzle rate distributions from Day 17 (Fig. 2.4e), the least drizzly of all 4 days, also shows that the vertical structure of drizzle is dominated by condensation on this day. Figure 2.5e shows that there is some collectional growth between mid-cloud and cloud base based on some larger D_{50} values, but this does not dominate the vertical structure of drizzle on this day. Day 15 shows a similar pattern to Day 17 and therefore is not shown.

In contrast to the low-drizzle cases, drizzle rate distributions from Day 14, the heaviest drizzling day, show increasing contribution to the drizzle rate by larger drops from cloud top to cloud base, consistent with growth dominated by collision-coalescence (Fig. 2.4d). The mode dominated by condensational growth is still noticeable from mid-cloud to cloud top (growing from 16.4 to 19.7 µm) but is absent from mid-cloud to cloud base. The elimination of a condensation mode near cloud base at sizes smaller than 16 µm can be explained by collisional scavenging which removes many of these drops. Day 16 shows a similar pattern to Day 14 and therefore is not shown.

It is apparent that two distinct vertical patterns in drizzle exist: one which is dominated by condensational growth, seen on all days, and the other by collision-coalescence, which is only apparent only on the high drizzle days (Days 14/16). It is not possible to determine which day consists of high drizzle versus low drizzle by simply comparing the mode of the number distributions at cloud top or mid-cloud (Fig. 2.2a-b). This emphasizes that drizzle is a phenomenon associated with small changes in the tail of the number distribution at large drop sizes rather than the mode. Conversely, the drizzle distributions show clear differences among the days because they represent a higher-moment of the distribution. The drizzle distributions at cloud top, especially the PDF_{D90}, reveal of the initial stages of drizzle production; the tail end of the distributions, comprised of a very few, lucky drops, evolve to contribute to the drizzling patches seen at cloud base. The vertical growth of these drops is discussed next.

2.3.3.3 Vertical growth of drizzle

This study emphasizes the importance of accurate cloud top measurements for characterizing the drizzling state of a cloud. Cloud top drop measurements are important because they are the only data which contain information from a single moment in the lifetime of the cloud drop distribution. All other measurements—in the case of our study, those that are retrieved at mid-cloud or at cloud base—are mixtures of cloud droplets from two stages of their growth. One, which contains drops on their way up through the cloud, as they grow by condensation, and the other, which contains drops falling through the cloud. Cloud base, for example, is comprised of drops at the beginning of their life cycle, which we have shown account for the majority of the cloud data, and at the end of their life cycle. For Days 14/16, drops at the end of their life cycle only account for a small concentration of cloud drop but a large portion of the drizzle flux. Cloud top measurements are therefore restrained to the middle period of a cloud drop's

growth.

Cloud top drop measurements are also important because this is where the first few drops large enough to form heavy drizzle are found. Several mechanisms have been proposed for the formation of embryonic drizzle drops. One of the initial hypothesis was that giant CCN, which can act as large collection nuclei, were responsible for the formation of the largest drop sizes [*Johnson*, 1982]. More recently, an increase in the speed and accuracy of *in situ* probes, alongside the development of cloud models and laboratory tools, prompted a surge of studies investigating the role of mixing on embryonic drop development. These studies began by investigating the simplest mixing types, for example, homogenous and inhomogeneous mixing [*Mason and Jonas*, 1974; *Baker et al.*, 1980] but soon, more complex mixing models were hypothesized. These include, but are not limited to: entity type entrainment mixing, turbulent internal mixing, circulation mixing, and stochastic condensation [*Telford and Chai*, 1980; *Cooper*, 1989; *Hudson and Svensson*, 1995; *McGraw and Liu*, 2006]. While the specifics of each type are not important here, they all depend on a combination of processes which affect drop trajectory through its lifetime. One of the most important factors which affect drop trajectory is turbulence. While almost all mixing models account for it, others treat it as the primary forcing (eg. turbulent internal mixing and stochastic condensation). The final hypothesis for the formation of embryonic drizzle drops is turbulence itself (regardless of mixing process).

Let us first analytically estimate the collisional growth for sedimenting drops in quiescent air. For a cloud thickness of 300 m, the growth between cloud top and cloud base is $\Delta D \sim$20 µm assuming a cloud-top LWC of 0.3 g kg^{-1} and that LWC increases linearly with height. The more general formula is:

$$\Delta D \sim \frac{LH}{4\rho_l} \tag{2.3.1}$$

where L is the maximum (assumed at cloud top) LWC, H is cloud thickness, and ρ_l is density of water. Note that liquid water path is, under these assumptions, given by LWP= $\frac{1}{2}LH$. In order for a 20 µm drop at cloud top to grow to, say, 400 µm at cloud base (drops as large as 800 µm contribute to CB R on Day 14) requires ∼10 entire circuits of the cloud (each circuit being two passes through the cloud, one downwards and one upwards). Alternately, if the drop simply sediments monotonically downwards then the path length must be increased by a factor of ~ 20. Another option is that the effective collision cross-sectional area increases by a factor ∼20 (collisional radius would then increase by a factor of ∼4 to 5). One of these, or a combination thereof, is needed to explain the observed R distributions. Note that the above formula assumes that the collected drops are points and have no diameter. This equation then underestimates the growth of D since it does not account for the finite size of the collected cloud drops. The formula is not very accurate when the collector drop is small (same size as the cloud drops) but becomes more accurate as the collector drops grows larger. We estimate this underestimates growth by one or two circuits, which is the number of circuits it takes to yield drops such that $D_{collector} >> D_{cloud}$. *Jonas* [1996] finds values similar in magnitude, stating, in still air, a drop with an initial radius 20 µm at cloud top can only grow by ∼1 to 2 µm as it falls to the cloud base of a 100 m deep layer, or to ∼30 µm through a 500 m deep layer (assuming realistic LWC and a collection efficiency of one).

It is clear from Figs. 2.4, 2.5, and 2.6 that drizzle drops develop much more than this. The tail of the cloud top R distributions, the contribution of R from the most developed drizzle drops, on Day 14 ends at 100 µm. By the time the most developed cloud drops have reached cloud base, 195 m later, some have grown to as large as ∼1000 µm (Fig. 2.4). Even the less developed cloud days show accelerated drizzle drop growth. $\mathrm{PDF}_{R,D90}$ distributions at cloud top for Day 15, a ∼230 m deep cloud, show contributions from drops up to only ∼30 µm while at cloud base, contributions continue from drops up to ∼85 µm (Fig. 2.6). It is also clear from Figs. 2.4, 2.5, and 2.6 that there is no

evidence of drop recycling. Because the drop size differences are relatively small for each pass through the cloud, cloud top and cloud base would have to look very similar for recycling to be a plausible mechanism. At very best, several of the large drops at cloud top (Fig. 2.6) could be individually recycled drops. What processes would account for only a tiny fraction of the drop population to be recycled? Is this sufficient enough to produce patchy, heavy drizzle like that seen on Days 14/16?

It is clear the calculations are incomplete because as they include the assumption that the drops are falling through still air. It is because of this that scientists, beginning with *Mason* [1952], have modeled the trajectories of cloud drops affected by turbulent motion within the cloud. Model results show turbulent motions increase the dwell-time of a drop by several times its gravitational settling time allowing for repeat collision-coalescence cycles [*Wang et al.*, 2005; *Pinsky et al.*, 2006; *Franklin et al.*, 2007]. While scientist have been including the effects of turbulence on drop growth for decades, beginning with *Bowen* [1950], observational evidence is still lacking. And although the amount of turbulent motion in MASE clouds could not be calculated because the turbulence gust probe was not functioning properly, a mechanism for collisional growth acceleration clearly exists.

2.4 Conclusions

In this study, we have analyzed observations of DSD measured by the F-PDI and CIP in the summertime MSc cloud deck off the coast of central California during the MASE project in July 2005. Using the DSD from flight level legs (CT, MC, and CB) we computed a number of statistics relating to the number size distribution and the drizzle size distribution in order to understand the horizontal and vertical structure and variability of drizzle. We focus in particular on statistics relating to the drizzle rate R. Our main

findings include:

- During the four study days, we find two microphysical regimes, a high drizzle regime on Days 14/16 and a low drizzle regime on Days 15/17. These two regimes, however, are not apparent when looking at the number size distribution (Fig. 2.2), but are only brought out when statistics that emphasize higher moments (and hence larger drops) are examined, such as the drizzle rate.

- High drizzle days exhibit higher R at all levels compared to low drizzle days (Figs. 2.3, 2.5 and 2.6) at nearly all times. Thus, high drizzle days are not merely low drizzle days with a few patches of high R. Instead, there is a systematic difference in the mean properties of these clouds at all altitudes that causes their drizzle properties to be so different. This is particularly noticeable when the PDFs of the median (D_{50}) and 90th percentile (D_{90}) diameters of the drizzle rate distribution are compiled at different altitudes within the cloud (Figs. 2.5 and 2.6).

- High drizzle days also exhibit much more variability in R than low drizzle days (Table 2.2), in particular at large R values. Thus, clouds with large $\overline{R}$ are associated with patches of heavy drizzle and clouds with low $\overline{R}$ are associated with more uniform, light-to-no drizzle. Heavy drizzle is appears to occur in clusters with a typical length scale of 1 to 10 km.

- The presence of a small fraction of large, collisionally-formed drops at cloud top, most evident by examining $\mathrm{PDF}_{R,D90}$, appears to be a very strong indicator of how drizzle will develop through the cloud. Since we are looking only at four days, more data would be needed to determine whether this is a generalizable result.

- Drops up to 1 mm in diameter contribute significantly to R at cloud base on high drizzle days (Fig. 2.4). On the other hand, there is almost no contribution

to R from drops $D > 100$ µm at cloud top. This growth can not be explained by simple gravitational sedimentation of the largest CT drops through the cloud, as this is easily calculated to yield a diameter increase of 10 to 30 µm at most. Thus, the collisional growth of drops from CT to CB can not be explained only by cycling of air parcels and/or large drops within the cloud, as this would require the distributions to look almost the same, differing merely by 10 to 30 µm. Instead, the observed vertical structure requires either (i) the effective path length of the largest sedimenting drops must be increased by a factor of ten to a hundred, or (ii) the effective collection cross-section must increase by this same factor, or (iii) a combination of (i) and (ii).

- We hypothesize that the most obvious mechanism for such an effect is the enhancement in collision rates from turbulence, even at the low energy dissipation rates characteristic of Sc.

More generally, our results emphasize the importance of accurately quantifying drizzle in MSc, a statement that is supported by previous work [*Nicholls*, 1984; *Austin et al.*, 1995; *Bretherton et al.*, 1995; *Duynkerke et al.*, 1995; *Frisch et al.*, 1995; *Boers et al.*, 1996; *Vali et al.*, 1998; *vanZanten et al.*, 2005]. Drizzle properties are observed to span a wide range, even over short time and spatial scales, implying that the impact of drizzle on the MBL can vary significantly. We suggest that further investigations of the effect of turbulence on collision-coalescence in stratocumulus are needed to improve quantitative understanding of drizzle in this regime.

Chapter 3

Observations and implications of sub-cloud drizzle evaporation in marine stratocumulus

Evaporation of drizzle below the cloud layer is very important to the water and energy budgets of the stratocumulus-topped marine boundary layer (STBL). Sub-cloud evaporative cooling can lead to large-scale changes in boundary layer turbulence and buoyancy production. Condensational warming in the cloud layer and evaporative cooling below can change the overall stability of the marine boundary layer (MBL), promoting the decoupling of the mixed layer and eventually leading to the breakup of the cloud. Although the effects of evaporation on the system are widely acknowledged, quantifying its effects using observed drop measurements has been limited. Here, we utilize *in situ* aircraft observations of the cloud drop size distribution (DSD) of near-coastal marine stratocumulus clouds to thereby derive drizzle and sub-cloud evaporation rates. Measurements were obtained using the Artium Flight Phase Doppler Interferometer (F-PDI) during the MArine Stratus Experiment (MASE) in July 2005 in the northeastern subtropical

Pacific. The observations indicate a large range of BL cooling exists between our study days. Sub-cloud profiles of evaporative cooling show characteristic distributions, with variability in both peak magnitude and width. We show this variability corresponds to variations in the shape of the drizzle rate distributions. Variability is also found to exist in the horizontal, with implications for MBL turbulent kinetic energy. We utilize the concept of available potential energy (APE) to estimate the energy flux associated with evaporation and show it makes up a large portion of the radiative flux driving the MBL (1-50%). Although a number of assumptions were made in this study, given the broad range of data presented, our results demonstrate that evaporation plays a large role in MBL dynamics and cloud lifetime, and thus the global climate system.

3.1 Introduction

Clouds serve two major roles in the constant transport of energy on Earth. First, clouds affect the climate of the Earth by interacting with solar and terrestrial radiation. Second, clouds act as an intermediary step in the water cycle, storing water between the time it evaporates from the surface and before it falls as precipitation. This research focuses on the microphysical properties of stratocumulus clouds and their impact on the energy budgets (both radiation and water) of the stratocumulus-topped marine boundary layer (STBL). The most widespread and ubiquitous clouds, having a strong negative effect on the Earth's radiation budget, are the low lying marine stratocumulus (MSc) clouds which cover the world's eastern subtropical oceans [*Eastman et al.*, 2011]. While the sensitivity of the Earth's energy budget to MSc is large, their quantitative impact on the STBL remain unknown [*Bretherton et al.*, 2004].

MSc are a major source of uncertainty in climate estimates because of the many questions that remain regarding processes that lead to their formation, evolution, and dissipation and processes which affect their radiative properties [*Bony and Dufresne*,

2005; *Bony et al.*, 2006; *Cronin et al.*, 2006; *Wyant et al.*, 2006; *Delecluse et al.*, 1998]. One of these processes is drizzle, the sedimentation of drops through the cloud. Recently, as cloud probing instruments, such as radar, satellites and aircraft based equipment, have improved, the importance of drizzle on STBL dynamics has become increasingly more evident [*Nicholls*, 1984; *Frisch et al.*, 1995; *Bretherton et al.*, 1995; *Austin et al.*, 1995; *Boers et al.*, 1996; *Vali et al.*, 1998; *vanZanten et al.*, 2005; *Duynkerke et al.*, 1995]. While drizzle is responsible for the movement of water through the boundary layer, it also contributes to the redistribution of energy through the entire STBL. One prominent example is that once drops leave cloud base, they are subject to subsaturated relative humidities and begin to evaporate, adding moisture to and removing sensible heat from the sub-cloud layer.

The evaporation of drizzle within the sub-cloud layer is an important process within the marine boundary layer (MBL) and, via feedbacks, can impact the cloud layer itself. For example, sub-cloud evaporative cooling can lead to large-scale changes in boundary layer turbulence and buoyancy production [*Feingold et al.*, 1996]. *Wang and Feingold* [2009] identify this mechanism as the crucial link between drizzle and the formation and maintenance of pockets of open cells (POCs). Condensational warming in the cloud layer and evaporative cooling below can change the overall stability of the MBL [*Brost et al.*, 1982; *Wang and Wang*, 1994]. This could promote the decoupling of the mixed layer, cut-off surface fluxes into the base of the MSc, and eventually lead to the breakup of the cloud [*Nicholls*, 1984; *Paluch and Lenschow*, 1991; *Wang*, 1993; *Wang and Wang*, 1994]. Such decoupling is thought to play a role in the stratocumulus to cumulus transition [*Paluch and Lenschow*, 1991; *Feingold et al.*, 1996; *Stevens et al.*, 1998].

Understanding how the evaporation of drizzle quantitatively affects the MBL system is important for predicting the subsequent evolution and lifetime of the cloud. For example, a surface drizzle flux of 1 mm/day warms the boundary layer by approximately 30 W/m^2. Drizzle is clearly an important component of the MBL energy budget, although

questions remain regarding how this flux directly and indirectly affects the BL dynamics and how it compares to other competing processes which also influence cloud albedo and lifetime. It has been suggested that sufficient drizzle alone may be capable of offsetting the other radiative forces of the BL to the point of cloud breakup [*Paluch and Lenschow*, 1991].

This study uses observed drizzle distributions to derive sub-cloud evaporation rates, a study that has not yet been attempted observationally. Sub-cloud evaporation rates are then used to study the effects of evaporation on MBL dynamics in order to understand the potential consequences for MSc evolution. Section 3.2 describes the general methodology used in this study. Section 3.3.1 presents calculations of average evaporative drizzle flux through the depth of the sub-cloud layer and its implications for BL dynamics. We explore the relationship between drizzle rate and sub-cloud cooling in Sect. 3.3.2. A discussion of the spatial variability of sub-cloud evaporation is presented in Sect. 3.3.3, and in Sect. 3.3.4, we quantify the effect of evaporation on BL energetics by calculating the available potential energy associated with sub-cloud cooling.

3.2 Methods

The research presented here utilizes instruments onboard the Center for Interdisciplinary Remotely-Piloted Aircraft Studies (CIRPAS) Twin Otter during the MArine Stratus/Stratocumulus Experiment (MASE) in July 2005. Specifically, cloud drop size distribution (DSD) data are used for computing drizzle rates and evaporation rates necessary for this study. To capture the whole range of drop sizes, drop size measurements from the Artium Flight Phase Doppler Interferometer (F-PDI) ($D < 98$ µm) were merged with those from the Cloud Imaging Probe (CIP) ($98 < D < 1562$ µm). An introduction to the F-PDI can be found in Chapter 1 and in detail in *Chuang et al.* [2008]. A general overview of the entire MASE project can be found in *Lu et al.* [2007], while its specifics,

as they relate to this work, can also be found in Chapter 1. Many of the findings and discussions presented in this study were built directly upon drizzle results found in Chapter 2 and therefore will be referenced when appropriate.

3.2.1 Evaporation Calculations

The phase change of water primarily occurs in the stratocumulus layer in the form of condensation and in the sub-cloud layer in the form of evaporation. In order to predict the dynamic response of the BL to these changes, it is important to quantify the amount of heat and moisture lost or gained via these processes. This research focuses on the redistribution of heat/moisture caused only by evaporation. We assume a stratocumulus layer exists in a well-mixed BL, meaning that the sub-cloud profile of potential temperature and water vapor mixing ratio are constant, both horizontally and vertically. Cloud drops are subject to gravitational settling, moving them through the cloud towards cloud base. Once a drizzle drops falls into the sub-saturated layer below cloud, evaporation begins. At this point, there are two possible fates for the water. First, the precipitation is completely evaporated and moisture is redistributed into the sub-cloud layer. Second, sub-saturated conditions are insufficient to evaporate all of the drops completely, precipitation reaches the surface, and water is removed from the boundary layer.

The fate of sub-cloud drizzle depends on environmental conditions and the DSD. The rate of growth or evaporation of a single falling drop with diameter D is given by:

$$\dot{m}(D) = \frac{dm}{dt} = 2\pi D \alpha_v \overline{f}_v \left(\rho_{v,\infty} - \rho_{v,D}\right) \tag{3.2.1}$$

where m is the drop mass, α_v is the diffusivity of water in air, $\overline{f}_v$ is the mean ventilation coefficient, $\rho_{v,D}$ is the density of vapor just above the surface of the drop, and $\rho_{v,\infty}$ is the density of vapor in the surrounding air. $\overline{f}_v$ describes the additional water

mass flux (relative to pure diffusion) to or from the drop due to its relative velocity with the air (i.e. due to sedimentation; *Pruppacher and Klett*, 1997, p. 537). *Pruppacher and Rasmussen* [1979] and *Pruppacher and Beard* [1970] both use experimental data to derive the empirical relationship:

$$\overline{f}_v = 1.00 + 0.108 \left(N_{Sc,v}^{\frac{1}{3}} N_{Re}^{\frac{1}{2}} \right)^2 \tag{3.2.2}$$

where N_{Sc} is the Schmidt number and N_{Re} is the Reynolds number. To calculate $\overline{f}_v$, we assume that a drop falling through the sub-cloud layer has a velocity relative to the air equal to its terminal velocity, w_T [*Pruppacher and Klett*, 1997]. This assumes that sub-cloud motions are dominated by turbulent eddies and average to zero over a sufficiently long time, T, i.e. $\frac{1}{T}\int_0^T w dt = 0$ for large T in the MSc drizzle regions. This is not necessarily a good assumption in convective rain shafts, where the drag associated with the falling drops can cause downdrafts. However, the intensities of precipitation encountered here are roughly two orders of magnitude smaller, and thus we assume that the drizzle-induced downdraft is negligible.

From Equation (3.2.1), the change in diameter of a falling drop over time is:

$$\frac{dD}{dt} = \frac{4\alpha_v \bar{f}_v}{\rho_l D} \left(\rho_{v,\infty} - \rho_{v,D} \right) \tag{3.2.3}$$

where ρ_l is the density of liquid water. Warming occurs within the cloud layer when the condensation of water molecules releases latent heat, and cooling occurs in the sub-cloud layer due to evaporation. The heating rate associated with a single drop growing by condensation (or shrinking by evaporation) is:

$$\dot{q}(D) = \frac{dq}{dt} = L_e \dot{m}(D) \tag{3.2.4}$$

where q is enthalpy, and L_e is the latent heat of evaporation (*Pruppacher and Klett*, 1997, p. 542).

If we discretize the size distribution measured by the combination of the F-PDI and CIP into bins, and assign the diameter and concentration in the i^{th} bin to be D_i and N_i, respectively, then the total latent heating rate (in units of $\mathrm{W\,m^{-3}}$) associated with each size bin is:

$$Q_i(D_i) = L_e \dot{m}_i N_i \tag{3.2.5}$$

and the associated cooling rate C (in units of $\mathrm{K\,s^{-1}}$) is given by:

$$C_i(D_i) = -\frac{L_e \dot{m}_i N_i}{\rho_a c_{pa}} \tag{3.2.6}$$

where ρ_a and c_{pa} are the density and specific heat capacity of air, respectively. The total latent heating rate Q and cooling rate C is the sum over all n drop bins:

$$Q(z) = \sum_{i=1}^{n} Q_i \text{ and } C(z) = \sum_{i=1}^{n} C_i \tag{3.2.7}$$

where we now show Q and C to be explicitly dependent on altitude z, reflecting the altitude-dependence of the drop size distribution in the sub-cloud layer due to drop evaporation.

To generate the sub-cloud profiles $Q(z)$ and $C(z)$, observed drop size distributions from only the cloud base legs are simulated as falling at their terminal velocity. Because the air below is assumed to be sub-saturated, the drops also begin to evaporate (Eq. 3.2.1) and cool the surrounding air (Eq. 3.2.6). As they evaporate, their size and terminal velocity decreases, which changes the subsequent cooling rates. Note that $\dot{m}_i$ depends on the sub-cloud moisture profile $\rho_{v,\infty}$ which is determined from a relative humidity profile measured by the Twin Otter. For this calculation, we assume that the moisture from evaporation does not significantly change the background water vapor content $\rho_{v,\infty}$ and hence there is no feedback between falling drizzle and evaporation. This assumption is reasonable provided turbulent mixing occurs quickly enough to smooth out any mois-

ture and temperature gradients created by the drizzle. Because the drops are assumed to fall independently, we compute $Q(z)$ and $C(z)$ by summing the contributions over all bins of the drop size distribution (Eq. 3.2.7). Because we initialize the calculation using 1-s cloud base size distributions, these calculations result in latent heating and cooling rate profiles beneath each cloud base leg that are horizontally-resolved at the same time resolution, which corresponds to $\sim$50 m. These profiles form the basis for all the other calculations performed in this study.

3.2.2 APE Calculations

Available Potential Energy (APE) was introduced by *Lorenz* [1955] to describe the potential energy stored in the spatial (both horizontal and vertical) distribution of potential energy:

> The available potential energy... may be defined as the difference between the total potential energy and the minimum total potential energy which could result from any adiabatic redistribution of mass. It vanishes if the density stratification is horizontal and statically stable everywhere, and is positive otherwise.

In stratocumulus-topped boundary layers, potential energy is created when sub-cloud evaporation causes localized cooling in two ways: (1) the upper-reaches of the sub-cloud layer are preferentially cooled (Sect. 3.3 below) relative to lower altitudes; and (2) cooling is horizontally inhomogeneous. APE measures the maximum potential energy release that could occur if the cold air in the evaporating drizzle shafts sinks, while warmer, more buoyant air rises to replace it. The resulting increase in turbulent kinetic energy (TKE) can enhance momentum, moisture and energy fluxes in the sub-cloud layer, with

feedbacks to properties of the Sc layer and drizzle derived from it.

The enthalpy (per unit mass) h of an air parcel is given by:

$$h = c_{pa}\theta \left(\frac{p}{p_0}\right)^{\kappa} \tag{3.2.8}$$

where θ and p are the parcel's potential energy and pressure, respectively, and p_0 is a reference pressure and $\kappa = R/c_{pa}$. Following *Randall and Wang* [1992], if a cold air parcel "c" at a higher altitude (lower pressure) exchanges places with a warmer air parcel "h" at a lower altitude (higher pressure), both with equal masses, then the net change in enthalpy is given by:

$$\Delta h = c_{pa}(\theta_h - \theta_c)\left[\left(\frac{p_c}{p_0}\right)^{\kappa} - \left(\frac{p_h}{p_0}\right)^{\kappa}\right] \tag{3.2.9}$$

which is a negative value. This implies total enthalpy of the system decreases due to the exchange, which increases some other form of energy such as TKE. The negative of this enthalpy change is termed the system APE and has units J/kg. This equation assumes the absence of moist processes occurring in response to the re-arrangement of air. This equation can be generalized to the re-arrangement of n parcels of air, all of equal mass, and re-written in terms of altitude z rather than pressure as:

$$\text{APE} = \frac{c_{pa}\kappa}{H}\sum_{j=1}^{n}\theta_j(z_{f,j} - z_{i,j}) \tag{3.2.10}$$

where z_f and z_i are the final and initial altitudes of the air parcel. Deriving Eq. 3.2.10 also assumes that pressure decreases exponentially with a scale height H. Note that for calculations of APE for circulations that extend through a large fraction of the troposphere, Eq. 3.2.10 should not be used because it assumes that $z << H$ for all air parcels.

If drizzle falls into a layer which initially has constant θ (both horizontally and ver-

tically), then given a cooling rate $C = -dT/dt \simeq -d\theta/dt$ due to evaporation, Eq. 3.2.10 can be re-written as:

$$\frac{d(\text{APE})}{dt} = \frac{c_{pa}\kappa}{H} \sum_{j=1}^{n} C_j(z_{i,j} - z_{f,j}) \tag{3.2.11}$$

where the left-hand side is now the rate of potential energy generation. Eq. 3.2.11 utilizes an idealized scenario and therefore should be viewed as an estimate of the actual rate of APE formation. One advantage of the simple reference condition is that *relative* APE generation rates for different drizzle conditions can be accurately computed.

For this study, we use aircraft measurements of cloud base drizzle to estimate cooling rate profiles (Sect. 3.2.1) over a horizontal distance, i.e. $C = C(x, z)$. To calculate APE generation rate, C is calculated for constant *mass* bins in the vertical dimension, which requires the grid Δz to increase with altitude as pressure drops. The initial condition assumes that the surface pressure is 101.325 kPa and that the sub-cloud layer is well-mixed such that $\theta(x, z) = 290$ K. The cooling rate distribution $C(x, z)$ is calculated for each flight leg at cloud base assuming that the measured drizzle is exactly at cloud base at an altitude of $z = 200$ m. To calculate APE generation rate, $C(x, z)$ is sorted from largest to smallest values, which are then assigned to their final altitude bins from lowest to highest z. Thus, each parcel j has associated with it a cooling rate C_j and a change in altitude $\Delta z_j = z_f - z_i$, after which we apply Eq. 3.2.11 to compute the total APE generation rate.

3.3 Results and Discussion

The goal of this research is to study the effects of drizzle via evaporation in the sub-cloud layer and its subsequent influence on the MBL. Just as in Chapter 2, this study will only focus on four MASE flight days: the 14, 15, 16, and 17 of July, 2005 (referred to hereafter as Day 14 to Day 17, respectively). Microphysical data was retrieved by

performing horizontal flight legs through the MBL, both in and out of cloud. In-cloud flight leg data at 3 levels, cloud top (CT), mid-cloud (MC), and cloud base (CB), were extracted for analysis (see Chapter 2 for more detail on how flight legs were characterized). The evaporation calculations were made utilizing only data from the CB legs, although conclusions regarding the structure of drizzle, which were found in Chapter 2 and which are critical for this study, utilized the flight leg data at CT and MC as well.

3.3.1 Sub-cloud Average Drizzle Flux

We first examine the integrated evaporative heat flux, F_{tot}, for each CB layer as shown in Fig. 3.1. The range of mean BL cooling rates ranges from 0.6 to 4.8 W/m^2. These values are somewhat smaller than the net cloud-top radiative cooling that drive daytime marine stratocumulus. At night, in the absence of sunlight, net IR cooling at the top of the MBL has a typical value of 50 W/m^2, but varies primarily with cloud top temperature and the column water vapor content above the cloud. During the day, absorption of shortwave radiation by the cloud and at the surface reduces the net cooling to typical values of $\sim$ 10 to 20 W/m^2, with a strong dependence on time of day and cloud liquid water path. Very roughly, then, the calculated energy flux associated with drizzle may range from less than 1% to almost 50% of the overall radiative flux driving the system during the daytime Sc-topped BL.

Vertically-resolved (but still horizontally-averaged) profiles of sub-cloud evaporative cooling rates are shown in Fig. 3.2 with associated cooling rates (K/day) available on the top axis. Each profile was calculated using data retrieved from a single CB leg, therefore the number of profiles presented (3, 1, 2, 2) corresponds to the number of CB flight legs flown on each day (Days 14 to 17, respectively). Each of these legs is $\sim$10 min in duration, which corresponds to $\sim$30 km in length. Each CB leg is labeled with a number corresponding to the day it was performed (14-17) and a letter corresponding

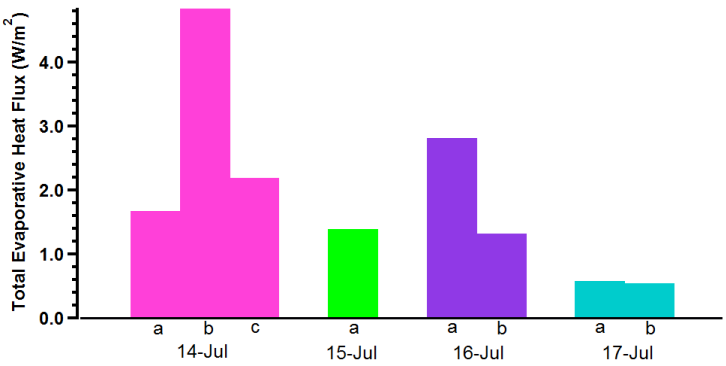

Figure 3.1: Computed mean drizzle flux
Computed mean drizzle flux, F_{tot}, for each CB leg during each MASE day. Values range between 0.6 to 4.8 W/m^2.

to the order in which the leg was performed: 1st leg = a, 2nd leg = b, and 3rd leg = c. This notation will be used on additional plots and throughout the discussion. Figure 3.2 shows the vertical profile of the drizzle-induced cooling rate. Note that these curves are plotted until the drizzle completely evaporates. It is possible, of course, for drizzle to reach the surface before completely evaporating. We do not account for the actual cloud base altitudes from these legs for these calculations because we are interested more generally in the range of possible effects that drizzle could have on the sub-cloud layer, rather than in the specific effects during these exact flight legs.

All curves in Fig. 3.2 have a characteristic distribution, with variability expressed in both the peak magnitude and width; among the eight flight legs, these two properties are found to vary independently of each other, i.e. are uncorrelated (data not shown). Because drizzle drops are largest immediately after they leave cloud base, Eq. (3.2.1) suggests evaporation should also be greatest in this region. But Fig. 3.2 shows Q does not reach its maximum until some distance below cloud base. There are two reasons for this: (i) because drizzle drops are largest in this region, they fall at their greatest terminal velocities, spending the least amount of time directly under cloud base; and (ii) because relative humidities at the top of the sub-cloud layer are close to 100%, evapora-

tion is slow and thus does not reach its max until some distance below cloud base when $\rho_{v,\infty}$ is significantly larger than $\rho_{v,D}$ (Eq. 3.2.1).

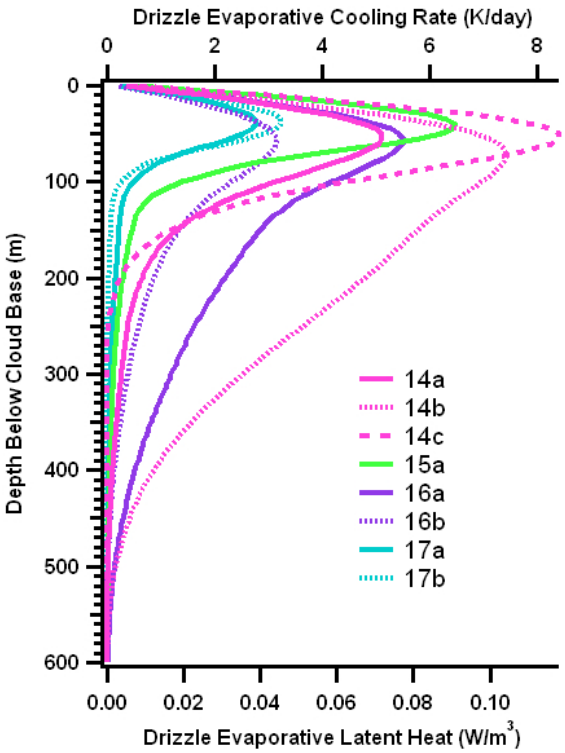

Figure 3.2: Sub-cloud evaporation profiles
Computed sub-cloud evaporation latent heating profiles, $Q(z)$, (W/m^3, bottom axis) and cooling rates, C(z), (K/day, top axis). Calculations are run until all drizzle evaporates and do not account for the surface location on these days (see text).

Maximum cooling occurs 40-45 m below cloud base (BCB) on Days 15/17 and 55-60 m BCB on Days 14/16. The only exception is 14b when peak cooling occurs 70-75 m below the cloud. The evaporation profile for this leg is also notable because it shows significant evaporation well-below the altitude of peak cooling. Both profiles on Day 16 also show evaporation penetrating far beneath cloud base but to a lesser extent than 14b. These three profiles exhibit evaporation that is not confined to a single layer beneath the cloud but instead extends throughout the depth of sub-cloud layer.

While the largest F_{tot} values are associated with profiles that extend far beneath the cloud layer (14b and 16a), *Feingold et al.* [1996] found that there is no clear dependence of BL dynamics on F_{tot} (Fig. 3.1). Like MASE clouds, evaporation in the *Feingold et al.* [1996] study was either constrained to a layer directly below CB or was spread throughout the sub-cloud layer. In the former case, cooling destabilizes the BL, producing deeper circulation and increased turbulence, whereas in the latter case, cooling stabilizes the BL, circulation is weakened and the BL becomes less well-mixed. Therefore, their results suggest two opposite ways in which the evaporation of drizzle affects BL dynamics. The observationally-based cooling profiles from Fig. 3.1 do show variability in the distribution of cooling through the boundary layer. For example, Fig. 3.1 shows F_{tot} on 16b and 15a are of similar value (1.3 and 1.4 W/m^2, respectively), but the profiles from these two CB legs are starkly different (Fig. 3.2) and thus it is possible that their effects on the BL are also very different. Closer comparison of the drizzle fluxes in Fig. 3.1 with those from *Feingold et al.* [1996] (c.f. their Fig. 8), however, suggests that *all* profiles from this study much more closely resemble the profile that *Feingold et al.* [1996] suggests produces destabilization of the BL, while none resembles the BL stabilization cooling profile. This does not imply that evaporation of drizzle can not stabilize the BL, but rather that the stabilization caused by cooling the sub-cloud layer is counter-acted to some degree by the enhancement of TKE in this layer. We speculate that which effect dominates depends at least partly on the degree to which sensible heat and TKE in the sub-cloud layer are turbulently transported upward into the cloud layer. We will examine further the impact of cooling profiles on dynamics below (Sect. 3.3.4)

Days 14/16 in Fig. 3.2 show a significant amount of cooling occurs far beneath cloud base, much farther than the height of a typical cloud base. This implies that much of the liquid water leaving the cloud as drizzle is not completely evaporated in the sub-cloud layer. Instead, moisture is lost at the surface, removed from the system altogether. This will tend to dry the BL and hence reduce cloudiness. Days 15/17, on the other

hand, show almost an entire loss of drizzle in the sub-cloud layer, allowing moisture to be recycled back into the cloud. Total evaporation of drizzle in the sub-cloud layer has also been observed in simulations [*Ackerman et al.*, 2009; *Wang and Feingold*, 2009] and other field studies [*Wood*, 2005; *vanZanten et al.*, 2005].

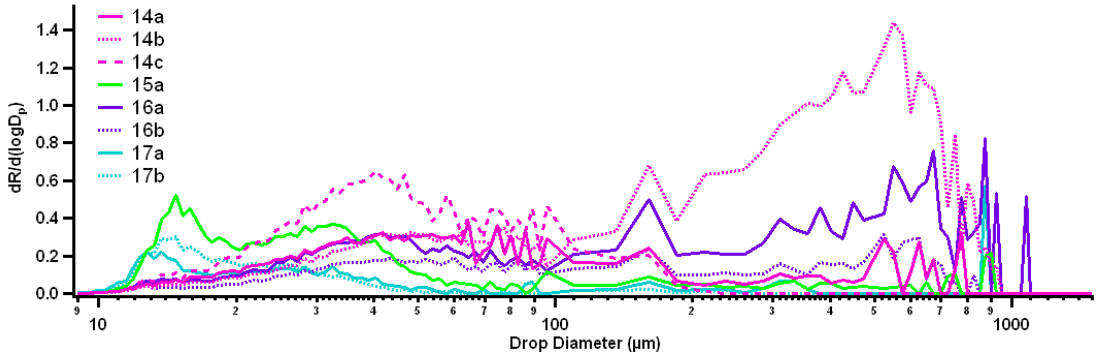

Figure 3.3: CB R distributions
R distributions for each CB leg. Note that the implementation of a CIP concentration correction factor lowered the concentration of all CIP diameters before 161 μm, leading to a jump in the drizzle distribution at this size. This artifact does not significantly affect the data or any interpretations made in this study.

3.3.2 Relationship between R distributions and cooling profiles

Comparison of the drizzle rate (R) distributions and the profiles of sub-cloud evaporative latent heat flux shows a relationship between the shape of the R distributions (Fig. 3.3) and the shape of the evaporation profiles (Fig. 3.2). Note that $\overline{R}$ values for each CB leg, presented in Table 3.1, directly correlate to the evaporative F_{tot} values in Fig. 3.1 since all drizzle is assumed to evaporate rather than deposit at the surface.

The drizzle rate distributions for 14b, 16a and 16b have the greatest contribution of drizzle from the larger drop sizes (seen as a 2nd mode at larger drop sizes, $D > 100$ μm). The corresponding evaporative heat flux profiles for these days extend throughout the

depth of sub-cloud layer. R distributions for Days 15/17 are dominated by contributions from drops smaller than 100 µm and correspond to flux profiles in which evaporation is confined to the layer just beneath cloud base. Because large drops increase the depth to which drizzle falls, the drizzle lost at the surface is comprised of the largest CB drops, while total evaporation to the sub-cloud layer is a result of drizzle comprised mostly of small drops. Results from *Feingold et al.* [1996] show a similar relationship. In their study, drizzle comprised of large drizzle drops resulted in 85% more precipitation to reach the surface than their reference case, in which drizzle was comprised primarily of small drops. *Comstock et al.* [2007] similarly showed radar reflectivity values diminished more slowly below cloud than drizzle rate values because small drops contribute proportionately less to the reflectivity than large drops.

$\overline{R}$ (mm/day)				
	14-Jul	**15-Jul**	**16-Jul**	**17-Jul**
leg a	0.290	0.244	0.488	0.102
leg b	0.837	-	0.230	0.096
leg c	0.379	-	-	-

Table 3.1: Leg-averaged drizzle rates
Average drizzle rate during each cloud base leg. A dash (-) means no second or third CB leg was performed.

The dynamical response of the BL has been shown to be dependent on the sub-cloud evaporation profiles but the evaporation profiles are themselves dependent on the drizzle distributions. Just as F_{tot} values alone cannot determine the dynamical response to the BL, neither can $\overline{R}$. A closer look at Day 15, discussed in Chapter 2 as an interesting case, reinforces this point while also highlighting the importance of having accurate measurements of drops at smaller sizes. While the contribution from larger drop sizes is minor, its total drizzle rate is significant, comparable to CB drizzle rates comprised of

well-developed drizzle drops (16b, Table 3.1). In the past, studies have often disregard the contribution of small drops when calculating sub-cloud evaporation rates. A strong R comprised entirely of small drops, causing a vertically thin region of intense cooling can disrupt the BL just as significantly as drizzle comprised mostly of large drops.

3.3.3 Horizontal Variability in Sub-cloud Drizzle Flux

We now focus on examining the *horizontal* variability of drizzle and how it can interact with MBL dynamics. Past studies have linked the horizontal variability of drizzle, even in lightly drizzling clouds (with surface drizzle as low as 0.02 mm/day; *Wang and Feingold*, 2009), and its subsequent evaporation, to breakup of the stratocumulus layer [*Comstock et al.*, 2007; *Stevens et al.*, 2003, 2005; *Sharon et al.*, 2006; *Petters et al.*, 2006]. Thus, we now turn our attention to studying the horizontal variability in sub-cloud evaporation during MASE and its possible affects on MBL dynamics, other MBL processes, and cloud lifetime.

Using the methods described in Sect. 3.2.1, 1-s measurements of DSD are used to estimate the horizontal and vertical structure of sub-cloud cooling for each of the eight CB legs; of these, four are presented in Fig. 3.4. Warm colors represent intense cooling, reaching as high as 330 K/day during moments of severe drizzle, while cool colors represent lower cooling rates. For reference, the corresponding time-averaged cooling profiles have also been plotted. Variability among the eight different evaporation fields is large. The four plots presented in Fig. 3.4 are reasonably representative of the range of evaporation fields among the eight days. Areas of interest within each evaporation field are labeled A, B, C, etc. above each panel in Fig. 3.4 for ease of reference.

The uppermost panel in Fig. 3.4 corresponds to 14b, the leg with the largest $\overline{R}$ (F_{tot}) and the leg which exhibits evaporation extending well into the sub-cloud layer (Fig. 3.2). Excluding the intermittent spikes to greater depths associated with intense

cooling, evaporation is confined primarily to first ∼250 m (ranging between 120-320 m) BCB. Cooling rates are variable over many different length scales, mostly alternating between low cooling rates (<1 K/day) and moderate cooling rates (7 K/day).

The vertical lines extending past the region of bulk cooling, penetrating deep into the sub-cloud layer, are patches of intense evaporation; their number and intensity are unique to this leg across all four days. Moments of intense cooling (colored red) seem to occur at random and are more likely to occur within clusters of high cooling rates (like areas A and D), although not exclusively (point C). Over the entire CB leg, the two largest regions of strong cooling, areas A and D, extend over ∼200 s, corresponding to ∼10 km. Patchiness is also not confined to areas of high evaporation. Region B is a long (∼ 10 km) section of low evaporation with small patches of higher cooling rates embedded within.

The second panel from the top corresponds to leg 14c (Fig. 3.4b). This panel contrasts with Fig. 3.4a in several ways. First, there are no patches of intense evaporative cooling to large depths below CB. Second, evaporation is higher and more uniform throughout the leg. Third, patches of high evaporation are limited to the thin layer just below CB where the bulk of the cooling takes place. And finally, variability during this leg appears to exhibit a lower frequency relative to leg 14b, such that the patches of highest evaporative cooling are embedded within areas of already moderately high evaporation. This leg is unique in the fact that evaporation is strong, consistently stronger than 14b, but never reaches the level of patchiness seen in 14b. The majority of the cooling is focused between 10 and 110 m BCB, resulting in a Q profile with the largest peak cooling (Fig. 3.2). Similar to 14b, evaporation extends to ∼250 m (ranging between 120 and 320 m) BCB.

Leg 16b (Fig. 3.4c) exhibits evaporation that is light and patchy. Its patchiness appears comparable to 14b but cooling rates are consistently much smaller than either previous panel. The leg contains only several seconds of high evaporation which pene-

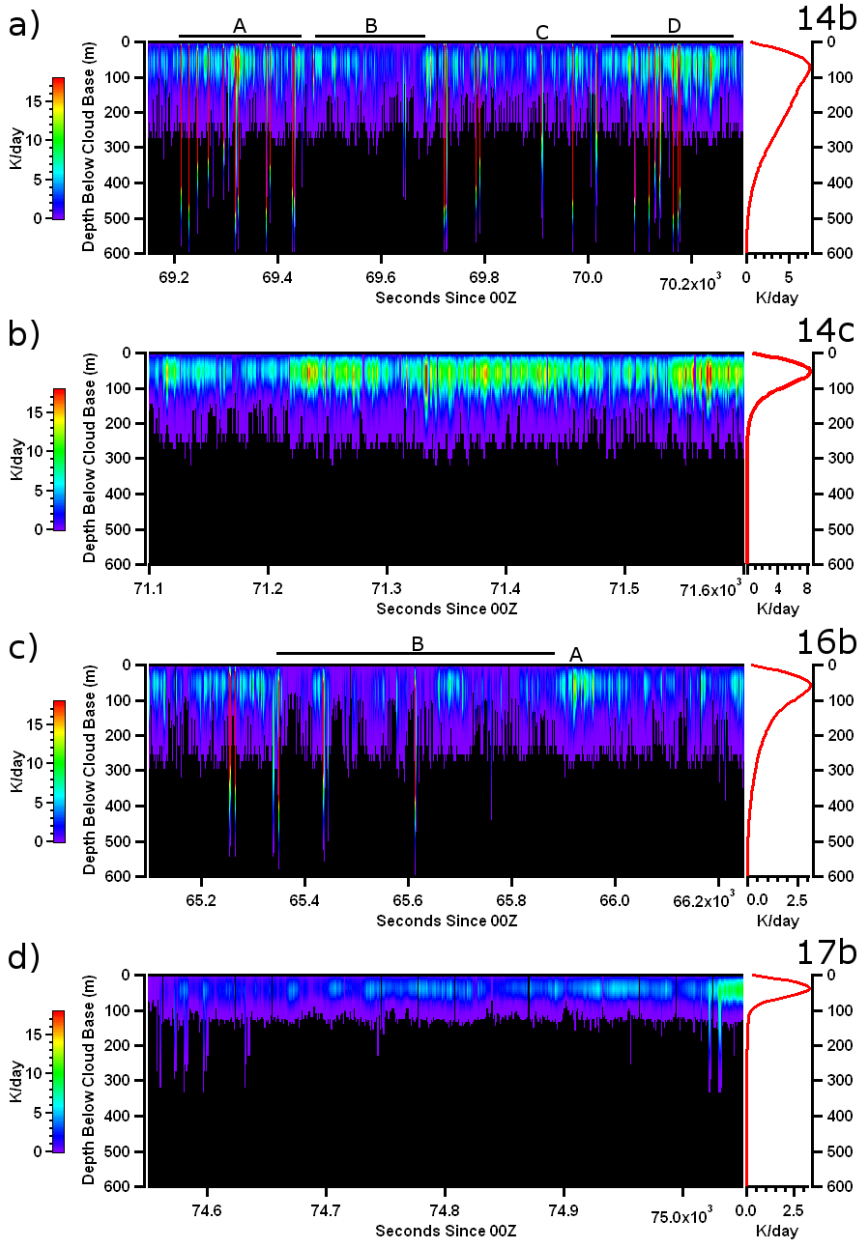

Figure 3.4: Sub-cloud evaporative cooling fields

Computed sub-cloud evaporative cooling (K/day) for four of the eight CB legs during MASE: (top to bottom) legs 14b, 14c, 16b, and 17b. The horizontal axis is time in seconds from 0Z on that day. Tick marks are separated by either 100 or 200 s, which correspond to ∼5 km and 10 km, respectively. To the right is the time-averaged cooling profile (replicated from Fig. 3.2) for reference.

trate deep within the sub-cloud layer and they do not appear to be embedded within clusters of stronger evaporation. Excluding these patches, only one instance of evaporative cooling larger than 7 K/day exist and is found at point A. Similar to the top two panels, the evaporation extends to ∼120-320 m BCB but, during this leg, it is much more variable, frequently bouncing between high and low depths. Also unique to this observational period is the high frequency of cooling rates < 1 K/day. Within the middle 450 s of the leg (region B), these instances are in the majority. The corresponding Q profile is very similar in shape to 14b but with a peak value that is three times smaller (Fig. 3.2).

The last panel corresponds to leg 17b (Fig. 3.4d), which is again different from the others described so far. Evaporation is uniform and light, with only one cluster reaching 8 K/day at the tail end of the flight leg. Evaporation profiles for Day 17 show that the cooling occurs almost entirely between 0 and 100 m BCB.

Legs that are not shown generally behave similarly to the ones shown in Fig. 3.4; sometimes they exhibit features from a combination of two of the legs presented in Fig. 3.4, and sometimes they share similarities with a single leg. Therefore Fig. 3.4 is a good representation of evaporation seen throughout the four MASE flights but does not fully represent the diversity of the evaporation fields.

Several interesting observations can be made from Fig. 3.4 which lead to conclusions regarding the structure of sub-cloud evaporation. First, variability occurs over a wide range of length scales, from the highest resolution of our data (50 m) up to scales of 10 km. Also, high and low variability in cooling do not correlate with, respectively, strong and weak mean cooling, as demonstrated by legs 16b and 14c. A single flight can contain CB legs which have very different evaporation fields. For example, legs 14b and 14c (Fig. 3.4a and b) exhibit strong and weak patchiness, respectively. This is notable because the aircraft samples the stratocumulus layer in a Lagrangian fashion by advecting with the mean wind. The two very different evaporation profiles from legs

14b and 14c suggest either strong variability in time of these profiles since they occur 30 mins apart, or that such profiles are highly variable in space, as the aircraft stays roughly in the same volume of air, but with some uncertainty that is on the order of a few kilometers. In contrast, 17a (not shown) is almost identical to 17b shown in panel (d), illustrating that heterogeneity is not always observed. In summary, the four MASE days presented here show a diverse range of evaporation fields, with each panel individually illustrating the complex nature of evaporation. The fate of the cloud layer is often determined by the complexities found in the sub-cloud evaporative cooling fields and therefore, in our last section, we attempt to predict how the MBL will evolve in response to the variability of evaporation.

3.3.4 Available Potential Energy

Available potential energy (APE) is one way to assess the impact of the heterogeneity of sub-cloud evaporation, both vertical and horizontal, on the sub-cloud layer. In particular, it is a consistent way to assess the potential for density gradients to generate turbulent kinetic energy in the sub-cloud region, which subsequently impacts key BL processes such as moisture and energy fluxes which can feed back to properties of the stratocumulus layer.

For each CB leg across the four study days, we compute the rate of APE generation using the method outlined in Sect. 3.2.2. As discussed above, we assume for the purposes of this calculation that each CB leg occurs at an altitude of 200 m, which does not reflect the actual altitude of this leg in all cases (Table 1.3). We also assume that the drizzle falls into a well-mixed cloud layer with constant $\theta = 290$ K and surface pressure P =101.325 kPa. These assumptions are made in order to be able to directly compare the APE generation rates from different days independent of the characteristics of the sub-cloud layer on these different days.

To put the APE calculations in context, we also compute APE for an idealized daytime MSc case. We chose a daytime reference case because the MASE flights took place during the day rather than at night. We consider a case where the sub-cloud layer is 200 m thick and is topped by a 100 m thick MSc layer. The top 10 m of the cloud layer is cooled at a rate of 100 K/day, which is the equivalent of a net cloud-top radiative cooling of 14 $\mathrm{W\,m^{-2}}$. This value is low relative to nocturnal MSc; *Roach et al.* [1982] find a net cloud-top cooling equivalent to 45 $\mathrm{W\,m^{-2}}$, about three times higher. *Nicholls* [1984] show daytime calculations where shortwave absorption almost exactly cancels the longwave emission, although this is very sensitive to the solar insolation. Thus, our reference case lies in between these two extremes. Additionally, we consider a surface heating via a sensible heat flux of 2 $\mathrm{W\,m^{-2}}$, which we estimated from aircraft measurements of coastal MSc during the VAMOS Ocean-Clouds-Atmosphere-Land Study (VOCALS).

The results of all APE calculations are shown in Fig. 3.5. The daytime reference case yields an APE generation rate of 4.3 $\mathrm{cm^2\,s^{-3}}$, which is consistent with (though

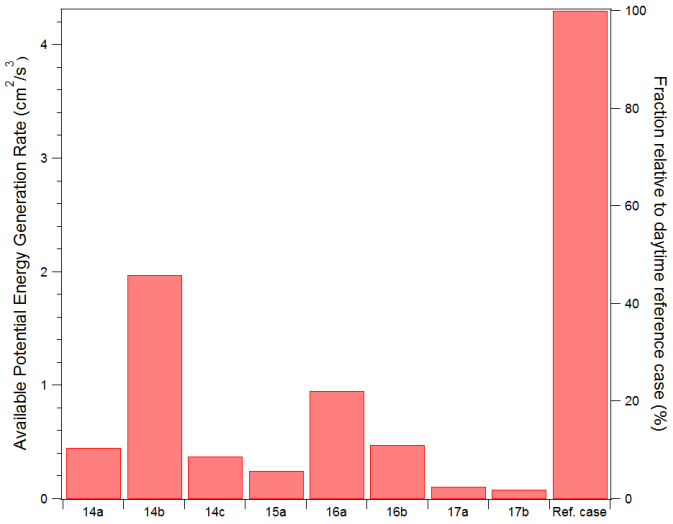

Figure 3.5: Available potential energy
The drizzle-induced APE rates for the 8 sampled CB legs and, for comparison, a reference case. Results range from 0.08 to 2.0 $\mathrm{cm^2\,s^{-3}}$.

larger than) measurements of mean mixed-layer energy dissipation rate ε of 1 $\mathrm{cm^2\,s^{-3}}$ in stratocumulus [*Siebert*, 2010; *Pinsky et al.*, 2010], especially if some inefficiency in the conversion of APE to TKE is accounted for. The drizzle-induced APE generation rates range from 0.08 to 2.0 $\mathrm{cm^2\,s^{-3}}$, which correspond to 2 to 46% of the reference case. Out of the eight CB legs considered, the two highest APE generation rate values represent 46 and 22% compared to the reference, and the next three highest values range from 9 to 11%. If instead we use the measured mean ε of 1 $\mathrm{cm^2\,s^{-3}}$ as a comparison, drizzle production represents 8 to 200% of ε, with a median value of 40%, albeit only for the sub-cloud layer and not for the entire boundary layer. Since we typically think of stratocumulus being driven by cloud-top cooling, these results suggest that the additional TKE driven by the evaporation of drizzle can be a significant fraction of the total BL TKE budget.

The distribution of the APE-generated TKE differs from that produced by cloud top radiative cooling because it is formed primarily in the sub-cloud layer. The additional TKE generated via APE can alter key fluxes such as the surface sensible heat, moisture/latent heat, and momentum fluxes, with consequences for Sc properties. For example, an increase in the surface moisture flux can help replenish the cloud layer of water vapor lost via drizzle, which is could then support further drizzle. TKE generated in the sub-cloud layer may also affect entrainment differently from that generated at cloud top. An entrainment closure proposed by *Lilly* [2002] weights turbulence at cloud top more heavily than the lower portion of the boundary layer in order to emphasize the importance of local, small-scale turbulent eddies on entrainment rate. Increasing TKE in the lower region of the MBL without changing that at cloud top could thereby alter the evolution of the cloud layer by, for example, increasing the moisture source (surface fluxes) relative to entrainment, a key moisture sink. Furthermore, this tendency could potentially be strengthened by the evaporative cooling which will tend to de-couple the sub-cloud layer from the cloud layer, thus exporting less TKE to the cloud layer,

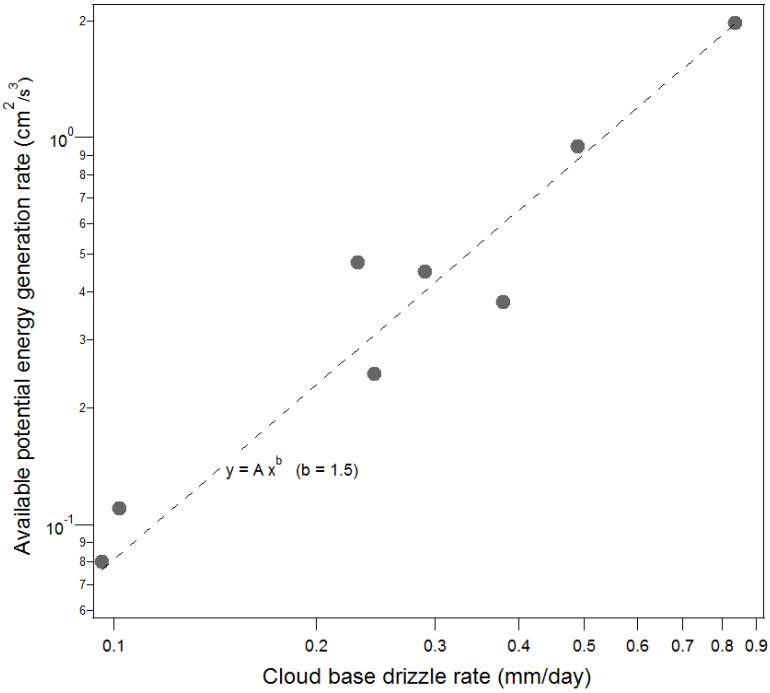

Figure 3.6: APE compared to mean CB drizzle rate
Comparison of calculated APE with mean cloud base total drizzle rate for the eight MASE legs. The line represents a power-law fit to the data, as illustrated.

although de-coupling also cuts off the cloud layer from the surface moisture flux.

Because APE considers the horizontal and vertical distribution of cooling due to drizzle, it is not a given that it will correlate well with mean drizzle properties where the detailed drizzle structure is not considered. Figure 3.6 compares APE generation rate with the mean cloud base drizzle rate on for the eight MASE legs. While there is some scatter, a simple power law fit appears to match reasonably the data, with the points farthest from the line being within a factor of 1.6 of the best-fit value. Note that this result does not account for the vertical structure of APE generation, which also may change for different cooling rate structures. If it were found, after adding data from a wider range of conditions, that APE generation generally increases with drizzle rate, then this relationship could potentially be used to simply parameterize this effect in large-scale models covering stratocumulus regions.

3.4 Conclusions

Drop size data used in this research was collected by the F-PDI and CIP probes in the summertime MSc cloud deck off the coast of central California during the MASE project in July 2005. Using measured DSD from different cloud base flight legs, we calculate profiles of latent heating $Q(z)$ and the associated cooling rates $C(z)$. We utilize the concept of available potential energy (APE) to estimate the effects of evaporation on the dynamics of the MBL, which has not been previously examined observationally. APE accounts for both vertical and horizontal gradients in cooling rates which generates buoyancy gradients that can be converted into turbulent kinetic energy (TKE). The following is a summary of the main findings regarding sub-cloud evaporation within the MBL:

- The range of mean BL cooling ranges from 0.6 to 4.8 W/m^2 which corresponds to 1 to 50% of the overall radiative flux driving a daytime Sc-topped BL.
- All evaporation cooling profiles have a characteristic distribution, with variability expressed in both the peak magnitude and width; among the eight flight legs, these two properties are found to vary independently of each other.
- Profiles for three CB legs (14b, 16a, and 16b) exhibit evaporation that extends throughout the depth of sub-cloud layer, much farther than all other legs. These legs have the greatest contribution of drizzle from the larger drop sizes, which explains the greater depth to which evaporative cooling occurs.
- The three flight legs on days 15 and 17 are dominated by contributions from drops smaller than 100 µm and correspond to flux profiles in which evaporation is confined to the layer just beneath cloud base.
- Evaporation fields show variability occurs over a wide range of length scales, from

the highest resolution of our data (50 m) up to scales of 10 km.

- High and low horizontal variability in cooling do not correlate with, respectively, strong and weak mean cooling, as demonstrated by comparing legs 16b and 14c (Fig. 3.4).

- The drizzle-induced APE generation rates range from 0.08 to 2.0 $\mathrm{cm^2\,s^{-3}}$, which are significant relative to the computed mean energy dissipation rates of $\sim 1\ \mathrm{cm^2\,s^{-3}}$ in stratocumulus from previous studies [*Siebert*, 2010; *Pinsky et al.*, 2010]. These results suggest that the additional TKE generated by the evaporation of drizzle can be a significant fraction of the total BL TKE budget.

A number of assumptions were made in this study, and result in important caveats:

- The sub-cloud layer into which the drizzle falls is idealized. There is no horizontal variability in the thermodynamic properties of this layer.

- As drizzle evaporates, we assume that the environmental moisture and temperature stays constant and does not feed back to evaporation rates, which could lead to over-estimation of the latter. However, the drizzle rates in this study are very low and therefore it is unlikely this effect is large.

- Our calculations assume no turbulent mixing occurs. This could affect, for example, the horizontal variability in cooling since mixing would tend to reduce strong gradients.

Our results show that the evaporation of drizzle in the sub-cloud layer can be an important process within the MBL that can have large implications for both boundary layer

dynamics and cloud lifetime. The implications of this research support other modeling and radar work by *Nicholls* [1984]; *Paluch and Lenschow* [1991]; *Wang* [1993]; *Wang and Wang* [1994]; *Feingold et al.* [1996]; *Stevens et al.* [1998], with new implications for BL turbulence.

Chapter 4

How is drizzle initiated in stratocumulus?

The most fundamental parameter of cloud microphysics, drop size distribution (DSD), is strongly linked to the formation of precipitation. For this reason, accurately modeling the evolution of the DSD through time has been a goal of scientists for decades. While the most basic collision models can accurately simulate DSD growth, eventually forming precipitation, the timescales associated with the theoretical solutions are much larger than those observed. It has been shown that the appearance of large, collisionally-formed drops at cloud top (CT) aid in accelerating drizzle formation. The question then becomes: what CT processes are responsible for the formation of these large drops? Here, we utilize DSD measured from *in situ* aircraft instruments and derived from box model simulations to calculate CT collision rates in marine stratocumulus clouds (MSc). We found the collision rates derived from observations follow a power law. The observed slope, m, varied between 2.5 and 3.5, for a well-developed and a less-developed CT, respectively. Attempts to correlate m with other cloud properties failed, prompting the calculation of collision rates using DSD from box model simulations. While model

results suggest collision rates are closely linked to properties such as turbulence, cloud seeds, and cloud drop residence time, it is insufficient to produce observed CT collision rates. Our results suggest that a box model does not represent cloud top properties well. Nevertheless, observational results can serve as good constraints for more sophisticated model development, particularly at CT and for the MSc regime.

4.1 Introduction

One of the most fundamental goals of cloud physics is to accurately represent the evolution of cloud drop populations. Starting with drop activation at cloud base and ending in precipitation or evaporation, the processes which govern the growth of cloud drops has yet to be fully understood. The most basic microphysical description of a cloud is the drop size distribution (DSD), which characterizes the drop concentration as a function of size. The DSD has been shown to (i) control the radiative and reflective properties of the cloud, (ii) affect the formation of precipitation, determining the lifetime of a cloud, and (iii) regulate the amount liquid water content of the cloud, determining the latent energy balance of the atmosphere. It is for these reasons that DSD is one of the most important parameterization used in climate models, models which often have a hard time accurately representing clouds [*IPCC*, 2007; *Bony et al.*, 2006; *Cronin et al.*, 2006; *Wyant et al.*, 2006; *Bony and Dufresne*, 2005].

As mentioned, the initiation of cloud formation, and thus DSD development, begins with the condensation of water vapor onto cloud condensation nuclei. Condensation also accounts for the growth of small cloud drops but is too slow to explain the production of drops substantially larger than 20 μm. In this study, we focus primarily on the growth of the DSD through the process of collision-coalescence, the dominant growth mechanism for drops greater than 20 μm. Collision-coalescence is the process by which cloud droplets collide into each other and combine to form larger drops. It often occurs when drops

larger than their neighboring drops, and thus with larger fall speeds, sweep up smaller drops that lie in their path.

Attempts to model collision-coalescence began with the *Bowen* [1950]. The Bowen model assumes a uniform drop population and continuous growth (as opposed to discrete collision events). The model was successful in producing precipitation, although the required time was significantly longer than that found in nature. Therefore, later improvements in the representation of collision-coalescence focused on reducing growth time. At present, stochastic collection is believed to best represent cloud drop growth from collision-coalescence. This model assumes more realistic behavior. First, drizzle formation is derived from the evolution of the entire drop spectrum, not just of an average drop. Second, the spectrum evolves by discrete collisions and not through continuous growth. Third, collection efficiency is a function of the probability of random collisions.

Processes which control the shape of the DSD are especially important with respect to the low-lying marine stratocumulus clouds (MSc) which form over the eastern subtropical oceans in the summer months. Because MSc dominate the region in time (lasting up to several days) and in space (spanning up to 10^6 km^2), are highly reflective, and emit radiation close to the same temperature as the earth, they are the strongest negative forcing within the climate system, reducing the net radiation balance on a annually averaged global basis by $\sim$15 W/m^2 [*Hartmann et al.*, 1992; *Rogers and M.K Yau*, 1989; *Eastman et al.*, 2011]. More recent attempts to improve the representation of collision-coalescence have focused on the fact that the collection process is unique to cloud environments and types. Most important to this study is the fact that the marine boundary layer (MBL), the environment in which the MSc resides, is associated with a number of standard features which strongly affect the collision-coalescence process.

Especially strong changes of DSDs in MSc are related to drizzle formation (e.g., *Stevens et al.*, 1998; *vanZanten and Stevens*, 2005; *Petters et al.*, 2006). At the same time, the fundamental mechanisms of DSD and drizzle formation in stratocumulus clouds

are still not well understood. However, *Nicholls* [1987] proposed that turbulence plays a crucial role in MSc drizzle formation. Strong turbulence appears to keep small drizzle drops in circulation long enough to increase the collision-coalescence process and enhance drizzle formation. Model results by *Austin et al.* [1995] found that without strong turbulence, increasing autoconversion rates has little impact on the drizzle flux. More recently, *Feingold et al.* [1999] showed positive correlation between radar reflectivities (a proxy for drizzle) and in-cloud turbulence. Although the largest contributor to BL turbulence is cloud-top radiative cooling, entrainment generates negatively buoyant parcels near cloud top and therefore can also enhance turbulence. While entrainment dries the air, decreasing drop size and number, it also produces mixing thought to produce drops large enough to initiate the collision-coalescence process. Because drizzle, turbulence, and entrainment may operate simultaneously, their effects on DSD can be difficult to distinguish quantitatively. This problem is exacerbated by the fact that these three processes are linked and feedback on each other.

Collisional growth, whether by differential gravitational sedimentation or turbulence, is sensitive to the diameter of the largest drops. For cloud drop sizes, the probability of collisional growth generally increases rapidly with size, e.g. depends on $\sim D^4$ if only gravitational sedimentation is considered. Because cloud top is where the largest condensationally-formed drops are found, it is also the location where the first collisions are most likely to occur, making it a special place in a stratocumulus layer. Cloud top is also where turbulence tends to be strongest insuch systems since the buoyancy production of turbulent kinetic energy (TKE) is primarily generated from cloud top longwave radiative cooling. Previous observations based on radar show that drizzle is initiated very near to cloud top [*Vali et al.*, 1998; *vanZanten et al.*, 2005]. Therefore, if we seek to understand the mechanism by which drizzle is initiated in Sc, cloud top is the key region to study.

This study begins by taking an in-depth look at *in situ* cloud top drop distribution

(Sect. 4.3.1). Section 4.3.2 uses the observed cloud top DSD to calculate cloud top collision rates (Sect. 4.3.2). And finally, in Sect. 4.3.4, we presents calculations of CT collision rates derived from box model simulation, in an attempt to determine what controls the variability of collision-coalescence at cloud top.

4.2 Methods

4.2.1 Field observations

The research presented here utilizes DSD measurements from *in-situ* cloud probes and cloud-modeling simulations to compute cloud top collision rates. *In-situ* microphysical measurements come from instruments onboard the Center for Interdisciplinary Remotely-Piloted Aircraft Studies (CIRPAS) Twin Otter during the MArine Stratus/Stratocumulus Experiment (MASE) in July 2005 [*Lu et al.*, 2007], with additional contributions from Physics Of Stratocumulus Tops (POST) in July-August 2008 and VAMOS Ocean-Cloud-Atmosphere-Land Study (VOCALS) in November 2008 [*Wood et al.*, 2011]. While the focus of each field campaign varied, their goal was the same: to better understand summertime MSc over the Pacific. MASE and POST field campaigns investigated clouds off of the coast of central California while VOCALS focused on those off of the coast of northern Chile. Microphysical measurements used in this research come from two drop-measuring probes, the Artium Flight Phase Doppler Interferometer (F-PDI) and the Cloud Imaging Probe (CIP). A detailed description of the F-PDI and the CIP can be found in [*Chuang et al.*, 2008] and [*Knollenberg*, 1970], respectively. Specifics of the MASE field campaign and the F-PDI, as they relate to this work, can also be found in Chapter 1. To capture the whole range of drop sizes at the cloud base and mid-cloud levels, measurements from the F-PDI ($D < 98$ µm) were merged with those from the CIP ($98 < D < 1562$ µm). Cloud base (CB) and mid-cloud (MC) drop size data are only

presented for the MASE mission; all other data comes from cloud top (CT), utilizing F-PDI measurements alone. Modeled DSD come from the stochastic collection model described in *Bott* [1998] using the Hall kernel [*Hall*, 1980], a hydrodynamical– gravitational kernel. Specifics of the model are presented in Sect. 4.2.3. First, we describe the calculation of cloud top collision rates which form the basis of this study.

4.2.2 Collision Calculations

Cloud drops are nucleated at or just above the lifting condensation level and grow by condensation as they continue upward in the cloud. The number of drops activated at cloud base is determined by the available cloud condensation nuclei and the updraft speed. Condensational growth increases the mode of the DSD while drop concentrations remains constant. The effects of collision-coalescence on the DSD are two-fold: collision-coalescence causes a reduction in drop concentration and an increase in widths of the distributions at the larger drop sizes. Because collision-coalescence is strongly tied to the sedimentation of drops, the effects of collision-coalescence on the DSD increase moving down in the cloud (see Chapter 2). A cloud subject to both growth processes will exhibit DSDs showing a combination of features from both effects.

In this study, we assume cloud drops reach their maximum condensational growth size at cloud top, which we will term the characteristic drop size, D_c. We next assume that drops significantly larger than D_c found at cloud top are a result of the collision of drops of size D_c. Assuming no liquid water is lost in the coalescence process, the volume of a drop formed by i collisions is $V_i = (i+1)V_c$, where V_c is the volume of the characteristic drop. Because drops do not exist in discrete bin sizes, we relax our assumption and assign volumes within the range $(i+0.5)V_i$ and $(i+1.5)V_i$ to be products of i collisions. The drop diameter associated with the i^{th} collision, D_i, is then:

$$\left[\frac{6}{\pi}(i+0.5)V_c\right]^{\frac{1}{3}} < D_i < \left[\frac{6}{\pi}(i+1.5)V_c\right]^{\frac{1}{3}} \tag{4.2.1}$$

We will transform both DSD collected from *in-situ* instruments and those derived from a box model, described next, into collisional distributions, i.e. compute the concentration of drops that are the product of 1, 2, 3... collisions. By binning in this way, permits comparison of daily distributions which focuses on the collision process while also accounting for day-to-day variations in drop size. We will use these collision distributions to elucidate which processes are most important in governing collisional growth.

4.2.3 Collision Box Model

The evolution of a drop size distribution is computed using a stochastic collection box model described in *Bott* [1998][1]. This model is used to help interpret observations of cloud top size distributions in MSc clouds. The Hall collection kernel, a hydrodynamical-gravitational kernel, was used in simulating collisional drop growth given an initial drop distribution [*Hall*, 1980]. The kernel, K, describes the rate at which drops of size D_1 collide and coalesce with drops of size D_2:

$$K_{12} = \frac{\pi}{4}\left(D_1 + D_2\right)^2 u_{12} E_{12} \tag{4.2.2}$$

where E is the collection efficiency (dimensionless) for the drop pair in question and $u_{12} =\mid u_1 - u_2 \mid$ is the relative velocity between the drops. Collection efficiency has been experimentally determined [*Manton*, 1974; *Lin and Lee*, 1975] and is found to be a complex function of size because it incorporates processes such as wake capture, drop deflection, and drop rebound. See *Pruppacher and Klett* [1997] for more detailed discussion. For the Hall kernel, u_{12} is defined using the drop terminal sedimentation

[1] Available for free at http://www2.meteo.uni-bonn.de/forschung/gruppen/tgwww/people/abott/fortran/fortran_english.ht

velocity, i.e.

$$u_{12} = \mid w_{t1} - w_{t2} \mid \tag{4.2.3}$$

where w_t is the terminal velocity. At cloud drop sizes $D < 30$ µm, w_t is very small and thus the kernel predicts very slow collection rates. Only once one of the drops becomes substantially larger, $D \sim 50$ to 60 µm, does differential sedimentation become rapid.

Microphysical parameters which define the initial DSD for the box model are based on those typical of MSc and similar to those found in the observational data from the MASE, POST and VOCALS field campaigns (Sect. 4.2.1). These parameters are held constant throughout this study and are listed in Table 4.1. Running the model at various time increments showed no variability in calculated DSD for time increments $\Delta t <$ 1 s. To be conservative, we set $\Delta t = 0.1$ s. The initial drop concentration, $N_\circ$, was set at a typical MSc value, assuming clean cloud conditions, of 100 cm^{-3}. The initial DSD is defined using a lognormal size distribution with median drop size D_m and standard deviation σ. During MASE, σ ranged between 1.03 and 1.06, and therefore we set the initial DSD $\sigma = 1.05$. We chose to define the initial median diameter $D_m = 20.5$ µm because this is close to $\overline{D}_m$ observed during the MASE and POST field projects (Sect. 4.3.2). The VOCALS field project generally exhibited smaller drop sizes, which tends to reduce collision rates and hence should exhibit less collisional growth. With these parameters, the initial liquid water content (LWC) during the model runs is ~ 0.3 g m^{-3}, also a typical value for MSc.

Cloud Top Parameter	Symbol	Value
Time step	dt	0.1 s
Initial drop concentration	$N_\circ$	100 cm^{-3}
Initial geometric standard deviation of DSD	σ	1.05
Median drop diameter	D_m	20.5 µm
Truncation diameter	D_{trunc}	23.4 µm

Table 4.1: Constant prescribed model parameters

We convert DSDs to collisional distributions as described above (Sect. 4.2.2). This assumes that drops significantly larger than cloud top D_m are a result of the collision of drops with diameters equal to D_c, the characteristic drop size. Equation 4.2.1 defines drops as small as $D = \left[\frac{6}{\pi}(1.5)V_c\right]^{\frac{1}{3}}$ (i.e. the lower bound with $i = 1$) to be products of 1-collision events. In order to make sure that the pre-existing size distribution at collisional sizes did not prejudice the results, all drops which exceeded this diameter $D_{trunc} > \left[\frac{6}{\pi}(1.5)V_c\right]^{\frac{1}{3}}$ were removed from the initial DSD, i.e. the concentration of drops with $D > D_{trunc}$ was set to zero (as illustrated in the schematic shown in Fig. 4.1). For D_c= 20.5 µm, D_{trunc} = 23.4 µm. Thus, all drops that are found at collisional sizes must be formed by collisions of smaller drops.

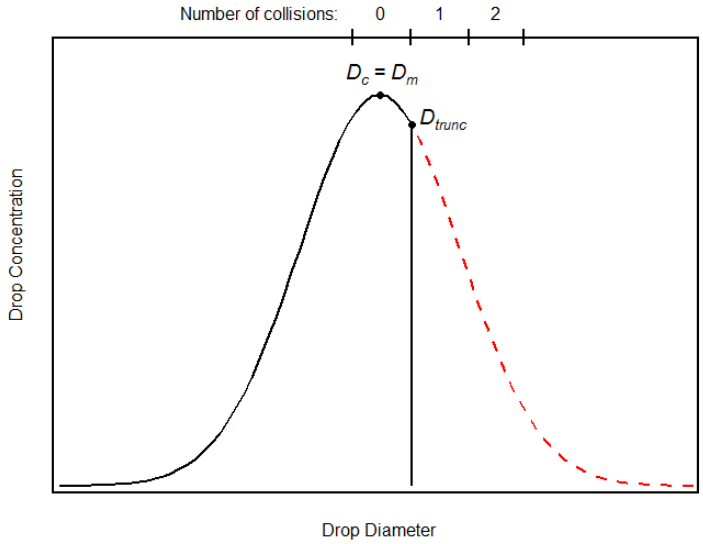

Figure 4.1: Schematic of model DSD truncation

Two optional modifications to the original model were made in order to emulate realistic CT environments. The first modification is intended to simulate turbulence effects on collisions. Longwave emission from CT leads to CT cooling, which generates negatively buoyant air that sinks, producing BL turbulence. Small-scale ($L < 1$ m), turbulence has been hypothesized to increase collision-coalescence rates and promote the

development of drizzle (see review by *Bartello et al.*, 2010). CT turbulence is therefore an important process to consider when attempting to simulate DSD growth from collision-coalescence. Turbulence was simulated in a highly simplified and idealized manner by modifying the relative velocity u_{12} from Eq. 4.2.2 such that:

$$u_{12} = \mid w_{t1} - w_{t2} \mid + v_{rel} \tag{4.2.4}$$

where a fixed relative velocity between drops, v_{rel}, is assumed to be added for all drops due to turbulent motions. This highly idealized model is used because it is simple and the results are easily interpretable. In order to represent effects such as drop acceleration, inertia and clustering, a more realistic model of turbulence effects on v_{rel}, which accounts for drop size, would be needed. A range of v_{rel} between 30 and 100 $\mathrm{cm\,s^{-1}}$ was used; the latter value is larger than realistic mean turbulent velocity fluctuations in stratocumulus environments.

Cloud Top Parameter	Symbol	Value
Drop relative velocity	v_{rel}	30, 60, 100 cm $\mathrm{s^{-1}}$
Cloud seed size	D_{seed}	25.8, 29.5 µm
Cloud seed concentration	N_{seed}	0.01, 0.1, and 1.0 $\mathrm{cm^{-3}}$
Residence time	τ_{res}	10, 30 min

Table 4.2: Varying prescribed model parameters

The second modification that was made to the original model adds large drops, termed "seeds" to the initial DSD. In stratocumulus, such seeds are thought to be generated by the recycling of large drops back to cloud top. Although Chapter 2 shows that this mechanism does not dominate the production of large drops at cloud top, it is plausible, and perhaps even inevitable, that a small number of such drops return to cloud top by turbulent diffusion after collisional growth through the cloud layer. These drops are often referred to as "seeds" or "lucky" drops because they develop independently

of the bulk drop population and have been shown to help promote drizzle production. Collision-coalescence increases rapidly with size and therefore the inclusion of even a small number of large drops may have substantial effects on collision-coalescence growth rates. We simulate lucky drops by seeding the initial DSD with drops $D_{seed} > D_{trunc}$. D_{seed} = 25.8 and 29.5 µm, which represent the mean sizes of 1- and 2-collision drops (given our assumption that D_c =20.5 µm), with concentrations N_{seed} = 0.01 cm^{-3}, 0.1 cm^{-3}, and 1.0 cm^{-3}. Cloud seeds were incorporated into the initial DSD after truncation. Finally, each box model was run for a period that varied between 10 and 30 min. Because simulations are meant to represent collision events at cloud top, residence times, τ_{res}, had to stay within realistic dwell times for air parcels at CT. Results from *Magaritz et al.* [2009] found CT dwell times reached peak values of ∼20 minutes. All parameters and their prescribed values, which varied between model runs, discussed here are listed in Table 2.

4.3 Results and Discussion

4.3.1 Number Distributions

We began our analysis of MASE clouds by comparing DSD from Days 14-17 (see Chapter 2). Figure 2.3 showed that day to day variations in the shapes of the DSD at CT and MC levels are very small. Only at CB are there clear signs that the low drizzle Days 14/16 were microphysically different from the high drizzle Days 15/17. A comprehensive study of the drizzle structure (through calculations of R, R probability distribution functions, R distributions, and the statistics associated with these calculations) followed and revealed differences in cloud properties between Days 14/16 and Days 15/17 apparent *at all levels* within the cloud. These calculations also lead to conclusions

regarding the drizzling nature of the MASE flights and, more generally, regarding the range of drizzle rates and the diversity in drizzle structure (vertical and horizontal) seen from day to day within MSc regimes. Days 14/16 were shown to exhibit well-developed drizzle, with moments of strong drizzle, while Days 15/17 were shown to exhibit more uniform, and much lighter drizzle.

With these conclusions in mind, we investigate the number distributions once again, but this time, with concentration plotted on a logarithmic scale, as shown in Figs. 4.2 and 4.3, in order to bring out details of the DSD at larger sizes. Insets show concentration plotted on a linear scale, like those in Chapter 2, for convenient comparison. Figure 4.2 shows daily DSD grouped by a) cloud top, b) mid-cloud, and c) cloud base (see Chapter 1 for a description of how flight levels are characterized). These figures reveal differences in the DSD not visible in the insets, the most obvious of which occur at $D > 30$ µm. In all three panels of Fig. 4.2, the heavy drizzle days (Days 14/16) and the light drizzle days (Days 15/17) exhibit clear differences in the concentration at large drop sizes. These differences are smallest at cloud top (Fig. 4.2a) and largest at cloud base (Fig. 4.2c). As discussed in Chapter 2 (and also above, Sect. 4.2.2), this implies that drizzle is initiated at, and at least partly controlled by, the CT region. Although it will be explored in greater detail below, one final observation which we note here is that the tail of the DSDs at large drop sizes appears to be well-represented by a straight line (when plotted on a log-log scale). Our main goal in this study is to better understand the cloud processes which determine the DSD at large drop sizes in order to elucidate the origin of drizzle in marine stratocumulus.

Figure 4.3 shows drop concentrations grouped by day, with CB, MC and CT distributions for each day on a single plot. On Day 14 (Fig. 4.3a), mode diameter increases moving upward in the cloud, indicative of growth that is primarily driven by condensation. At drop sizes much larger than the mode, however, concentrations increase moving downward in the cloud, indicative of drop growth by collision-coalescence of sedimenting

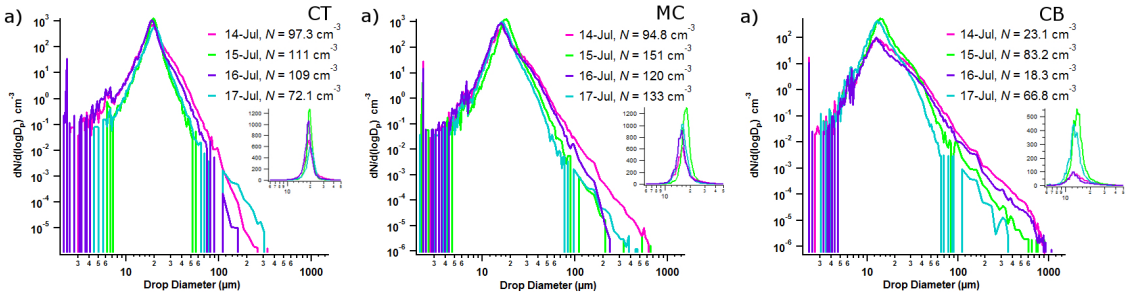

Figure 4.2: Daily DSD at each cloud level plotted on a logarithmic scale
Daily DSD at each cloud level plotted on a logarithmic scale, a) cloud top, b) mid-cloud, and c) cloud base, for MASE Days 14-17. Insets show identical DSD with concentration plotted on a linear scale as opposed to a logarithmic scale.

drops. Days 15 and 16 show a similar pattern, even though these days exhibit much less drizzle than Day 14 (Fig. 4.3b and 4.3c). All of these cases highlight the importance of both condensation and collision-coalescence for the evolution of drop populations. Day 17, which exhibits the least amount drizzle, appears different in that very little collisional growth through the cloud layer can be observed. While the CT DSD extends to 300 μm, indicating some amount of CT collisional growth, no further evidence for drop growth at the MC or CB levels is seen (Fig. 4.3d).

One prominent feature in Fig. 4.3 is the intersection of the CT, MC and CB size distributions. The "crossover" diameters are listed in Table 4.3, and represent the size at which the concentration of drops at one level exceeds the concentration of drops in another level. For example, on Day 14, the concentration of drops at MC is less than those at CT for $D < 38.6$ μm, and then exceeds that of CT for $D < 38.6$ μm. These diameters describe, very approximately, the characteristic drop size that sediments from one region (e.g. MC) into the next lower region (e.g. CB), all the while growing via collision-coalescence. The three days for which crossover sizes can be determined follow an expected pattern, with Day 14 (highest drizzle) showing the largest sizes at both transitions (CT to MC and MC to CB), and Day 15 (lowest drizzle) exhibiting the smallest crossover sizes. Because Day 17 shows no growth at lower cloud levels (the DSD from

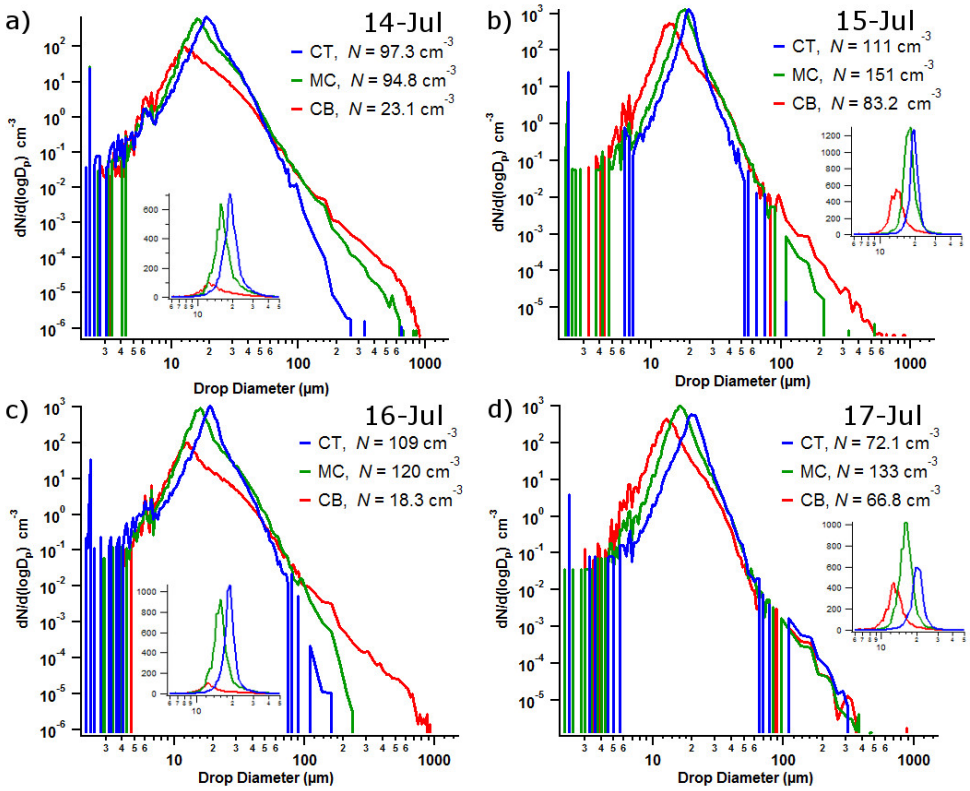

Figure 4.3: Level by level DSD plotted on a logarithmic scale
Level by level DSD plotted on a logarithmic scale on each MASE Day14-17, a) - d), respectively. Individual DSD are the same as those found in Fig. 4.2

each cloud level lies almost directly on top of one another) no crossover diameters are presented.

4.3.2 Collision Distributions

For each study day, combining Eq. 4.2.1 with the mode diameter D_c permits us to estimate the range of drop sizes which are products of individual collision events. In other words, in this section, we re-bin the drop size distribution into those drops that are the product of $i = 1$, 2, 3, etc. collisions, which we will term "collisional space". This is useful because it transforms size distributions into a framework where

	14-Jul	15-Jul	16-Jul	17-Jul
N_{MC} over N_{CT} (µm)	38.6	23.8	28.2	-
N_{CB} over N_{MC} (µm)	111	71.3	99.7	-

Table 4.3: Cloud top crossover diameters
Cloud top crossover diameters for MASE clouds, Day 14-17. Crossover diameters mark the location at which the concentration of drops at one level exceeds the concentration of drops at another level.

comparisons can be made among different days, independent of changes in, e.g., mode diameter caused by differences in cloud depth or CCN concentration. The fact that cloud top DSDs are observed to be narrow (for MASE, $1.02 < \sigma_g < 1.06$), consistent with pure condensational growth, means that binning the drops into collisional space is a reasonable way to transform the data. Figure 4.4 shows 31 cloud top size distributions across all three field projects (MASE, POST and VOCALS) from which D_c values were determined. The mean across all projects is $\bar{D}_c = 18.2 \pm 5.41$ µm, ranging between 9.9 and 28.2 µm. DSDs show an inverse relationship between D_c and mode height, consistent with drop concentrations being controlled by aerosol. The sixteen POST DSD, shown in black, exhibit a large range of D_c ($\bar{D}_{c,POST} = 20.4 \pm 4.84$ µm). The MASE clouds (Days 14-17, plus two additional days in which CT data was available) are shown in red and are centered within POST data. Aside from the DSD to the far right, MASE D_c are relatively constant ($\bar{D}_{c,MASE} = 19.8 \pm 0.938$ µm) and exhibit narrower distributions compared to POST clouds. VOCALS clouds also show low variability in D_c but at much smaller drop sizes compared to POST and MASE ($\bar{D}_{c,VOCALS} = 12.3 \pm 1.63$ µm). All of the distributions shown in Fig. 4.4 exhibit significant contribution to concentration at drop sizes larger than D_c, regardless of the size of D_c. The addition of POST and VOCALS data adds a range of DSD height, width and D_c which was not available using MASE days alone. This diversity will contribute to the relevance of our results to a

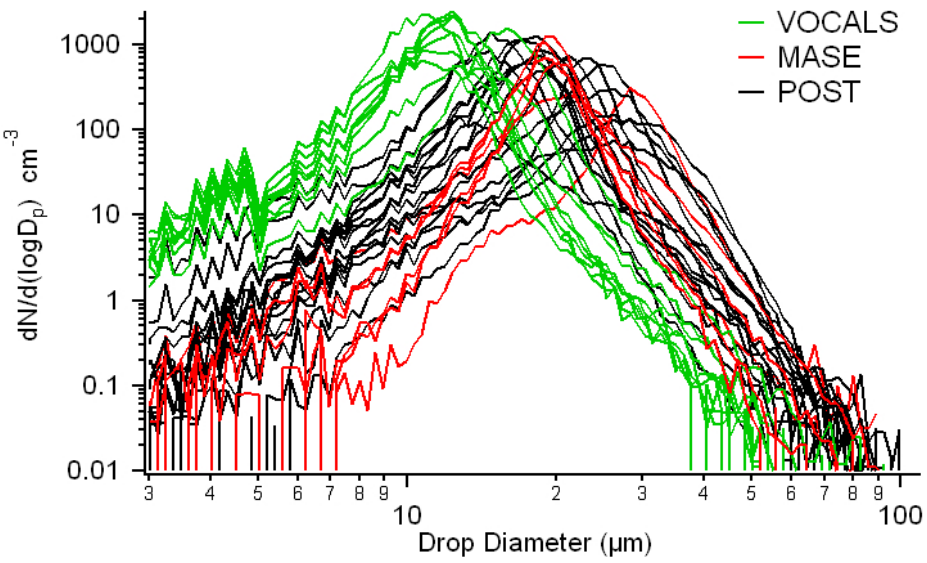

Figure 4.4: F-PDI measured cloud top DSD
F-PDI derived cloud top DSD for all available data from 3 MSc field projects: VOCALS (green), MASE (red) and POST (black).

broad range of MSc conditions.

Figure 4.5 shows all 31 of the collisional number distributions. In general, the distributions become noisier at $\sim 8-10$ collisions owing to the poor counting statistics for rare, large drops. For this reason, we only show the curves up to 8 collisions. All fits are also limited to data between 1 and 8 collisions. Drop concentrations follow a power law:

$$C(k) = bk^{-m} \tag{4.3.1}$$

where C is the concentration of drops that have formed from k collisions, b is a constant and $m = 3.04 \pm 0.39$ for all available data (Fig. 4.5). The slope m represents the extent to which collisional growth produces drop sizes larger than D_c. Drops which are the product of a large number of collisions appear at greater concentrations within a well-developed CT, thus flattening the slope. A small m, then, corresponds with stronger drizzle. For familiarity, we compare m from the four MASE days, whose collision curves

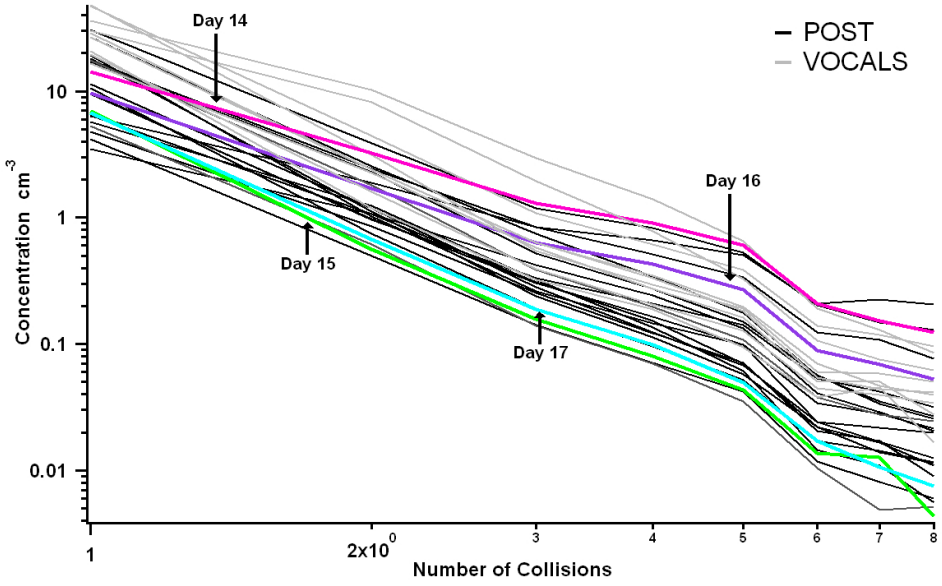

Figure 4.5: Observed collision number distributions
Collision number distributions for all available data from 3 MSc field projects: VOCALS (gray) and POST (black), and with MASE Days 14-17 highlighted for easy comparison.

are highlighted in Fig. 4.5. m for Days 14/16, the two well-developed clouds, are 2.29 and 2.50, respectively, while m for Days 15/17, the two less-developed clouds, are 3.37 and 3.26, respectively. Days 14-17 are unique in the fact that the daily D_c are nearly identical (again, $\bar{D}_{c,MASE} = 19.8 \pm 0.938$ µm). We note that low m values do not necessarily imply high drizzle rates. For cloud tops characterized by small D_c, such as most of the VOCALS data, a low m value only implies that substantial collisional growth has occurred even if the drops that are produced are not very large and hence ineffective at sedimenting. Because the processes that govern collisional growth are our main focus, these data are still useful and of interest to us.

Daily m was compared to other daily cloud properties in a hope to reveal a relationship between m and other cloud properties which have previously been linked to cloud development. These properties include: R; D_c; b; N; cloud top LWC; cloud thickness, H; vertical velocity variance,$(w')^2$ (not available for MASE); and the CT jump in both

total water mixing ratio, Δq_T, and equivalent potential temperature, $\Delta\theta_e$. No significant correlation was found between m and any of these properties (not shown). This result does not suggest m is independent of these cloud properties; it could imply that m is dependent on several cloud properties which may affect CT collision rates simultaneously, and thus the correlation with any single variable does not easily reveal this relationship. Given that our observations yield no further clues into what governs collisional growth, i.e. m, we will below (Sect. 4.3.4) turn to a box model where CT properties can be varied both independently and in conjunction with one another.

4.3.3 Power Law Relationship

As discussed above, plotting the number distributions in log-log space (Fig. 4.4) strongly suggests a power-law relationship in the data at drop sizes larger than the mode size. When transformed to collisional space (Fig. 4.5) and focusing on the first eight collisions this relationship becomes quite clear. The high correlation coefficient values ($\overline{R^2} = 0.987 \pm 0.008$) for the power-law fits lend further credence to this notion. We note that if the drop size distribution follows a power-law:

$$C(D) = aD^{-p} \tag{4.3.2}$$

where C is concentration, a is a constant and D is diameter, then it follows that a power-law will also be found in collisional space since $D_k^3 = kD_c^3$ or $D_k = k^{1/3}D_c$ where k is the number of collisions, which, after substituting yields:

$$C(k) = aD_c k^{-p/3} = bk^{-m} \tag{4.3.3}$$

which is the same as Eq. 4.3.1.

Previous studies have suggested other kinds of fits for drop size distributions that are

not power-law relationships at large drop sizes. For example, a lognormal distribution that is often used for cloud drops will fall off more quickly than a power-law distribution. The Marshall-Palmer distribution for rain drops [*Marshall and Palmer*, 1948] decreases exponentially rather than as a power-law and is appropriate for drop sizes in the millimeter size range, which is an entirely different size range from the $D < 60$ µm range considered here.

We suggest that the interpretation of a power-law relationship is consistent with known mechanisms for producing such relationships, in particular a mechanism called "preferential attachment" [*Newman*, 2005]. One example of this mechanism is the observed power-law relationship for the number of cities as a function of population. Larger cities attract more people than small cities (i.e. people are preferentially attracted to larger cities), and the result of this process is a power-law distribution of city sizes [*Newman*, 2005]. This process has also been described as the "rich get richer" scenario.

For collision-coalescence, preferential attachment has a satisfying interpretation: collisionally-produced drops of size $D_k > D_c$ are better able to compete for the population of condensationally-formed drops of size D_c, as shown in Eq. 4.2.2. If drop velocity is independent of diameter, then the collision rate increases as D_k increases because the collision cross-section increases, which describes the conditions for the preferential attachment mechanism. If we further assume that the relative velocity is due to the difference in sedimentation velocity (as per the Hall kernel), then $u \sim D^2$ for drops in the size of interest here, which makes the "rich" ones grow "richer" much faster, which still satisfies the conditions for a power-law relationship.

We observe this power-law relationship in a limited size range due to the limits of sampling during each flight. It would be of great interest to understand the full size range for which this distribution is valid. Panels a and c in Fig. 4.3 certainly suggest that this relationship holds for quite a wide range of drop sizes, perhaps as high as 1 mm. If true, this would make sense since there are few other processes within the

cloud that will affect drop sizes. Entrainment of sub-saturated air is one such process, but otherwise for stratocumulus, it would require that either (i) the drops to become large enough to experience drop breakup ($\sim$ 5 mm), which does not occur or (ii) hydrometeor self-collection becomes significant, which is unlikely given extremely low rain rates for even the strongest drizzling clouds. Thus, collisional growth is most likely the primary governing process of the DSD at large sizes within Sc layers.

4.3.4 Box model simulations

Having reached the limit of what observations can tell us about the processes that control the collisional distribution (i.e. the power-law slope, m), we turn to using the idealized stochastic collection model described in Sect 4.2.3. The goal is to (1) determine if we can generate simulated power-law drop size distributions that resemble observed ones, and what parameters would be required to do so; and (2) determine what controls the variability of m. Note that observed m is derived from the mean of the DSD over a horizontal distance of $\sim$ 30 km, which clearly is not well-represented as a box. Hence, the box model is meant to represent the mean behavior of this layer and thus we will utilize mean properties. One disadvantage of this method is that averaging over a number of simulations with variability in properties such as mean drop size and concentration may not produce the same result as one simulation using the mean of these properties since collision-coalescence is not a linear process. It might be that the results for a ensemble of simulations would be different.

The input parameters which define the shape of initial DSD are presented in Table 4.1. We begin by performing the most basic simulation, using the Hall kernel without any additional "turbulence" (so $v_{rel} = 0$ cm s^{-1}) and no seed drops. The collision distribution for this run is shown in orange at the bottom of Fig. 4.6, which is plotted in the same manner as Fig. 4.5. Two collision curves are shown for each model run, one with the

model integration (or residence) time $\tau_{res} = 10$ min, represented by a broken line, and one with $\tau_{res} = 30$ min, represented by a solid line. The two black dashed lines at the top of the figure show the range of slopes derived from observed DSD, representing $m_{ref} = 2.5$ and 3.5. These reference lines allow for easy comparison between the slopes of the model's collision curves to those which fall within the range of values produced by observations. Comparing both orange lines to the reference lines, it is clear that the slope of the collision curves do not fall within the range of observed m . In fact, m is much higher than m_{ref}, reflecting a DSD which falls off quickly at $D > D_c$.

Comparing the orange collision curve in Fig. 4.6 to the observed collision curves in Fig. 4.5 reveals that the concentration of 1-collision drops, b, is significantly lower for the model than that for the observed data. The low b is a result our imposed truncation of the DSD, which assumes no 1-collion-size drops exist, before collisions are allowed. While the relative changes in b between model runs is interesting, the low concentration of 1-collision drops is a function of model design, is not a source of concern, and should not be compared to observed b. Although the extra 20 minutes of growth time between the dashed and solid lines increased the concentration of drops formed by collision, it did not alter the slope of the line, reflecting little development of the CT DSD between 10 and 30 min. The most important conclusion which can be made from these observations is that the base simulation cannot produce collision curves comparable to observed collision curves. This conclusion motivated our next set of studies in which prescribed turbulence, in varying quantities, was added.

4.3.4.1 Simulations with turbulence

Figure 4.6 shows 3 additional pairs of lines where simulated turbulence, in the form of a relative velocity difference between drops, v_{rel}, was added to the model, the extent to which varied between model runs (30 cm s^{-1}, 60 cm s^{-1} and 100 cm s^{-1}). A typical

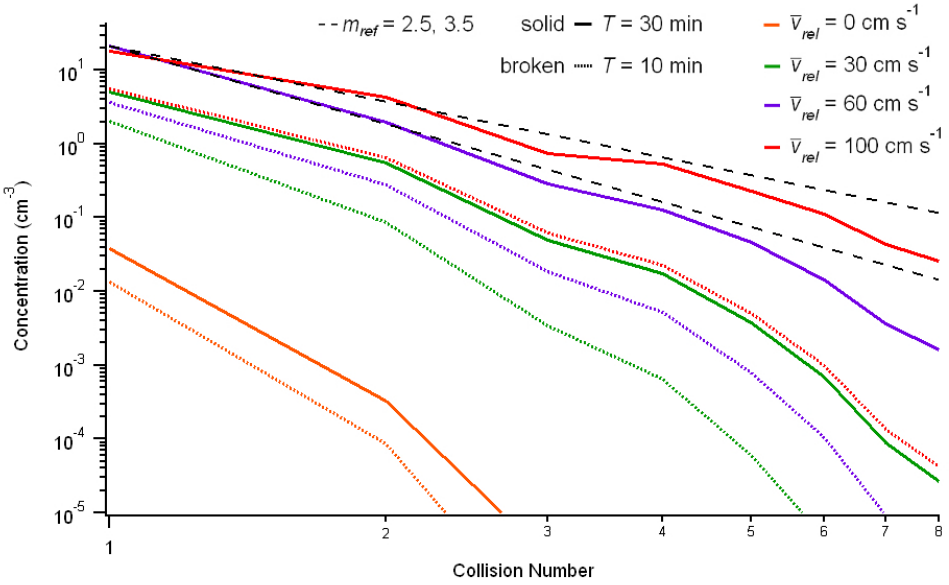

Figure 4.6: Model-derived collision number distributions
Collision curves derived from model DSD. Results are shown for varying prescribed turbulence (line color) and residence time (line style). Two reference curves are also plotted with m_{ref} = 2.5 and 3.5, the range of m exhibited during MASE, POST, and VOCALS.

turbulent velocity might be $\sim$ 50 cm s^{-1}, so the first two values are within a plausible range, with the last being somewhat higher than realistic. These simulations show that m decreases as the relative velocity between the drops increases (the slopes decrease from orange to red, moving up on the plot). That is, the development of CT DSD from collisional growth increases as collision rates are accelerated with greater amounts of "turbulence," which is expected. Second, m decreases from τ_{res}= 10 min to τ_{res} = 30 min at all prescribed v_{rel}, which also was expected but was not apparent in the no turbulence collision curves. Thus, both the kernel and the residence time are effective at changing m. Surprisingly, only one collision curve falls within the range of m values derived from observed DSD. This collision curve was produced from the model run in which v_{rel} and τ_{res} were highest (red, solid line; m = 3.01), meaning the model can only produce collision curves comparable to those observed if the drop environment is

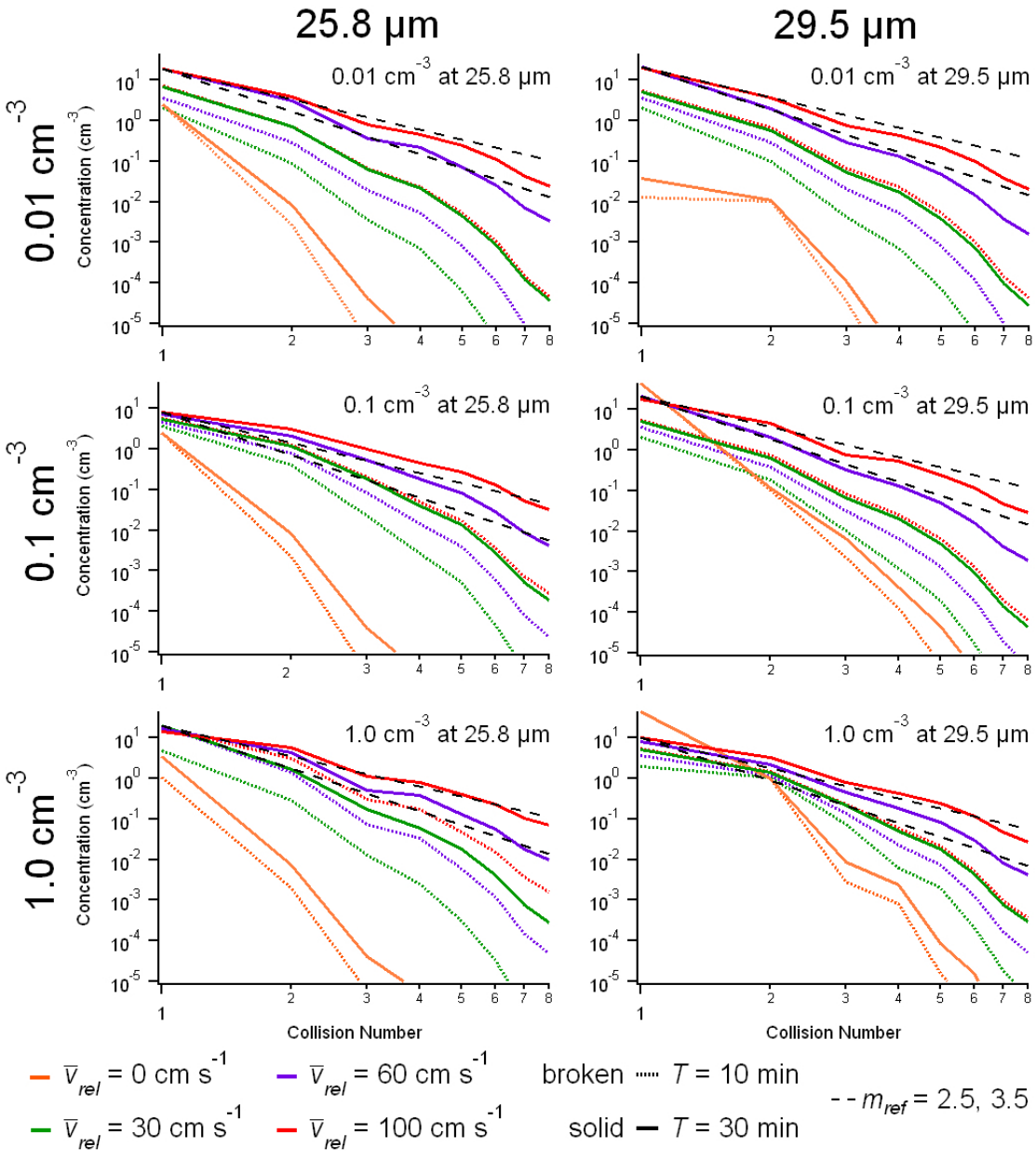

Figure 4.7: Model-derived collision number distributions with seeds
Collision curves varying seed size (D_{seed} = 25.8 µm and D_{seed} = 29.5 µm, left to right) and seed concentrations (N_{seed} = 0.01 cm^{-3} , N_{seed} = 0.1 cm^{-3} , and N_{seed} = 1.0 cm^{-3}, top to bottom). Prescribed turbulence and run-times vary in the same manner as Fig. 4.6, with line color and style changing accordingly. Again, reference curves are plotted along with model run data.

turbulent *and* if CT air parcel dwell times are large, both of which are most likely larger than is realistic in stratocumulus. While this is an improvement to the results found previously (where $v_{rel} = 0$ cm s^{-1}), it is unlikely that in the mean air parcels reside at cloud top for 30 min and exhibit such turbulent conditions.

4.3.4.2 Simulations with seed drops

Figure 4.7 shows the results of adding cloud seeds, drops which are larger than the truncation diameter, to our initial truncated size distribution. The specifics of the graph are identical to those found in Fig. 4.6, with line types and line colors representing differences in v_{rel} and τ_{res}. Starting seed size and concentration vary between each plot. Cloud seeds were added at 2 sizes, 25.8 and 29.5 µm (representing 1- and 2-collision sized drops, respectively), and 3 different concentrations, 0.01, 0.1, and 1.0 cm^{-3}. These concentrations are chosen to be small because they are intended to reflect drops that are grown collisionally, and while sedimenting are transported back to cloud top through turbulent diffusion. We know (Chapter 2) that such recycling is not a strong process, and thus we have selected relatively concentrations to reflect this prior observation.

Examining the changes along a single column in Fig. 4.7 shows the response of the DSD to increases in seed concentration while seed size remains constant. The response of m in both columns is the same: increasing N_{seed} causes m to decrease. This is true regardless of prescribed turbulence and air parcel residence times. Moving from left to right within each row shows the response of the DSD to increases in seed sizes while seed concentration remains constant. The response of m to changing the seed size is very small and, in some cases, caused m to even *increase* slightly. We believe this is an effect of drop binning within the model and has little to do with simulated cloud dynamics. While increasing D_{seed} had a small affect on m, it had a large affect on the concentration of drops at small v_{rel}. Increasing D_{seed} causes the concentrations of drops formed from

each collision event to increase as well, causing the collision curves to move up in the plot. This effect is easy discernible when considering the area between the lowest curve (v_{rel} = 0 cm s^{-1}, τ_{res}= 10 min; orange, broken line) and the highest curve (v_{rel} = 100 cm s^{-1}, τ_{res}= 30 min; solid, red line). This area decreases moving left to right, within each row. This affect is also apparent moving down each column (as N_{seed} increases) although the strength of this effect is greatest from left to right (as D_{seed} increases).

D_{seed} = 25.8 µm			D_{seed} = 29.5 µm		
	N_{seed} (cm^{-3})	m		N_{seed} (cm^{-3})	m
v_{rel} = 100 cm s^{-1}	0.01	3.03	v_{rel} = 100 cm s^{-1}	0.01	3.11
	0.1	2.52		0.1	2.97
	1.0	2.49		1.0	2.69
v_{rel} = 60 cm s^{-1}	0.1	3.35	v_{rel} = 60 cm s^{-1}	1.0	3.42

Table 4.4: Seeding parameters and slopes
Seeding parameters which lead to m within the range of observed m; τ_{res} = 30 min.

One goal in running the simulations found in Fig. 4.7 was to find a range of prescribed model parameters which produce slopes similar to those in the range of observed m. The summary of all of the simulation conditions that generate slopes in the observed range of m between 2.5 and 3.5 are shown in Table 4.4. The model can produce collision curves comparable to those observed only if the drop environment is turbulent (v_{rel} = 100 cm s^{-1}) and if drop CT dwell times are large (τ_{res}= 30 min). The required turbulence can be reduced to v_{rel} = 60 cm s^{-1} only if cloud seeds are added at concentrations of 0.1 cm^{-3} or greater. While this is expands the parameter space relative to the results found in Fig. 4.6, in which no seeds were added, it still requires simulations which push the limits of reality regarding CT dwell times and turbulence. Thus, we believe turbulence, dwell times, and cloud seeds, which in reality represent large drops that are return to cloud top after having grown through collisions, play an important role in increasing collision

rates at CT. However, we also find that the model is limited in its ability to simulate CT drop development based on a lack of realistic parameter space which can generate simulated DSDs that resemble those that are observed. One possibility is that a box model is a poor method to simulate a turbulent cloud environment, and that processes associated with turbulence, such as random fluctuations in concentration and mixing of different air parcels, play an important role. Addressing this question would require a substantially more complex model, such as large eddy simulation, which could be a fruitful next step in addressing the questions we have posed here.

4.4 Conclusions

This study synthesizes the results from the Artium Flight PhaseDoppler Interferometer comprising 31 flights during three different stratocumulus field projects in order to examine the drop size distribution near cloud top, and, in particular, study the large drops formed by collision-coalescence. We focus on cloud top because this is the location where drizzle is observed to be initiated, and because we previously found (in Chapter 2) that high and low drizzle days are microphysically distinct in this region. Based on flight observations, we found the following:

- Drop size distributions appear to follow a power-law relationship at drop sizes larger than the mode diameter. This relationship appears to fit the data very well on the four MASE days (Days 14-17) for drops between 20 and ~500 µm diameter (Fig. 4.3).
- When transformed into collisional space, this power-law is retained, as theory predicts. For the drops formed by between 1 and 8 collisions, the power-law fit over all 31 flights yields $\overline{R^2} = 0.987 \pm 0.008$.

- We suggest that this observation can be explained by the "preferential attachment" mechanism which is known to generate power-law distributions. In this scenario, drops that are larger will collide and thereby grow more rapidly than smaller drops, which satisfies the conditions for this mechanism.

- The observed slope m of the power-law (Eq. 4.3.1) for the collision distribution varies between approximately 2.5 and 3.5.

- Attempts to find correlations of m with mean stratocumulus layer properties (R, D_c, b, N, CT LWC, H, $(w')^2$, Δq_T, $\Delta\theta_e$) all failed. This may imply that m either does not depend on these parameters at all, which we deem unlikely, or that it depends on these parameters in a complex fashion that will require more analysis to understand.

Because we did not find any way to predict m from other observational data, we turned to a box model simulation of stochastic collection in order to help understand what causes m to vary. The simulation uses only the Hall kernel, and is initialized with drop distributions typical of MASE conditions. The model is modified in three important ways: (i) distributions are truncated so that the concentration of drops in the collisionally-formed size range is initially zero; (ii) the option to increase the relative velocity v_{rel} between all drops by a constant amount was added in order to represent the effect of turbulence in a highly simplified manner; and (iii) the option to "seed" the distribution with drops larger than the truncation size was added to help accelerate collisional growth. By running this box model, we found that:

- Without any modifications, simulated m is much larger (steeper) even if the drops in the air parcel are allowed to collide for 30 mins. Thus, the Hall kernel by itself is incapable of explaining the observed drop distributions.

- Adding a large amount of idealized turbulence, $v_{rel} = 100$ cm s^{-1} does accelerate collisional growth, and allowing the box model to run for 30 mins can generate m in the observational range. However, both of these conditions are most likely beyond realistic bounds for clouds.

- Adding seeds does accelerate collisional growth, but to produce m values in the range of strongly drizzling clouds ($m \sim 2.5$) still requires the unrealistic parameters $v_{rel} = 100$ cm s^{-1} and a 30 min integration of the model.

Overall, the simulations do come close to being successful at explaining the observations (Table 4.4) but fall somewhat short. As a result, a physically reasonable explanation for the observed cloud top drop size distributions in the range of low to high drizzling clouds remains elusive. Perhaps in addition to turbulence and recycling of large drops, processes not represented in the box model are also necessary ingredients to form drizzle in stratocumulus. Nevertheless, the observed distributions of large drops, including the power-law distribution, can serve as good constraints for more sophisticated models used to simulate the stratocumulus-topped marine boundary layer.

Chapter 5

Summary

The research presented in this dissertation has successfully resulted in a quantitative analysis of the relationship between marine stratocumulus (MSc) clouds and the water and energy budgets of the marine boundary layer (MBL). The impact of the MSc cloud regime on regional and global climates cannot be overstated. MSc are one of the main features of the Earth's atmosphere, effectively cooling the planet more than any other forcing (one scientist even refers to MSc as "climate refrigerators"). While the importance of MSc is acknowledged, they remain one of the hardest clouds for climate models to simulate. While their persistence and ubiquity may suggest simplicity, the processes which govern their dynamics are extremely complex, so complex they are difficult to parameterize. This research investigated several of these processes, including: sub-cloud evaporation, turbulence, entrainment, and cloud top (CT) radiative cooling, all with respect to drizzle.

Aircraft measurements used in this study come from *in situ* observations taken from a combination of instruments onboard the Center for Interdisciplinary Remotely-Piloted Aircraft Studies (CIRPAS) Twin Otter during the MArine Stratus/Stratocumulus Experiment (MASE) in July 2005. The flights specifically targeted MSc off the coast of California in the vicinity of Monterey, CA during the month in which the stratocumulus

is at its maximum. The goal of MASE was to study the interaction between aerosol and clouds using state-of-the-art instrumentation within one of the world's most persistent stratocumulus decks.

This research utilizes an Artium Flight Phase Doppler Interferometer (F-PDI) probe to derive high rate size distributions of drop population. One of the advantages of the F-PDI relative to other instruments is its accurate cloud drop size distribution measurements across a wide range of sizes, 2 to 100 µm diameter. Traditionally, the upper portion of this size range, ∼30 to 100 µm, has been difficult to measure well, and it is of particular importance to the initiation and evolution of drizzle. One of the main benefits of this research is the measurable drop size range of the F-PDI. All of the work presented here makes advancements to the field of cloud microphysics for this reason alone; much of the research performed would not have been possible, or possible to the extent of the accuracy we present, without the use of the F-PDI. To capture the whole range of drop sizes important for drizzle, which can reach up $D = 1$ mm in MASE clouds, drop size measurements from the Cloud Imaging Probe (CIP) are merged with those from the F-PDI.

Drizzle statistics in Chapter 2 indicate two microphysical regimes existed between the four MASE days, a high drizzle regime and a low drizzle regime. High drizzle regimes were found to be associated with patches of heavy drizzle, occurring in clusters with a typical length scale of 1 to 10 km, and exhibiting variability in R at all levels in the cloud. This was in contrast to light drizzle regimes, which were associated with more uniform, light-to-no drizzle. The presence of a small fraction of large, collisionally-formed drops at cloud top appeared to be a very strong indicator of how drizzle will develop through the cloud. We showed that drop growth can not be explained by simple gravitational sedimenation of the largest cloud top (CT) drops and suggested other mechanisms for growth, such as turbulence. The predictability of the structure (vertical and horizontal) and variability of drizzle may lead to further developments in distinguishing how other

key microphysical processes control Sc evolution. Furthermore, because these processes, including drizzle, control cloud properties, the findings described in Chapter 2 made advancements towards understanding the interaction between Sc and the larger climate system.

In Chapter 3, we derived sub-cloud evaporation rates from drizzle calculations at cloud base (CB). The observations indicate a large range of BL cooling exists between our study days. Sub-cloud profiles of evaporative cooling show characteristic distributions, with variability in both peak magnitude and width. We showed this variability corresponds to variations in the shape of the drizzle rate distributions. Variability was also found to exist in the horizontal, with implications for MBL turbulent kinetic energy. We utilized the concept of available potential energy (APE) to estimate the energy flux associated with evaporation and showed it makes up a large portion of the radiative flux driving the MBL (1-50%). Although a number of assumptions were made in this study, given the broad range of data presented, our results in Chapter 3 demonstrate that evaporation plays a large role in MBL dynamics and cloud lifetime, and thus the global climate system.

In Chapter 4 we utilized DSD measured from *in situ* aircraft instruments and derived from box model simulations to calculate CT collision rates in MSc. We found the collision rates derived from observations follow a power law. The observed slope, m, varied between 2.5 and 3.5, for a well-developed and a less-developed CT, respectively. Attempts to correlate m with other cloud properties failed, prompting the calculation of collision rates using DSD from box model simulations. While model results suggest collision rates are closely linked to properties such as turbulence, cloud seeds, and cloud drop residence time, it was insufficient to produce observed CT collision rates. The results of Chapter 4 suggested that a box model does not represent cloud top properties well. Nevertheless, observational results can serve as good constraints for more sophisticated model development, particularly at CT and for the entire MSc regime.

In a more general sense, the results of this dissertation emphasize the importance of accurately quantifying drizzle in MSc, a statement that is supported by previous work [*Nicholls*, 1984; *Austin et al.*, 1995; *Bretherton et al.*, 1995; *Duynkerke et al.*, 1995; *Frisch et al.*, 1995; *Boers et al.*, 1996; *Vali et al.*, 1998; *vanZanten et al.*, 2005]. Drizzle properties are observed to span a wide range, even over short time and spatial scales, implying that the impact of drizzle on the MBL can vary significantly. We suggest that further investigations of the effect of turbulence on collision-coalescence in stratocumulus are needed to improve quantitative understanding of drizzle in this regime. We also suggest a more detailed model of cloud top processes be used to better understand the formation of drizzle in MSc.

Nomenclature

α	Albedo
θ	Potential temperature (K)
θ_e	Equivalent potential temperature (K)
θ_v	Virtual potential temperature (K)
σ	Model initial standard deviation of DSD
τ_{res}	Model residence time (s)
w_T	Terminal velocity (m/s)
$(w')^2$	Vertical velocity variance
b	Concentration of 1-collision drops (cm^{-3})
C	Concentration of collisionally formed drops (cm^{-3})
D	Drop diameter (µm)
D_c	Characteristic drop diameter (µm)
D_k	Drop diameter of collisionally-formed drop (µm)
D_m	Model median drop diameter (µm)
D_{trun}	Model truncation drop diameter (µm)
D_{seed}	Model cloud drop seed diameter (µm)
D_{10}	10th percentile diameter of the drizzle distribution (µm)
D_{50}	50th percentile diameter of the drizzle distribution (µm)
D_{90}	90th percentile diameter of the drizzle distribution (µm)

E	Collection efficiency
H	Cloud thickness (m)
K	Kernel
k	Number of collisions
LWC	Liquid water content (g/m^3)
N	Cloud drop number concentration (cm^{-3})
$N_\circ$	Model initial cloud drop number concentration (cm^{-3})
N_a	Sub-cloud aerosol concentration (cm^{-3})
N_{seed}	Model cloud seed concentration (cm^{-3})
m	Slope
m_{ref}	Reference line slopes
q	Mixing ratio
q_L	Liquid water mixing ratio
q_T	Total water mixing ratio
R	Drizzle rate (mm/day)
R_{40}	Drizzle rate only including drop diameters $>$ 40 µm (mm/day)
$\overline{R}_{1\sigma}$	Mean drizzle rate over one standard deviation (mm/day)
T	Time (s)
dt	Model time step (s)
u	Drop velocity (m/s)
v	Vertical velocity (m/s)
v_{rel}	Model drop relative velocity (cm/s)
V_c	Characteristic drop volume (µm^{-3})
dv/dz	Shear strength (s^{-1})
z	Altitude (m)

Distribution Statistics Nomenclature

$D_{m,DSD}$	Mode diameter of the DSD (µm)
$\sigma_{g,DSD}$	Geometric standard deviation of the DSD
σ_R	Standard deviation of the drizzle rate
$D_{m,R}$	Mode diameter of the drizzle rate distribution (µm)
$\sigma_{g,R}$	Geometric standard deviation of the drizzle rate distribution
$D_{g,D50}$	Geometric mean of the PDF of D_{50} (µm)
$\sigma_{g,D50}$	Geometric standard deviation of the PDF of D_{50}
$D_{g,D90}$	Geometric mean of the PDF of D_{90} (µm)
$\sigma_{g,D50}$	Geometric standard deviation of the PDF of D_{90}

Bibliography

Ackerman, A. S., et al., Large-eddy simulations of a drizzling, stratocumulus-topped marine boundary layer rid d-2144-2009, *Monthly Weather Review*, *137*(3), 1083–1110, doi:10.1175/2008MWR2582.1, 2009.

Albrecht, B., Aerosols, cloud microphysics, and fractional cloudiness, *Science*, *245*(4923), 1227–1230, 1989.

Austin, P., Y. Wang, R. Pincus, and V. Kujala, Precipitation in stratocumulus clouds - observational and modeling results, *J Atmos Sci*, *52*(13), 2329–2352, 1995.

Bachalo, W., Method for measuring the size and velocity of spheres by dual-beam light-scatter interferometry, *Appl. Optics*, *19*, 363–370, 1980.

Bachalo, W., and M. Houser, Phase doppler spray analyzer for simultaneous measurements of drop size and velocity distributions, *Opt. Eng.*, *23*, 583–590, 1984.

Baker, M., R. Corbin, and J. Latham, The influence of entrainment on the evolution of cloud droplet spectra .1. a model of inhomogeneous mixing, *Quarterly Journal of the Royal Meteorological Society*, *106*(449), 581–598, 1980.

Bartello, P., B. J. Devenish, J. D. Haigh, and J. C. Vassilicos, Clouds and turbulence, *Bulletin of the American Meteorological Society*, *91*(8), 1087–1089, doi: 10.1175/2010BAMS2940.1, 2010.

Boers, R., J. Jensen, P. Krummel, and H. Gerber, Microphysical and short-wave radiative structure of wintertime stratocumulus clouds over the southern ocean, *Q J Roy Meteor Soc*, *122*(534, Part B), 1307–1339, 1996.

Bony, S., and J. Dufresne, Marine boundary layer clouds at the heart of tropical cloud feedback uncertainties in climate models, *Geophys. Res. Lett.*, *32*(20), doi: 10.1029/2005GL023851, 2005.

Bony, S., et al., How well do we understand and evaluate climate change feedback processes? rid b-5782-2008 rid e-6113-2011, *Journal of Climate*, *19*(15), 3445–3482, doi:10.1175/JCLI3819.1, 2006.

Bott, A., A flux method for the numerical solution of the stochastic collection equation, *Journal of the Atmospheric Sciences*, *55*(13), 2284–2293, 1998.

Bowen, E., The formation of rain by coalescence, *Aust. J. Sci. Res. Ser. A*, *3*, 193–213, 1950.

Bretherton, C., P. Austin, and S. Siems, Cloudiness and marine boundary-layer dynamics in the astex lagrangian experiments .2. cloudiness, drizzle, surface fluxes, and entrainment, *J Atmos Sci*, *52*(16), 2724–2735, 1995.

Bretherton, C., T. Uttal, C. Fairall, S. Yuter, R. Weller, D. Baumgardner, K. Comstock, R. Wood, and G. Raga, The epic 2001 stratocumulus study, *B Am Meteorol Soc*, *85*(7), 967+, doi:10.1175/BAMS-85-7-967, 2004.

Bretherton, C. S., P. N. Blossey, and J. Uchida, Cloud droplet sedimentation, entrainment efficiency, and subtropical stratocumulus albedo, *Geophys Res Lett*, *34*(3), doi: 10.1029/2006GL027648, 2007.

Brost, R., J. Wyngaard, and D. Lenschow, Marine stratocumulus layers 2. turbulence budgets, *J Atmos Sci*, *39*(4), 818–836, 1982.

Charlson, R., S. Schwartz, J. Hales, R. Cess, J. Coakley, J. Hansen, and D. Hofmann, Climate forcing by anthropogenic aerosols, *Science*, *255*(5043), 423–430, 1992.

Chuang, P., E. Saw, J. Small, R. Shaw, C. Sipperley, G. Payne, and W. Bachalo, Airborne phase doppler interferometry for cloud microphysical measurements, *Aerosol Sci. Tech.*, *42*, 685–703, 2008.

Comstock, K., R. Wood, S. Yuter, and C. Bretherton, Reflectivity and rain rate in and below drizzling stratocumulus, *Quart. J. R. Met. Soc.*, *130*, 2891–2918, 2004.

Comstock, K. K., C. Bretherton, and Y. S.E., Mesoscale variability and drizzle in southeast pacific stratocumulus, *J Atmos Sci*, *62*, 3792–3807, 2005.

Comstock, K. K., S. E. Yuter, R. Wood, and C. S. Bretherton, The three-dimensional structure and kinematics of drizzling stratocumulus, *Monthly Weather Review*, *135*(11), 3767–3784, doi:10.1175/2007MWR1944.1, 2007.

Cooper, W. A., Effects of variable droplet growth histories on droplet size distributions .1. theory, *Journal of the Atmospheric Sciences*, *46*(10), 1301–1311, doi:10.1175/1520-0469(1989)046<1301:EOVDGH>2.0.CO;2, 1989.

Cronin, M. F., N. A. Bond, C. W. Fairall, and R. A. Weller, Surface cloud forcing in the east pacific stratus deck/cold tongue/itcz complex, *Journal of Climate*, *19*(3), 392–409, doi:10.1175/JCLI3620.1, 2006.

Delecluse, P., M. K. Davey, Y. Kitamura, S. G. H. Philander, M. Suarez, and L. Bengtsson, Coupled general circulation modeling of the tropical pacific, *Journal of Geophysical Research-oceans*, *103*(C7), 14,357–14,373, doi:10.1029/97JC02546, 1998.

Duynkerke, P., H. Zhang, and P. Jonker, Microphysical and turbulent structure of nocturnal stratocumulus as observed during astex, *J Atmos Sci*, *52*(16), 2763–2777, 1995.

Eastman, R., S. G. Warren, and C. J. Hahn, Variations in cloud cover and cloud types over the ocean from surface observations, 1954-2008, *Journal of Climate*, *24* (22), 5914–5934, doi:10.1175/2011JCLI3972.1, 2011.

Feingold, G., B. Stevens, W. Cotton, and A. Frisch, The relationship between drop in-cloud residence time and drizzle production in numerically simulated stratocumulus clouds, *J Atmos Sci*, *53*(8), 1108–1122, 1996.

Feingold, G., A. Frisch, B. Stevens, and W. Cotton, On the relationship among cloud turbulence, droplet formation and drizzle as viewed by doppler radar, microwave radiometer and lidar, *J. Geophys. Res.-Atmos.*, *104*, 22,195–22,203, 1999.

Franklin, C., P. Villancourt, and M. Yau, Statistics and parameterizations of the effect of turbulence on the geometric collision kernel of cloud droplets, *J. Atmos. Sci.*, *64*, 938–954, 2007.

Frisch, A., C. Fairall, and J. Snider, Measurement of stratus cloud and drizzle parameters in astex with a k-alpha-band doppler radar and a microwave radiometer, *J Atmos Sci*, *52*(16), 2788–2799, 1995.

Gerber, H., Supersaturation and droplet spectral evolution in fog, *J. Atmos. Sci.*, *48*, 2569–2588, 1991.

Gerber, H., B. G. Arends, and A. S. Ackerman, New microphysics sensor for aircraft use, *Atmos. Res.*, *31*, 235–252, 1994.

Hall, W. D., A detailed microphysical model within a two-dimensional dynamic framework - model description and preliminary-results, *Journal of the Atmospheric Sciences*, *37*(11), 2486–2507, doi:10.1175/1520-0469(1980)037<2486:ADMMWA>2.0.CO;2, 1980.

Hartmann, D., M. Ockertbell, and M. Michelsen, The effect of cloud type on earth's energy balance: Global analysis, *J Climate*, *5*(11), 1281–1304, 1992.

Hudson, J. G., and G. Svensson, Cloud microphysical relationships in california marine stratus, *Journal of Applied Meteorology*, *34*(12), 2655–2666, doi:10.1175/1520-0450(1995)034<2655:CMRICM>2.0.CO;2, 1995.

Jensen, J., S. Lee, P. Krummel, J. Katzfey, and D. Gogoasa, Precipitation in marine cumulus and stratocumulus. part i: Thermodynamic and dynamic observations of closed cell circulations and cumulus bands, *Atmos. Res.*, *54*, 117–155, 2000.

Joe, P., and R. List, Testing and performance of two-dimensional optical array spectrometers with greyscale, *J. Atmos. Ocean. Tech.*, *4*, 139–150, 1987.

Johnson, D. B., The role of giant and ultra-giant aerosol-particles in warm rain initiation, *Journal of the Atmospheric Sciences*, *39*(2), 448–460, 1982.

Jonas, P. R., Turbulence and cloud microphysics, *Atmospheric Research*, *40*(2-4), 283–306, 1996.

Klein, S., and D. Hartmann, The seasonal cycle of low stratiform clouds, *J Climate*, *6*(8), 1587–1606, 1993.

Knollenberg, R. G., The optical array: An alternative to scattering for airborne particle size determination, *J. Appl. Meteor.*, *9*, 86–103, 1970.

Korolev, A., J. W. Strapp, and G. A. Isaac, Evaluation of the accuracy of pms optical array probes, *J. Atmos. Ocean. Tech.*, *15*, 708–720, 1998.

Lilly, D., Models of cloud-topped mixed layers under a strong inversion, *Q J Roy Meteor Soc*, *94*(401), 292–309, 1968.

Lilly, D. K., Entrainment into mixed layers. part ii: A new closure, *J. Atmos. Sci.*, *59*(23), 3353–3361, doi:10.1175/1520-0469(2002)059<3353:EIMLPI>2.0.CO;2, 2002.

Lin, C. L., and S. C. Lee, Collision efficiency of water drops in atmosphere, *Journal of the Atmospheric Sciences*, *32*(7), 1412–1418, doi:10.1175/1520-0469(1975)032<1412:CEOWDI>2.0.CO;2, 1975.

Lorenz, E. N., Available potential energy and the maintenance of the general circulation, *Tellus*, *7*(2), 157–167, 1955.

Lu, M., W. C. Conant, H. H. Jonsson, V. Varutbangkul, R. C. Flagan, and J. H. Seinfeld, The marine stratus/stratocumulus experiment (mase): Aerosol-cloud relationships in marine stratocumulus, *J. Geophys. Res.-Atmos.*, *112*, 2007.

Magaritz, L., M. Pinsky, O. Krasnov, and A. Khain, Investigation of droplet size distributions and drizzle formation using a new trajectory ensemble model. part ii: Lucky parcels, *Journal of the Atmospheric Sciences*, *66*(4), 781–805, doi:10.1175/2008JAS2789.1, 2009.

Manton, M. J., Collection kernel for coalescence of water droplets, *Tellus*, *26*(3), 369–375, 1974.

Marshall, J. S., and W. M. Palmer, The distribution of raindrops with size, *Journal of Meteorology*, *5*(4), 165–166, doi:10.1175/1520-0469(1948)005<0165:TDORWS>2.0.CO;2, 1948.

Mason, B., Production of rain and drizzle by coalescence in stratiform clouds, *Quart. J. R. Met. Soc.*, *78*, 377–386, 1952.

Mason, B. J., and P. R. Jonas, Evolution of droplet spectra and large droplets by condensation in cumulus clouds, *Quarterly Journal of the Royal Meteorological Society*, *100*(423), 23–38, doi:10.1256/smsqj.42302, 1974.

McGraw, R., and Y. G. Liu, Brownian drift-diffusion model for evolution of droplet size distributions in turbulent clouds, *Geophysical Research Letters*, *33*(3), L03,802, doi:10.1029/2005GL023545, 2006.

Newman, M. E. J., Power laws, pareto distributions and zipf's law, *Contemporary Physics*, *46*(5), 323–351, doi:10.1080/00107510500052444, 2005.

Nicholls, S., The dynamics of stratocumulus - aircraft observations and comparisons with a mixed layer model, *Q J Roy Meteor Soc*, *110*(466), 783–820, 1984.

Nicholls, S., A model of drizzle growth in warm, turbulent, stratiform clouds, *Q J Roy Meteor Soc*, *113*(478), 1141–1170, 1987.

Paluch, I., and D. Lenschow, Stratiform cloud formation in the marine boundary-layer, *J Atmos Sci*, *48*(19), 2141–2158, 1991.

Petters, M. D., J. R. Snider, B. Stevens, G. Vali, I. Faloona, and L. M. Russell, Accumulation mode aerosol, pockets of open cells, and particle nucleation in the remote subtropical pacific marine boundary layer rid d-2144-2009, *Journal of Geophysical Research-atmospheres*, *111*(D2), D02,206, doi:10.1029/2004JD005694, 2006.

Pincus, R., and M. Baker, Effect of precipitation on the albedo susceptibility of clouds in the marine boundary-layer, *Nature*, *372*(6503), 250–252, 1994.

Pinsky, M., A. Khain, and M. Grits B. Shapiro, Collisions of small drops in a turbulent flow. part iii: Relative droplet fluxes and swept volumes, *J. Atmos. Sci.*, *63*, 2123–2139, 2006.

Pinsky, M., O. Krasnov, H. W. J. Russchenberg, and A. Khain, Investigation of the turbulent structure of a cloud-capped mixed layer using doppler radar, *Journal of Applied Meteorology and Climatology*, *49*(6), 1170–1190, doi:10.1175/2010JAMC2280.1, 2010.

Pruppacher, H., and K. V. Beard, A wind tunnel investigation of internal circulation and shape of water drops falling at terminal velocity in air, *Quarterly Journal of the Royal Meteorological Society*, *96*(408), 247–&, doi:10.1002/qj.49709640807, 1970.

Pruppacher, H., and R. Rasmussen, Wind-tunnel investigation of the rate of evaporation of large water drops falling at terminal velocity in air, *J Atmos Sci*, *36*(7), 1255–1260, 1979.

Pruppacher, H. R., and J. Klett, *Microphysics of Clouds and Precipitation*, Kluwer Adademic Publishers, 1997.

Randall, D. A., and J. Y. Wang, The moist available energy of a conditionally unstable atmosphere, *J. Atmos. Sci.*, *49*(3), 240–255, doi:10.1175/1520-0469(1992)049<0240:TMAEOA>2.0.CO;2, 1992.

Rasinski, P., H. Pawlowska, and W. W. Grabowski, Observations and kinematic modeling of drizzling marine stratocumulus, *Atmospheric Research*, *102*(1-2), 120–135, doi:10.1016/j.atmosres.2011.06.020, 2011.

Reuter, A., and S. Bakan, Improvements of cloud particle sizing with a 2d-grey probe, *J. Atmos. Ocean. Tech.*, *15*, 1193–1203, 1998.

Roach, W. T., R. Brown, S. J. Caughey, B. A. Crease, and A. Slingo, A field-study of nocturnal stratocumulus .1. mean structure and budgets, *Quart. J. Roy. Meteor. Soc.*, *108*(455), 103–123, doi:10.1256/smsqj.45506, 1982.

Rogers, R., and M. K. M.K Yau, *A Short Course in Cloud Physics*, 3 ed., 292 pp., Pergamon Press, 1989.

Rossow, W. B., and R. A. Schiffer, Advances in understanding clouds from isccp, *Bulletin of the American Meteorological Society*, *80*(11), 2261–2287, doi:10.1175/1520-0477(1999)080<2261:AIUCFI>2.0.CO;2, 1999.

Sharon, T. M., B. A. Albrecht, H. H. Jonsson, P. Minnis, M. M. Khaiyer, T. M. van Reken, J. Seinfeld, and R. Flagan, Aerosol and cloud microphysical characteristics of rifts and gradients in maritime stratocumulus clouds rid g-1902-2010, *Journal of the Atmospheric Sciences*, *63*(3), 983–997, doi:10.1175/JAS3667.1, 2006.

Siebert, R. A. S. Z. W., H., Statistics of small-scale velocity fluctuations and internal intermittency in marine stratocumulus clouds, *J. Atmos. Sci*, *67*, 262–273, 2010.

Sivaprakasam, S., and V. Kanakasabai, Traditional almanac predicted rainfall - a case study, *Indian Journal of Traditional Knowledge*, *8*(4), 621–625, 2009.

Slingo, A., Sensitivity of the earths radiation budget to changes in low clouds, *Nature*, *343*(6253), 49–51, 1990.

Solomon, D. Q. M. M. Z. C. M. M. K. A. M. T., S., and H. M. (eds.), *IPCC, 2007: Climate Change 2007: The Physical Science Basis. Contribution of Working Group I to the Fourth Assessment Report of the Intergovernmental Panel on Climate Change*, Cambridge University Press, Cambridge, United Kingdom and New York, NY, USA, 2007.

Stephens, G., Cloud feedbacks in the climate system: A critical review, *J Climate*, *18*(2), 237–273, 2005.

Stephens, G., and T. Greenwald, The earths radiation budget and its relation to atmospheric hydrology .2. observations of cloud effects, *J. Geophys. Res.-Atmos.*, *96*(D8), 15,325–15,340, 1991.

Stevens, B., W. Cotton, G. Feingold, and C. Moeng, Large-eddy simulations of strongly precipitating, shallow, stratocumulus-topped boundary layers, *J Atmos Sci*, *55*(24), 3616–3638, 1998.

Stevens, B., G. Vali, K. Comstock, R. Wood, M. van Zanten, P. Austin, and D. Bretherton C.S. nd Lenschow, Pockets of open cells and drizzle in marine stratocumulus, *Bull. Amer. Met. Soc.*, *86*, 51–+, 2005.

Stevens, B., et al., Dynamics and chemistry of marine stratocumulus - dycoms-ii, *Bull. Amer. Met. Soc.*, *84*, 579–+, 2003.

Strapp, J., F. Albers, A. Reuter, A. Korolev, U. Maixner, E. Rashke, and Z. Vukovic, Laboratory measurements of the response of a pms oap-2dc, *J. Atmos. Ocean. Tech.*, *18*, 1150–1170, 2001.

Stull, R. B., *An Introduction to Boundary Layer Meteorology*, Kluwer Academic Publishers, 1988.

Telford, J. W., and S. K. Chai, A new aspect of condensation theory, *Pure and Applied Geophysics*, *118*(3), 720–742, doi:10.1007/BF01593025, 1980.

Vali, G., R. Kelly, J. French, S. Haimov, D. Leon, R. McIntosh, and A. Pazmany, Finescale structure and microphysics of coastal stratus, *J Atmos Sci*, *55*(24), 3540–3564, 1998.

vanZanten, M., B. Stevens, G. Vali, and D. Lenschow, Observations of drizzle in nocturnal marine stratocumulus, *J Atmos Sci*, *62*(1), 88–106, 2005.

vanZanten, M. C., and B. Stevens, Observations of the structure of heavily precipitating marine stratocumulus, *Journal of the Atmospheric Sciences*, *62*(12), 4327–4342, doi:10.1175/JAS3611.1, 2005.

Wang, H. L., and G. Feingold, Modeling mesoscale cellular structures and drizzle in marine stratocumulus. part i: Impact of drizzle on the formation and evolution of open cells rid b-8061-2010, *Journal of the Atmospheric Sciences*, *66*(11), 3237–3256, doi:10.1175/2009JAS3022.1, 2009.

Wang, L. P., O. Ayala, S. E. Kasprzak, and W. W. Grabowski, Theoretical formulation of collision rate and collision efficiency of hydrodynamically interacting cloud droplets in turbulent atmosphere, *J. Atmos. Sci.*, *62*, 2433–2450, 2005.

Wang, S., Modeling marine boundary-layer clouds with a 2-layer model - a one-dimensional simulation, *J Atmos Sci*, *50*(24), 4001–4021, 1993.

Wang, S., and Q. Wang, Roles of drizzle in a one-dimensional 3rd-order turbulence closure-model of the nocturnal stratus-topped marine boundary-layer, *J Atmos Sci*, *51*(11), 1559–1576, 1994.

Wendisch, M., T. Garrett, and J. Strapp, Wind tunnel tests of the airborne pvm-100a response to large droplets, *J. Atmos. Ocean. Tech.*, *19*, 1577–1584, 2002.

Wood, R., Drizzle in stratiform boundary layer clouds. part 1: Vertical and horizontal structure, *J Atmos Sci*, *62*, 3011–3033, 2005.

Wood, R., et al., The vamos ocean-cloud-atmosphere-land study regional experiment (vocals-rex): goals, platforms, and field operations, *Atmospheric Chemistry and Physics*, *11*(2), 627–654, doi:10.5194/acp-11-627-2011, 2011.

Wyant, M. C., C. S. Bretherton, J. T. Bacmeister, J. T. Kiehl, I. M. Held, M. Zhao, S. A. Klein, and B. J. Soden, A comparison of low-latitude cloud properties and their response to climate change in three agcms sorted into regimes using mid-tropospheric vertical velocity, *Climate Dynamics*, *27*(2-3), 261–279, doi:10.1007/s00382-006-0138-4, 2006.